GEORG-AUGUST-UNIVERSITÄT
GÖTTINGEN

Fakultät für
Physik

Bachelor's Thesis

Untersuchung von Variablen zur Identifizierung von Teilchen in der schnellen ATLAS Kalorimetersimulation

Investigation of shower shape variables in the ATLAS Fast Calorimeter Simulation

prepared by

Carla Neubert

from Berlin

at the II. Physikalischen Institut

Thesis number:	II.Physik-UniGö-BSc-2021/03
Thesis period:	12th May 2021 until 18th August 2021
First referee:	Prof. Dr. Stan Lai
Second referee:	Priv. Doz. Dr. Jörn Große-Knetter

Abstract

Die schnelle Atlas Kalorimetersimulation ist Teil des neuen Simulationspakets AtlFast3, das die rechenaufwendige Simulation durch Geant4 mit verbesserter Genauigkeit im Vergleich zur vorherigen Generation AtlFastII ersetzen soll. Die schnelle Kalorimetersimulation basiert auf einer Parametrisierung der Detektorantwort, denn die Simulation der Kalorimeterantwort ist am rechenintensivsten.

Diese Bachelorarbeit widmet sich der Untersuchung von Variablen in der schnellen Atlas Kalorimetersimulation, die Teilchenschauer in einem Kalorimeter beschreiben. Dafür werden die Variablen in der schnellen Atlas Kalorimetersimulation implementiert. Die Verteilungen werden für die schnelle Kalorimetersimulation und die vollständige Geant4 Simulation verglichen, für Elektronen und Photonen sowie für elektromagnetische und hadronische Schauer. Darüber hinaus wird ein vereinfachter Algorithmus zur Clusterbildung von deponierter Energie im Kalorimeter implementiert. Das dient dazu, das Verständnis über verbleibenden Unterschiede zwischen der schnellen und der vollständigen Simulation des Kalorimeters zu verbessern.

Die Anzahl von Clustern, die mit dem vereinfachten Clusteralgorithmus rekonstruiert wurden, weicht für die schnelle Kalorimetersimulation signifikant von der Anzahl für die volle Simulation ab. Daher kann geschlossen werden, dass die Clusterbildung in der schnellen Kalorimetersimulation ein Grund dafür sein könnte, dass die Verteilungen von komplexeren Variablen in der schnellen Detektorsimulation noch immer von denen für die volle Simulation abweichen.

Abstract

The Atlas Fast Calorimeter Simulation is part of the new simulation toolkit AtlFast3, which is designed to replace the computationally expensive Geant4 simulation with improved accuracy compared to its predecessor AtlFastII. The Fast Calorimeter Simulation uses a parameterised modelling of the calorimeter response to reduce the required CPU consumption, which is dominated by the simulation of the calorimeter.

In this Bachelor's thesis, the shower shape variables in the Fast Calorimeter Simulation of the Atlas experiment are investigated. For this purpose, the variables used for electron and photon identification in Atlas are implemented in the Fast Calorimeter Simulation (FastCaloSim) algorithm. Comparisons of the distributions for FastCaloSim and Geant4, for electrons and photons and for electromagnetic and hadronic showers are made. In addition, a simple clustering algorithm is implemented in order to help understanding the remaining differences between FastCaloSim and Geant4.

Significant differences in the number of clusters built with FastCaloSim and Geant4 suggest that clustering is part of the reason for the remaining differences of the fast simulation toolkit AtlFast3 and the full simulation Geant4 for high level variables.

Contents

1. Introduction

The Standard Model [1] in particle physics describes elementary particles and their interactions in a quantum field theory. A major milestone to a more complete model was reached with the discovery of the Higgs boson. In 2013, the Nobel Prize in physics was awarded to Peter Higgs and François Englert after their theoretical prediction [2–4] of the Higgs boson, which was observed by the ATLAS [5] and CMS [6] experiments at the Large Hadron Collider (LHC) at CERN. This extraordinary discovery of an additional particle has not only changed our understanding of the fundamental components of the universe, but leaves some open questions, too. Both experiments at the largest particle accelerator in the world are dedicated to study the properties of the Higgs boson, validate theoretical predictions of the Standard Model and also to search for physics beyond the Standard Model.

In order to compare theoretical predictions of proton-proton collisions with data, events in the ATLAS experiment need to be simulated including the detector response. With the planned increased integrated luminosity at the LHC, the required CPU resources will outgrow the available capacity. Therefore, a faster simulation of the detector response is required and is provided by AtlFast3, a fast simulation toolkit, which has been employed recently by the ATLAS Collaboration. The simulation time in the calorimeter is significantly reduced with a parameterised modelling of the particle showers in the calorimeter while retaining excellent accuracy. It is designed to reproduce GEANT4, a simulation toolkit, which simulates the response of all particles in the calorimeter individually. For further improvement of the simulation of electron and photon induced showers, variables describing the shower shape and used for electron and photon identification in ATLAS, are expected to be tuned to real data. To facilitate this in prospective work on FastCaloSim, this Bachelor's thesis aims to implement these variables in the standalone FastCaloSim algorithm, which is more convenient to run than the full ATLAS simulation and reconstruction.

The theoretical background for this thesis is provided in Chapter 2, which briefly describes the Standard Model and Chapter 3, which describes the fundamentals of particle showers. Then, descriptions of the experimental setup of the ATLAS detector are provided

in Chapter 4 and of electron and photon identification in Chapter 5. The Fast Calorimeter Simulation is outlined in Chapter 6. In Chapter 7, the distributions of the shower shape variables gained from the implementation in the standalone FastCaloSim algorithm are presented and discussed. In Chapter 8, clustering in ATLAS and the implementation of a simple clustering algorithm in the standalone FastCaloSim algorithm for a better understanding of remaining differences between FastCaloSim and GEANT4 are described. Conclusions are drawn in Chapter 9.

2. Theory of the Standard Model

In this chapter, a short introduction to the Standard Model (SM) of particle physics is provided, electroweak symmetry breaking is briefly described and the limitations of the SM are specified.

The SM of particle physics [1] describes all known elementary particles and their interactions. This includes the electromagnetic, the strong and the weak interaction. Gravitation as the fourth fundamental force is not included in the SM.

The elementary particles in the SM can be divided into two groups. Firstly, there are particles with spin $\frac{1}{2}$, called fermions, and secondly, there are particles with integer spin, called bosons, that mediate interactions. The first group can be further split into two categories, quarks, to which the strong interaction couples, and leptons, to which it does not. The two categories can be arranged according to three different generations. The first quark generation includes up and down quarks, the second one charm and strange quarks and the third one top and bottom quarks. The three lepton generations each include an electron, a muon or a tau-lepton plus the respective neutrino. Particles in higher generations are heavier and less stable as they can decay into lighter particles. Quarks carry electromagnetic charge of either $\frac{2}{3}e$ for the up-type quarks or $-\frac{1}{3}e$ for the down-type quarks, where e is the elementary charge. Leptons either carry electromagnetic charge of $-1e$ (electrons, muons, taus), $+1e$ (the respective anti-leptons) or are not charged at all (neutrinos). Furthermore, there is an anti-particle for each fermion with the same properties except for the charge, which is the opposite for the fermions and anti-fermions. While leptons can exist and be detected independently, quarks are always found in bound states with other particles.

For each of the three forces, there is a corresponding gauge boson in the SM, which all have spin 1: the gluon for the strong interaction, the photon for the electromagnetic interaction and the Z and the W bosons for the weak interaction. In addition to these vector bosons (spin 1), there is one scalar boson (spin 0), called the Higgs boson. According to the Brout-Englert-Higgs-mechanism (BEH mechanism) [2–4], the elementary particles gain their mass via interaction with the Higgs-field. An overview of the particles in the SM is shown in Figure 2.1.

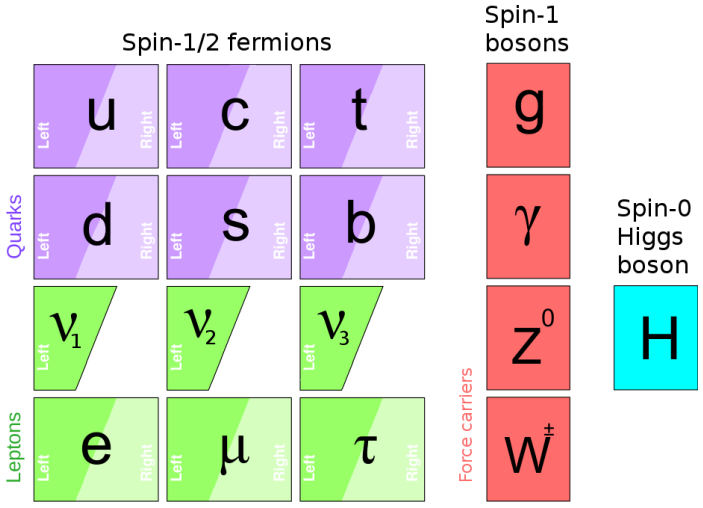

Figure 2.1.: Elementary particles in the SM [7].

The strong interaction only couples with particles that carry a colour charge. The only particles which carry colour charge are quarks and gluons. There are three different colours, red, green and blue, and the corresponding anti-colours. Quarks are never found as free particles but always come in bound colourless states. The gluon carries both colour charge and anti-colour charge, and there are eight different colour states for the gluon.

The electromagnetic interaction couples to fermions which carry electromagnetic charge by exchanging a photon as the gauge boson.

The weak interaction couples to all fermions and is the only one of the three forces capable of changing the quarks' flavour. The $W^{\pm}$ boson couples only to particles of left-handed chirality and to anti-particles of right-handed chirality.

The three interactions in the SM can be described in terms of a quantum field theory [8] under the condition that the Lagrange density is invariant under local phase transformations. In quantum field theory, particles are equivalent to excitations of certain fields. To ensure the invariance in the Lagrange density, gauge fields are introduced. The underlying symmetry of quantum chromodynamics is the invariance under $SU(3)$ local phase transformations. As the electromagnetic and weak interactions have been successfully unified into the electroweak interaction [9–11], they are subject to a combined gauge symmetry $SU(2)_L \otimes U(1)_Y$, where the index L stands for left-handed chirality coupling and the index Y stands for the hypercharge $Y = 2(Q - T_3)$ with the electric charge Q and the third component of the weak isospin T_3. Under these assumptions, the theory of the SM requires the four gauge bosons to be massless. While the gauge bosons of the electromagnetic and the strong interaction, the photon and the gluon, are indeed massless, it has nevertheless been shown in numerous experiments that the gauge bosons of the weak

interaction, the W^+, W^- and the Z^0 boson, possess masses [12, 13].

In order to solve this contradiction of theory and observation, a complex doublet of scalar fields is added to the Lagrange density [14, 15]. The corresponding potential, also known as Higgs-potential, can be written as

$$V(\phi) = \mu^2\phi^\dagger + \lambda(\phi^\dagger\phi)^2, \tag{2.1}$$

with $\mu^2 < 0$ and $\lambda > 0$, and is shown in Figure 2.2. All other quantum fields have a global minimum in the origin and thus a vacuum expectation value of zero. However, the Higgs-potential has a global minimum at a distance v from the origin and a vacuum expectation value of about $V \simeq 246\,\text{GeV}$ as determined from measurements [8]. This causes the spontaneous symmetry breaking, as the ground state of the system does not respect the symmetry of the system. Only this outstanding property of the Higgs field allows the W bosons and the Z boson to possess mass, as they interact with the Higgs field where the expectation value is not zero. Their masses can be written as functions of v:

$$m_W = \frac{1}{2} g_W v,$$
$$m_Z = \frac{1}{2} \frac{g_W}{\cos\theta_W} v,$$

where g_W is the weak coupling constant and θ_W is the weak mixing angle. Through the BEH mechanism, the SM predicts the existence of the Higgs boson.

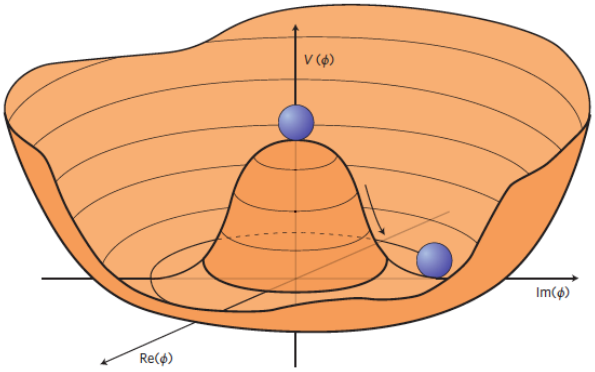

Figure 2.2.: The potential of the Higgs field [16].

Although all current measurements are in agreement with the predictions of the SM, the SM is not a complete theory of everything and has limitations. First of all, it does not explain the phenomenon of gravitation, one of the four fundamental forces in the universe,

because it is not possible to quantise and renormalise gravitation with known methods. Furthermore, it is known from astrophysical measurements that there is significantly more matter in the universe than directly detectable in order to explain certain gravitational phenomena. The SM fails to explain this additional invisible matter, called dark matter [17]. Another problem is that the SM only accounts for some of the observed asymmetry between matter and antimatter in the universe (through CP violation) but by far not all of it [18]. Finally, there is the hierarchy problem [19] which denotes the unexplained discrepancy in the scale of gravitational force and the other forces.

3. Fundamentals of particle shower development

In order to determine the energy of high energetic particles, one can exploit the phenomenon of particle showering in material [20]. When entering a slab of matter, a high energy particle induces a chain of inelastic reactions. This is a destructive process because for electromagnetic showers, the primary particle's energy is divided between a number of secondary particles. In this way, a particle shower is induced with a decreasing fraction of energy per particle with an increasing number of particles. Finally, when a single particle does not have enough energy to shower further, it deposits its energy in the material via ionisation. The threshold for this is called critical energy E_c and is defined as the energy where the loss through Bremsstrahlung is equal to the loss through ionisation. The deposited energy can by measured by the induced charge, scintillation light or Cherenkov light.

The underlying processes of an electromagnetic particle shower are Bremsstrahlung and pair production. On average, one of the processes occur every radiation length X_0. The mean free path of a photon is about $\frac{9}{7}X_0$ and a particle loses on average 63% of its energy after travelling a distance of X_0 through matter. The radiation length X_0 is roughly proportional to $\frac{A}{Z^2}$, where A is the mass number and Z is the proton number of the given material.

The longitudinal profile of the shower is best described by the shower maximum [21]. After a distance of $s = t \cdot X_0$ the number of particles is in a simplified model $N = 2^t$ and the energy per particle $E = \frac{E_0}{2^t}$ with the energy of the initial particle E_0. Therefore, the shower maximum can be determined:

$$\frac{E_0}{2^{t_{\max}}} \Leftrightarrow t_{\max} = \frac{\log(E_0/E_c)}{\log 2}.$$

Since the maximal number of particles is set by the initial energy and the critical energy

$$N_{\max} = 2^{\max} = \frac{E_0}{E_c},$$

the shower maximum is at $t_{\max} \propto \log E + c$ times the radiation length, where c is a constant.

Furthermore, the transverse scattering of the particles must be considered. The transverse profile of the shower can be described with the Molière-radius R_M. It describes the mean deflection of electrons at the critical energy after travelling one radiation length. On average, 90% of the shower energy is contained in a cylinder with radius R_M. The Molière-radius can be approximated by $R_M \simeq 21\,\mathrm{MeV} \cdot \frac{X_0}{E_c}$ [8].

Hadronic particle showers are more complex than electromagnetic showers and will only be briefly mentioned in the following since this Bachelor's thesis mainly focuses on the simulation of the electromagnetic calorimeter response in ATLAS. Multiple physical processes are involved in the hadronic shower development. In a high energy cascade, the incoming particle interacts inelastically with a nucleus of the material. Highly energetic particles are produced, which can interact with other nuclei. Within the nucleus, the incoming hadron scatters with a nucleon and induces an intra-nuclear cascade, too. This ends when the particles leave the nucleus or have too little energy left to interact further. Additionally, fragments of the nucleus are struck out in a process called spallation. After this, excited nuclei are left over and they emit their energy by evaporating nucleons and fragments of the nuclei. Sometimes it comes to a nuclear fission. A hadronic shower is characterised by the absorption length λ_a. It describes the mean free path between two nuclear collisions.

4. The ATLAS detector

ATLAS (A Toroidal LHC ApparatuS) a general purpose detector at the Large Hadron Collider (LHC) at the European Organisation for Nuclear Research (CERN). In this chapter, a brief description of the accelerator chain and the different detectors at the LHC is provided, followed by a more detailed description of the ATLAS detector with focus on the calorimeter system.

4.1. The Large Hadron Collider at CERN

CERN is based in Geneva and studies the properties and interactions of particles, tests predictions of the SM and searches for physics beyond the SM.

After passing through various pre-accelerators, particles are injected into the main and largest accelerator, the LHC [22]. The first link in the chain is the LINAC 4, a linear particle accelerator installed in the second long shutdown period in 2020, replacing LINAC 2. It accelerates ions, which are then injected into the Proton Synchrotron Booster. There, protons are extracted from the ions and accelerated further. In the Proton Synchrotron (PS) and afterwards in the Super Proton Synchrotron (SPS), the protons are accelerated to 450 GeV and can finally be injected into the LHC. The LHC has a circumference of 27 km in an underground tunnel and collides protons with a centre-of-mass energy of 13 TeV and a instantaneous luminosity of $10^{34}\,\mathrm{cm}^{-2}\,\mathrm{s}^{-1}$. The different accelerators and experiments are shown in Figure 4.1.

The schedule of the LHC is composed of periods of data taking and periods of maintenance and upgrades. In Run 1, between 2010 and 2013, protons were collided with a centre-of-mass energy of $\sqrt{s} = 7$ and 8 TeV. After a shutdown period of two years, Run 2 with $\sqrt{s} = 13$ TeV started. A second long shutdown period is expected to last until 2022, followed by a third run with $\sqrt{s} = 13$-14 TeV. A high-luminosity upgrade is planned and is expected to increase the luminosity by a factor of 10 in 2028 the earliest.
The ATLAS detector [5] is one of the four main detectors at the LHC along with CMS, ALICE and LHCb. The ALICE experiment studies properties of quark-gluon plasma that existed shortly after the Big Bang. The LHCb experiment investigates CP-violation and

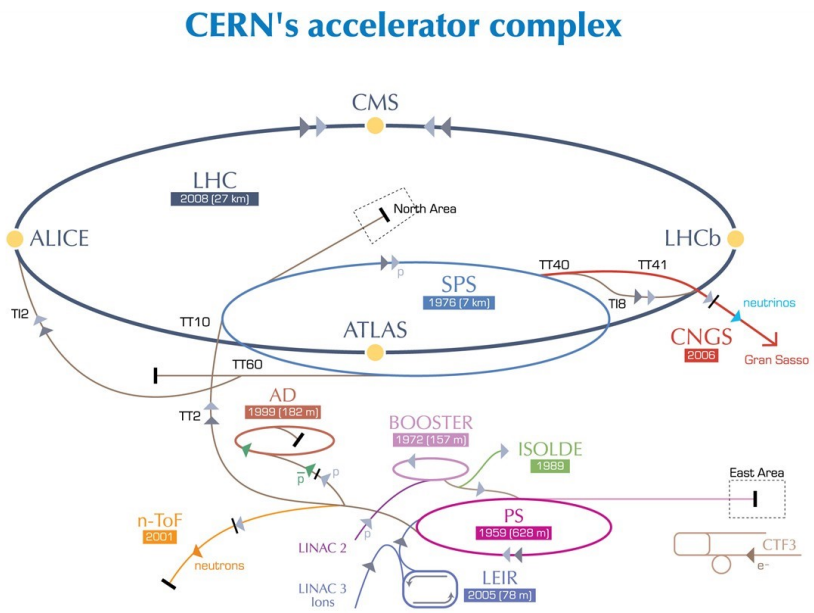

Figure 4.1.: Schematic view of the Lhc accelerator chain and the different detectors [23].

the problem of the observed asymmetry between matter and antimatter among other things. The Atlas experiment, like the Cms detector, is a general purpose particle detector. About 4000 physicists around the world are involved in the experiment. The different detector layers are arranged around the beam like a toroid. A schematic view of the detector is shown in Figure 4.2.

The Inner Detector (ID), which tracks charged particles and measures their momenta, consists of an insertable B-Layer (IBL), a pixel detector, a semiconductor detector and a transition radiation tracker. Additionally, there is an electromagnetic (ECAL) and a hadronic calorimeter (HCAL), that measure the particles' energy, as well as a Muon Spectrometer (MS). The resolution of the transverse momentum and the energy, and pseudorapidity coverage for each part of the detector is shown in Table 4.1.

4.2. Coordinate system

In Atlas, the collision point of the particles in the centre of the detector is chosen as the origin. The x-axis of the right-handed Cartesian coordinate system points towards the centre of the Lhc, the y-axis points upwards and the z-axis is parallel to the beam. However, due to the concentric geometry, a cylindrical coordinate system is used with an azimuthal angle ϕ and a polar angle θ. Nevertheless, instead of θ, the pseudorapidity

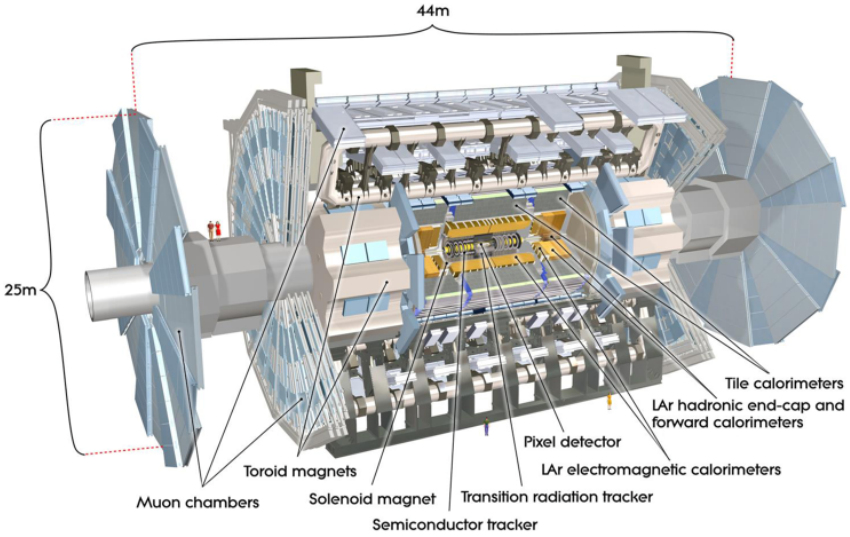

Figure 4.2.: Overview of the ATLAS detector [5].

Detector	resolution	η coverage
ID	$\sigma_{p_T}/p_T = 0.05\% p_T \oplus 1\%$	$\lvert\eta\rvert < 2.5$
EMCAL	$\sigma_E/E = 10\%/\sqrt{E} \oplus 0.7\%$	$\lvert\eta\rvert < 3.2$
HCAL:		
barrel and end-cap	$\sigma_E/E = 50\%/\sqrt{E} \oplus 3\%$	$\lvert\eta\rvert < 3.2$
forward	$\sigma_E/E = 100\%/\sqrt{E} \oplus 10\%$	$3.1 < \lvert\eta\rvert < 4.9$
MS	$\sigma_{p_T}/p_T = 10\%$ at $p_T = 1\,\text{TeV}$	$\lvert\eta\rvert < 2.7$

Table 4.1.: The resolution and pseudorapidity coverage of the different detector components [5]. The units for E and p_T are in GeV.

$\eta \equiv -\ln[\tan\left(\frac{\theta}{2}\right)]$ is preferred since differences in the pseudorapidity are approximately Lorentz invariant under boosts in z-direction. It ranges from $-\infty$ to $+\infty$ and equals to zero at a polar angle $\theta = \pi/2$. The ATLAS detector covers a range of $|\eta| < 4.9$. The angular separation of two objects is defined as $\Delta R \equiv \sqrt{(\Delta\eta)^2 + (\Delta\phi)^2}$.

4.3. Inner Detector

The Inner Detector (ID) [5] of the ATLAS detector system is composed of the insertable B-Layer (IBL), the pixel detector, the semiconductor tracker (SCT) and the transition radiation tracker (TRT). They are surrounded by a magnetic field of 2 T, which causes the tracks of the charged particles to bend. From the curvature of the tracks, the transverse momentum can be reconstructed. The pixel detector is capable of very precise tracking due to the high number of pixels with approximately 92 million readout channels together with the insertable B-Layer. The latter improves the tracking performance and assists

in the reconstruction of primary and secondary vertices from B-hadron decays, which is why it plays an important role in b-jet identification. The semiconductor tracker is less precise because it uses strips instead of pixels but it covers a larger area with about 6.3 million readout channels. The outermost part of the ID, the transition radiation tracker, is made out of straw tubes filled with a gas mixture. These straw tubes are interleaved with foils that provide transition radiation. This is a form of electromagnetic radiation emitted when a relativistic charged particle crosses the interface of two media of different dielectric constants. The emitted radiation is proportional to the Lorentz factor, which is why the light electrons produce a larger signal than the heavier pions. This helps to differentiate electrons from pions. As part of the high luminosity upgrade of the LHC, the ID will be replaced by an all-silicon Inner Tracker (ITk) to improve the tracking performance [24].

4.4. Calorimeter system

The calorimeter system [5] is responsible for the energy measurement of the electromagnetically and hadronically interacting particles. The incoming particle induces a shower of secondary particles, which deposit their energy via ionisation in the detector material as described in Chapter 3.

All calorimeters in ATLAS are sampling calorimeters, which are compositions of active and passive material. The passive material is responsible for developing the particle shower whereas the active material collects the signal.

The lower η region is covered by the hadronic tile barrel and the liquid argon (LAr) electromagnetic barrel. In higher η regions, there are the LAr hadronic (HEC) and LAr electromagnetic (EMEC) end-caps. Closest to the beam is the LAr forward calorimeter.

The LAr electromagnetic calorimeters consist of a lead absorber as the passive medium and liquid argon in the gaps between the lead layers as the active medium. In order to keep the argon in a liquid state, the calorimeters are stored in cryostats. The lead layers are accordion-shaped. The waves are parallel to the radial direction and run axially. The folding angle and wave amplitude vary so that the gaps with the liquid argon and the readout electrodes do not cause a non-uniform detector response. This results in a uniform performance in terms of linearity and resolution as a function of ϕ.

The electromagnetic calorimeter is composed of multiple layers. Behind the presampler, also referred to as layer 0 in the following, the first layer is finely segmented along η so that there are thin strips for the position resolution in order to discriminate between photons and $\pi^0 \to \gamma\gamma$ decays. The second layer collects the largest fraction of energy and

is segmented in cells of size 0.025×0.025 in $\eta \times \phi$. The third layer collects only the tail of the electromagnetic shower and is therefore less segmented in η.

The hadronic tile calorimeter is composed of a steel absorber, which has a short absorption length of 16.8 cm, as the passive medium and scintillating tiles with a long absorption length of 79.4 cm as the active medium. It is the only part of the calorimeter system that is not housed in a cryostat. The LAr hadronic end-cap has a copper absorber as the passive medium to optimise the resolution and for heat removal.

The LAr forward calorimeter consists of three layers, of which the first one is an electromagnetic calorimeter with a copper absorber. The second and third layers are hadronic calorimeters with a tungsten absorber, which has a high density and melting point and also provides containment and minimises the lateral shower spread as it has a good radiation shielding.

For the electromagnetic LAr calorimeter, liquid argon is used as the active medium because of its intrinsic linear behaviour, its stability in response over time and its intrinsic radiation hardness. It has a long radiation length of about 14 cm so that the shower does not develop much in these active layers of the calorimeter. Additionally, the deformation of the barrel due to its weight is reduced in virtue of the Archimedes thrust caused by the liquid argon. Lead is used as the passive medium as it has a high proton number and is still stable. This results in a short radiation length, which is necessary for a well-developed shower.

As opposed to the relative momentum resolution, the energy resolution improves with increasing energy. Ideally, it is proportional to $\frac{1}{\sqrt{E}}$ as the variance of the number of particles σ_N is equal to the square root of N, which is equal to the total deposited energy divided by the critical energy. In practise, there is an additional noise term with factor b for electronic noise of the readout chain and a constant term with factor c for inhomogeneities and defects in the material. The total relative energy resolution is then given by

$$\frac{\sigma_E}{E} = \frac{a}{\sqrt{E/\mathrm{GeV}}} \oplus \frac{b}{E/\mathrm{GeV}} \oplus c. \tag{4.1}$$

The electromagnetic calorimeter has a significantly better energy resolution than the hadronic calorimeter due to large fluctuations in hadronic showers. Because the hadronic shower mechanisms are more complicated, the showers are longer and less narrow. As neutrinos might be produced in strong interactions, and some of the primary particle's energy is used to break up nuclei, invisible energy is a feature for hadronic showers.

4.5. Muon Spectrometer

Muons do not deposit their energy in the calorimeter system since they only lose little energy via Bremsstrahlung while travelling through matter due to their large mass. For this reason, there is a Muon Spectrometer (MS) [5] outside the calorimeter system, which measures the momenta of the muons with the help of a magnetic field of 0.5 T in the central region and 1 T in the end-cap region. The muons pass through gas-filled chambers and produce tracks, which are bent by the magnetic field. From the curvature, the momentum can be calculated. Other particles than muons are mostly absorbed in the ID layers and therefore are not usually detected in the MS.

4.6. Trigger system

Because the detectors produce an enormous amount of data due to the high frequency of collisions, a system to filter the data and select events interesting enough to record is required. This is what the trigger system [5] is for. It is divided into two steps: the hardware-based Level-1 trigger and the software-based High-level trigger. The Level-1 trigger makes very fast decisions with low resolution and scans for high p_T particles (muons, electrons, photons and jets) to define regions of interest (RoI). Because of the high speed of these decisions, software cannot meet the requirements and custom electronics are used instead. The High-level trigger can make more complex decisions, reconstructs trajectories and associates them with the measured energy in the calorimeter in order to choose events. The input data stream for the Level-1 trigger is 40 MHz and is reduced to 100-1000 kHz, which is the input data stream for the High-level trigger. The latter then reduces the data stream to 1-10 kHz.

5. Electron and photon identification in ATLAS

In this chapter, electron and photon identification in ATLAS based on shower shape variables will be discussed. As a first step, electron and photon candidates are reconstructed. For electron reconstruction [25], charged particle tracks in the ID are matched to energy clusters in the calorimeter, which are described in Chapter 8. Unconverted photons are reconstructed with the energy clusters only and no track or conversion vertex is required. For converted photons, a cluster is matched to a conversion vertex. Then, for electron and photon identification [26], multiple variables are defined in order to discriminate between real and fake electrons and photons. These variables describe certain properties of the particle shower in the calorimeter. For photon identification, cut-based criteria using these shower shape variables are applied. Hadronic jets account for the background.

For electron identification, jets, electrons from photon conversion and non-prompt electrons from the decay of hadrons containing heavy flavours are background components. A likelihood discriminate d_L is formed from the shower shape variables for each electron candidate

$$d_L = \frac{L_S}{L_S + L_B},$$

where

$$L_{S(B)}(\boldsymbol{x}) = \prod_{i=1}^{n} P_{S(B),i}\left(x_i\right)$$

with the vector $\boldsymbol{x}$ of values x_i for the variables i and the value of the signal (background) probability function $P_{S(B),i}(x_i)$ for the quantity i at value x_i. The probability density functions $P_{S(B),i}$ are obtained from simulated samples, where all three kinds of background are considered for the background probability density function. The likelihood discriminate d_L has a sharp peak at unity (zero) for signal (background), which makes tuning cuts on d_L difficult as it would require extremely fine binning. For this reason, a transformed

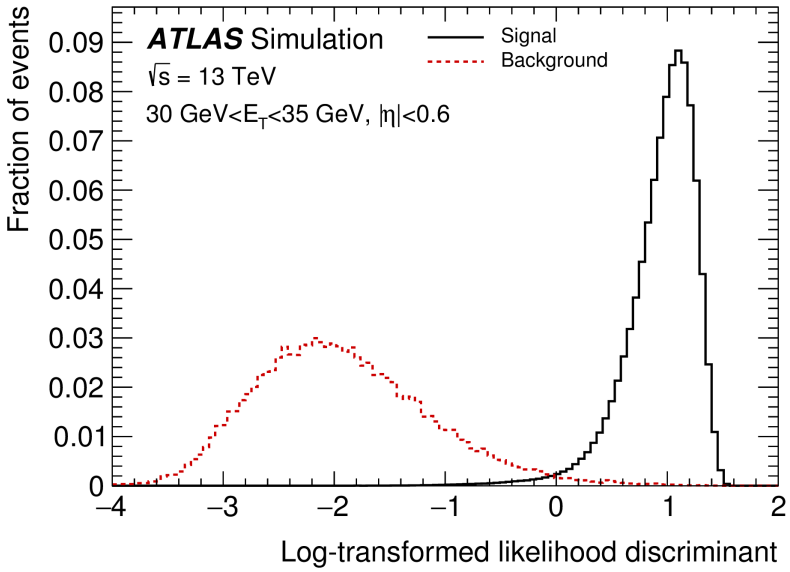

Figure 5.1.: Transformed likelihood discriminate d'_L for electron candidates in $Z \to ee$ events with tracks with $30\,\text{GeV} < E_T < 35\,\text{GeV}$ and $|\eta| < 0.6$ [26] and backgrounds in a two-to-two process simulation sample.

likelihood discriminate d'_L is defined

$$d'_L = -\tau^{-1}\ln(d_L^{-1} - 1)$$

with a parameter τ fixed to the value of 15 [27]. Electron candidates with values of d'_L above a chosen threshold are considered as signal. In Figure 5.1, the distribution of an example of a transformed likelihood discriminate for electron candidates in $Z \to ee$ events with tracks with $30\,\text{GeV} < E_T < 35\,\text{GeV}$ and $|\eta| < 0.6$ and backgrounds in a generic two-to-two process simulation sample is shown and illustrates the separation power of the likelihood discriminate between signal and background.

The different shower shape variables used for electron and photon identification are listed in Table 5.1. Variables with the largest separation power include f_{side}, E_{ratio}, ΔE, w_{stot}, R_ϕ, $w_{\eta 1}$, $w_{\eta 2}$, R_η and R_{had}. In Figure 5.2, some of the most important variables are visualised. In Figure 5.3, distributions of four of the shower shape variables E_{ratio}, f_3, R_η and R_ϕ for $20\,\text{GeV} < E_T < 30\,\text{GeV}$ and $0.6 < |\eta| < 0.8$ for signal determined from a $Z \to ee$ simulation sample and for background are shown. In addition to the listed shower shape variables, energy windows in $\eta \times \phi$ of different sizes around the cell with the most deposited energy are of interest.

Type	Description	Name	Usage
First layer of EM Calorimeter	Shower width using 3 strips: $\sqrt{\frac{\sum E_i \cdot (i-i_{\max})^2}{\sum E_i}}$	$w_{\eta 1}$	γ
	Shower width using 20 strips	w_{stot}	e/γ
	Fraction of energy outside core in the first layer: $\frac{E_7^{S1}-E_3^{S1}}{E_3^{S1}}$	f_{side}	γ
	Energy of the strip with the maximal energy	E_{maxs1}	
	Energy of the strip with the minimal energy between the first and second maximum	E_{mins1}	
	Energy of the strip of the second local maximum, i. e. the strip with the second most energy provided that the neighbour strips have less energy	E_{2tsts1}	
	Energy of the second local maximum in 3 strips	E_{2ts1}	
	Ratio of the energy difference associated with the largest and second largest energy deposits over the sum of these energies: $E_{\text{ratio}} = \frac{E_{\text{maxs1}}-E_{\text{2tsts1}}}{E_{\text{maxs1}}+E_{\text{2tsts1}}}$	E_{ratio}	e/γ
	$E_{\text{2tsts1}} - E_{\text{mins1}}$	ΔE	γ
	Ratio of the energy in the first layer to the total energy in the EM calorimeter	f_1	e/γ
	Fraction of energy in the core (3x2 window) in first layer	$f_{1,\text{core}}$	
	Asymmetry with 3 strips, i.e. energy difference between the left neighbour strip of the hottest strip and the right neighbour strip over the sum of these	asy_1	
	Barycentre in η: $\frac{\sum E_i \cdot \eta_i}{\sum E_i}$	bary_{S1}	
Second layer of EM Calorimeter	Shower width in layer 2 using a 3x5 window: $\sqrt{\frac{\sum E_i \eta_i^2}{\sum E_i} - \left(\frac{\sum E_i \eta_i}{\sum E_i}\right)^2}$	$w_{\eta 2}$	e/γ
	Energy in a 3x7 window around hottest cell over energy in a 7x7 window: $\frac{E_{3\times 7}^{S2}}{E_{7\times 7}^{S2}}$	R_η	e/γ
	Energy in a 3x3 window around hottest cell over energy in a 3x7 window: $R_\phi = \frac{E_{3\times 3}^{S2}}{E_{3\times 7}^{S2}}$	R_ϕ	e/γ
Third layer of EM Calorimeter	Ratio of the energy in the third layer to the total energy in the EM calorimeter	f_3	e
	Fraction of energy in the core (3x3 window) in third layer	$f_{3,\text{core}}$	
Multiple layers	Core energy: $E_{3\times 3}^{S0} + E_{15\times 3}^{S1} + E_{5\times 5}^{s2} + E_{3\times 5}^{S3}$	E_{core}	
	Ratio of energy in 3x3/3x7 cells: $\frac{E_{1\times 1}^{S0}+E_{3\times 1}^{S1}+E_{3\times 3}^{S2}+E_{3\times 3}^{S3}}{E_{3\times 3}^{S0}+E_{15\times 3}^{S1}+E_{3\times 7}^{S2}+E_{3\times 7}^{S3}}$	$r_{\text{33over37allcalo}}$	

Hadronic leakage	Energy leakage into first sampling of hadronic calorimenter: HEC0 (S8) + TileBar0 (S12) + TileExt0 (S18) + TileGap1 (S15) + TileGap2 (S16) in a 0.2×0.2 window around barycentre	E_{had1}	
	Leakage of the transverse energy in the hadronic calorimeter: $\frac{E_T^{\text{Had}}}{E_T}$ with $E_T = \frac{E_{\text{tot}}}{\cosh(\eta_2)}$ and $E_T^{\text{Had}} = \frac{E_{0.2\times0.2}^{\text{Had}}}{\cosh(\eta_2)}$ E_{tot}: total deposited energy in the entire calorimeter $\eta_2 = \left(\sum_{i,\,\text{layer}\,x} \eta_i E_i\right) / \left(\sum_{i,\,\text{layer}\,x} E_i\right)$, $x = 2$ or 6 depending on where more energy is deposited $E_{0.2\times0.2}^{\text{Had}}$: energy in the hadronic layers 7-20 excluding TileGap3 (S17) in a 0.2×0.2 around the barycentre	R_{had}	e/γ

Table 5.1.: The different shower shape variables and their descriptions. Modified from [25, 26]. Windows refer to windows in $\eta \times \phi$.

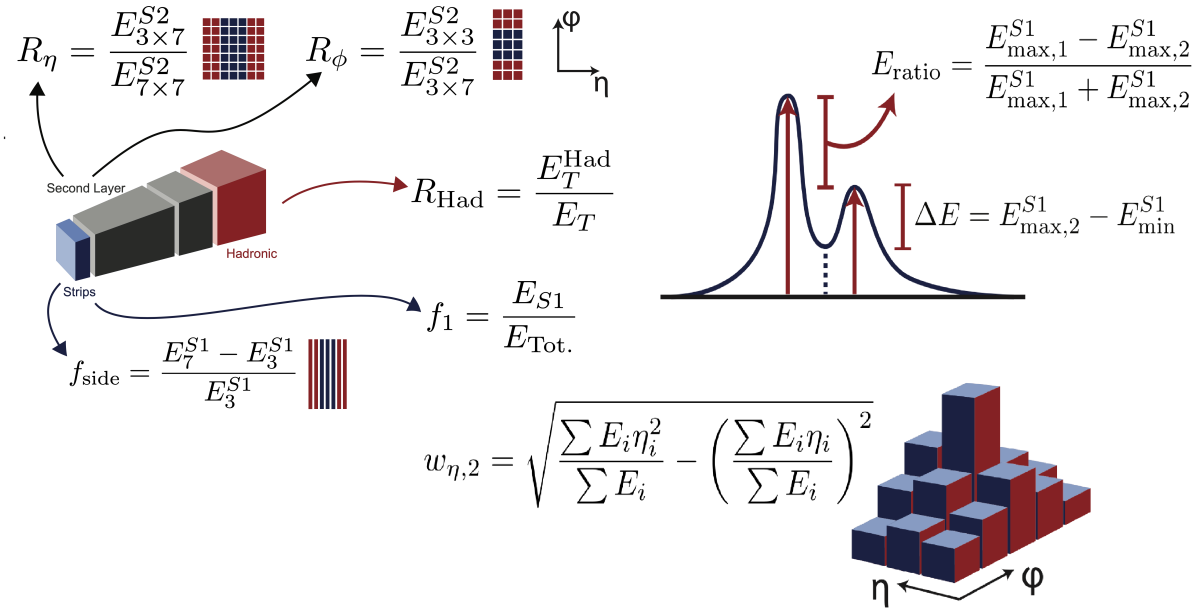

Figure 5.2.: Visualisation of some of the variables with the largest separation power R_η, R_ϕ, R_{Had}, f_1, f_{side}, E_{ratio}, ΔE and $w_{\eta 2}$ [28].

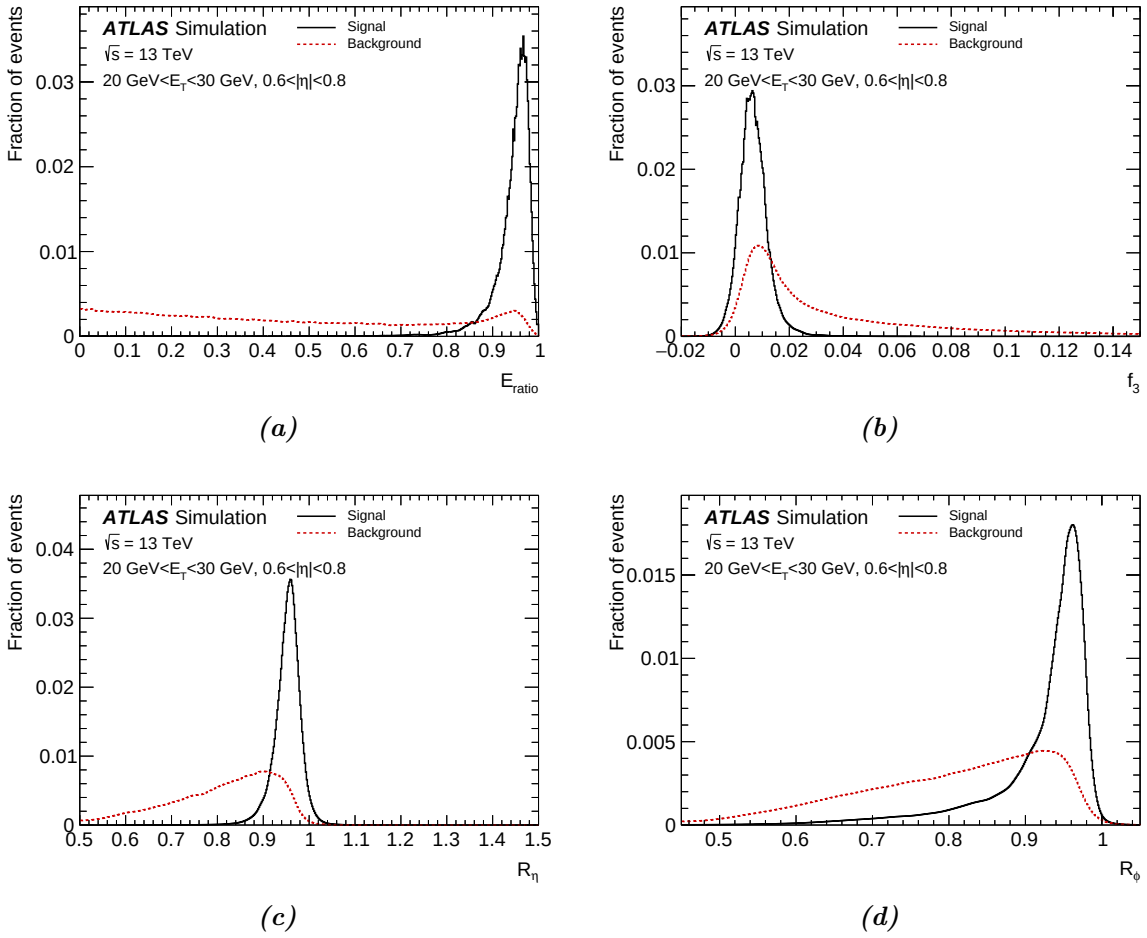

Figure 5.3.: Distributions of four of the shower shape variables E_{ratio}, f_3, R_η and R_ϕ for $20\,\text{GeV} < E_T < 30\,\text{GeV}$ and $0.6 < |\eta| < 0.8$ for signal determined from a $Z \to ee$ simulation sample and for background [26].

6. The ATLAS Fast Calorimeter Simulation

In order to compare theoretical predictions with data, events in the ATLAS experiment need to be simulated. The Monte Carlo production workflow for this includes the generation of the physical processes, the simulation and digitisation of the detector response and the reconstruction of the physical processes. The simulation of the detector response at hand, called GEANT4 [29], is very detailed and in good agreement with data. However, it is computationally expensive as it simulates each interaction individually. As the integrated luminosity in Run 3 and beyond will increase significantly, the required CPU resources with GEANT4 will outgrow the available capacity. This is because with more data, more Monte Carlo statistics is required, i.e. more samples are required with GEANT4. In Figure 6.1, the projected CPU consumption between 2020 and 2034 is shown for different scenarios.

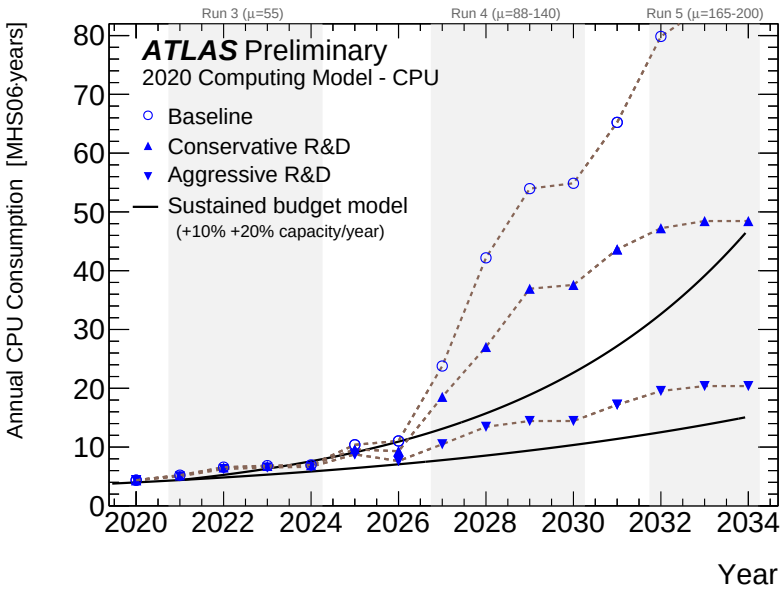

Figure 6.1.: Projected CPU requirement of ATLAS between 2020 and 2034 [30].

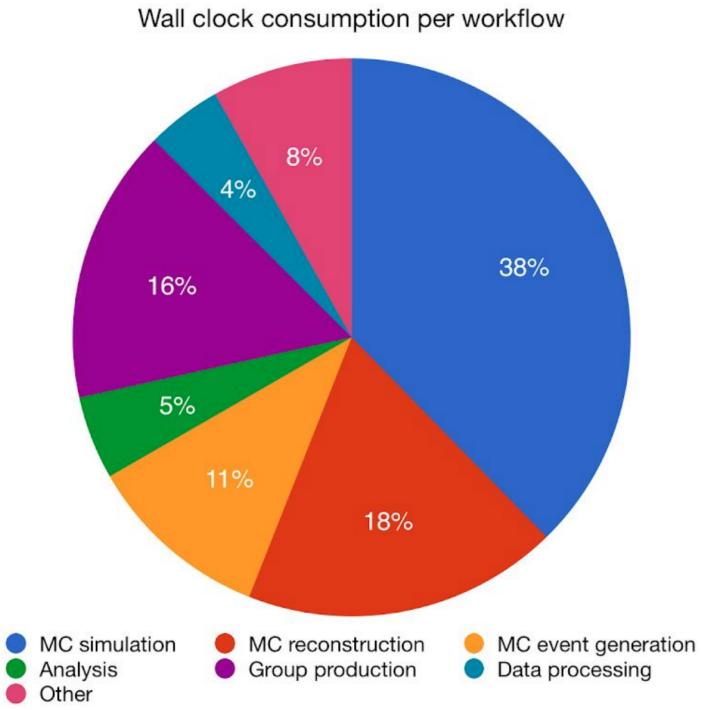

Figure 6.2.: Contribution of the event generation, detector simulation, reconstruction, user analysis and group production to the CPU consumption in ATLAS in 2018 [30].

It is clear that in the baseline scenario the required CPU will exceed the available resources with a sustained budget model considerably. Most of the computing power is used for the detector simulation as shown in Figure 6.2, of which 80-90% is used for the simulation of the calorimeter response. The event generation, reconstruction, digitisation, user analysis and group production contribute significantly less to the CPU consumption. It follows that a faster and less CPU-intensive simulation for the calorimeter is a crucial component to tackle the growing computing needs in the coming years.

A new fast simulation tool, called AtlFast3 [31], as the successor of AtlFastII [32] with the same CPU performance but improved accuracy has been employed recently by the ATLAS Collaboration. What makes both much faster than GEANT4 is the fact that only the ID is fully simulated and the simulation of the calorimeter response is parameterised, such that the simulation of individual particles traversing matter becomes obsolete. AtlFast3 includes two calorimeter simulation approaches. For electromagnetic showers of any energy and hadronic showers for energies $E_{\text{kin}}<16\,\text{GeV}$ and $E_{\text{kin}}>256\,\text{GeV}$, a parameterised modelling with FastCaloSimV2 is employed, in the following referred to as FastCaloSim. For pions in an energy range of $16\,\text{GeV}<E_{\text{kin}}<256\,\text{GeV}$, a generative adversarial network, known as FastCaloGan [33], is used. For pions with $E_{\text{kin}}<200\,\text{MeV}$ and other hadrons

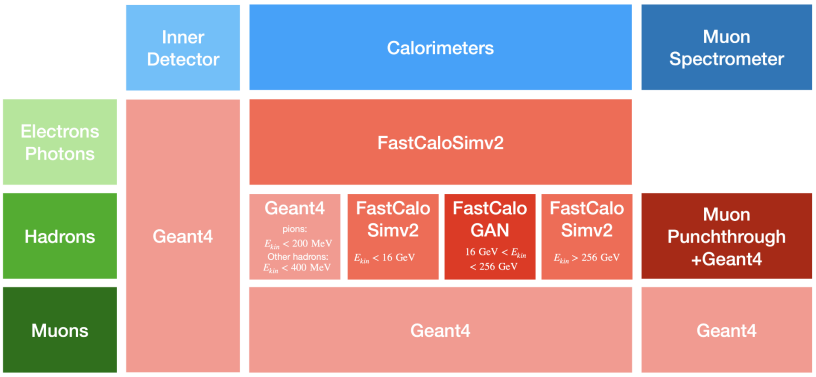

Figure 6.3.: Overview of the simulation tools and their field of application [34].

Energy [MeV]		
64	4096	262144
128	8192	524288
256	16384	1048576
512	32768	2097152
1024	65536	4194304
2048	131072	

Table 6.1.: The 17 logarithmically spaced energy grid points for the FastCaloSim samples.

with E_{kin}<400 MeV, GEANT4 is used. Secondary particles created in hadronic showers can leak to the MS. For these *punch through* particles, a separate parameterisation is derived using GEANT4 input samples for single pions. The propagation of these secondary particles through the MS as well as muon hits in the MS are simulated using GEANT4. In Figure 6.3, an overview of the different simulation components in AtlFast3 and their field of application is given.

In the following, the approach of FastCaloSim will be discussed in detail. For electromagnetic showers, electrons and photons are used for the parameterisation. For hadronic showers, only pions are considered. GEANT4 samples for single particles are produced for 17 logarithmically spaced grid points of total momentum in the range 64 MeV- 4 TeV listed in Table 6.1 for 100 equidistant bins of $|\eta| \in [0.0, 5.0]$. This η range slightly exceeds the calorimeter size and thereby includes particles which deposit only a fraction of their energy in the calorimeters. For energies in between the energy grid points, a piece-wise polynomial spline is fitted to the total energy response. For other shower shape properties, the parameterisation from the nearest lower or nearest higher energy grid point E_{kin} is randomly selected with a probability linear in $\log(E_{\text{kin}}[\text{MeV}])$. The detector response of single particles is parameterised independently for the lateral and longitudinal direction.

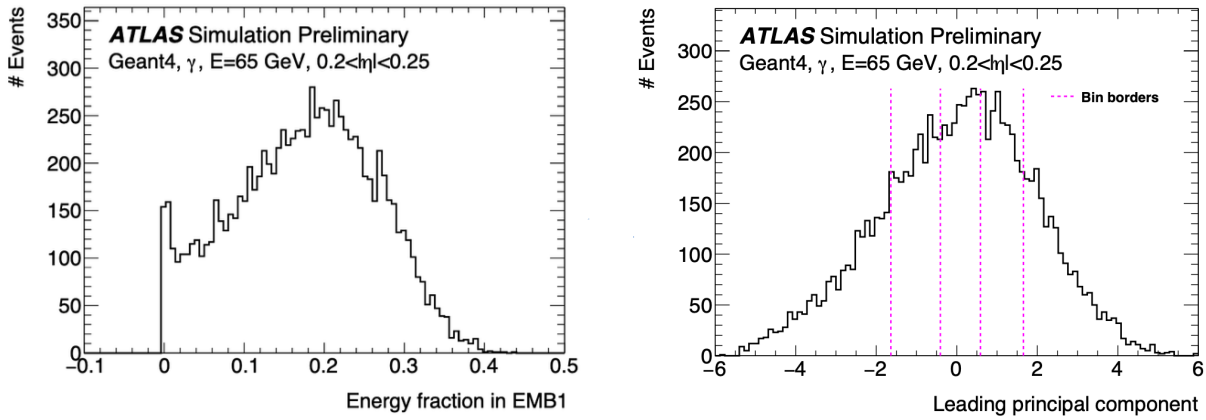

(a) *(b)*

Figure 6.4.: The distribution for the energy fraction in the electromagnetic barrel (a) for 65 GeV photons and the resulting distribution after the first PCA (b) [34].

6.1. Longitudinal shape parameterisation

In the following, the longitudinal shower parameterisation will be described. Here, the difficulty arises from the fact that the amount of energy deposited in the different layers is highly correlated. In order to parameterise the response for each layer separately, the energy is decorrelated using Principal Component Analysis (PCA) [35].

From a GEANT4 input sample with a fixed energy and a single η bin, the total energy and the fractions of energy in each layer is obtained as the input to the PCA. The distributions, for example for the energy fraction in the electromagnetic barrel shown in Figure 6.4a, are integrated and then transformed into Gaussian distributions using the inverse error function. A PCA matrix is constructed from these Gaussian distributions to get a set of linearly uncorrelated energies. This is referred to as *first PCA*. The resulting distribution for the energy fraction of the electromagnetic barrel is shown as an example in Figure 6.4b. The first PCA is used to divide the GEANT4 dataset into five PCA bins with roughly the same amount of events. This leads to an equal probability for an event to be assigned to one PCA bin for all bins. For yet further decorrelation, the PCA chain is carried out again within each bin separately, which is referred to as *second PCA*.

During the simulation, these steps are performed in reverse order. For each simulated particle, a PCA bin is randomly selected from a uniformly distributed probability density function. From the uncorrelated Gaussian distributions in the selected PCA bin, random numbers are generated and rotated using the inverse PCA matrix from the second PCA. Using the error function, the numbers are transformed into correlated numbers. From

these and the stored cumulative distributions, the energy distributions are obtained in each layer.

6.2. Lateral shape parameterisation

For the lateral shape parameterisation, the average lateral shower shape is constructed from GEANT4 input samples for each particle, energy grid point, η slice, calorimeter layer and bin of the first PCA. These 2D distributions of the deposited energy in a plane with η and ϕ coordinates computed with respect to the shower centre are used as a probability function to obtain the position of the hits during the simulation. Each hit is assigned the equal amount of deposited energy

$$E_{\text{hit}} = \frac{E_{\text{layer}}}{N_{\text{hits}}^{\text{layer}}},$$

where E_{layer} is the total energy deposited in the according layer, and N_{hits} is the number of hits in the layer. A random number following a Poisson distribution with an expected value λ is then used to generate the number of hits. The expected number of hits λ is derived to match the expected energy resolution $\sigma_E/E = a/\sqrt{E/\text{GeV}} \oplus c$ of the calorimeter technology:

$$\lambda = 1/\left(\sigma_E/E\right)^2 .$$

For electrons and photons as the showering particles, this results in a hit energy of about 10 MeV with a dominant stochastic term a of 10.1% in the electromagnetic calorimeter.

With hadronic showers, the fluctuations are much larger, which leads to large stochastic terms ($> 30\%$), which are dependent on the layer and η-region. For this reason, hits are assigned different amounts of energy according to weight factors constructed to better reproduce the observed RMS of GEANT4 distributions.

6.3. Simulation performance

Because the simulation time is already heavily reduced in AtlFastII compared to GEANT4, the advantage of AtlFast3 shows mainly in improvements in accuracy meaning many more analyses will be able to use AtlFast3. One of the main reasons for the shorter simulation time with AtlFastII and AtlFast3 is that it is no longer dependent on the energy of the

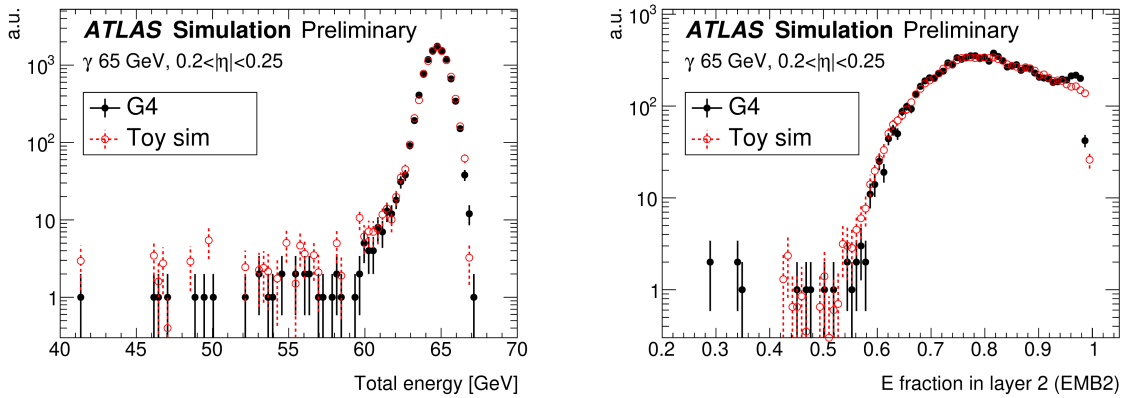

Figure 6.5.: Comparison of the energy simulation for 65 GeV photons between $0.20 < |\eta| < 0.25$ for GEANT4 and the standalone FastCaloSim [36].

particle and the lookup time in the parameterisation is constant regardless of energy. In contrast, with GEANT4 the simulation time increases with the energy because with increasing energy of the initial particle the number of particles in the shower increases, which are all simulated individually. For $t\bar{t}$ events, for example, the simulation of the pure calorimeter with AtlFast3 is faster by a factor of about 500 compared to GEANT4. For the full detector simulation, the reduction factor is about 10, and the simulation time is now dominated by the simulation of the ID.

To evaluate the simulation performance of AtlFast3 in regard to accuracy, one can compare the total energy as well as the energy fractions in each layer with GEANT4 as shown in Figure 6.5 for the electromagnetic barrel for 65 GeV photons in the region of $0.2 < |\eta| < 0.25$. The plots show excellent agreement between FastCaloSim an GEANT4.

Furthermore, the comparison of AtlFast3 with its predecessor as well as with GEANT4 for the modelling of physics objects can shed light on the simulation performance. As an example, the electron identification efficiency as a function of the reconstructed electron p_T is shown in Figure 6.6. The agreement with GEANT4 is improved for AtlFast3 compared to AtlFastII from 5% to 2% in a p_T range of 30-300 GeV except for photons at a very low p_T.

As an example for a reconstructed physics observable, Figure 6.7 shows the reconstructed Higgs boson mass for the diphoton decay with $p_T > 0.35\, m_{\gamma\gamma}$ and $p_T > 0.25\, m_{\gamma\gamma}$ and $|\eta|$<1.37 or $1.52 < |\eta| < 2.47$ as selection criteria. AtlFast3 shows improved modelling and is in agreement with GEANT4 within 5% compared to AtlFastII being in agreement with GEANT4 within a 10% tolerance.

However, while AtlFast3 shows excellent agreement to GEANT4 across a broad range of physics processes, some limitations remain. For instance, the distribution of the lead-

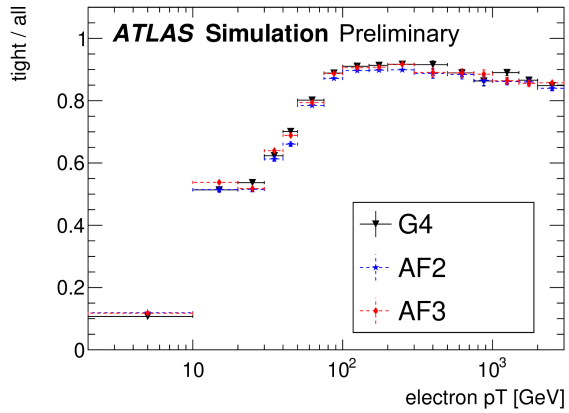

Figure 6.6.: Electron identification efficiency as a function of the reconstructed p_T [36].

ing UFO 1.0 jet [37] mass for $Z' \to t\bar{t}$ events with $m_{Z'} = 4\,\text{TeV}$ and a jet p_T>200 GeV shown in Figure 6.8 still shows some residual differences between GEANT4 and AtlFast3 although it is considerably improved compared to AtlFastII. For further improvement of the simulation in terms of accuracy in these high level variables, a deeper understanding on how reconstruction and clustering affects them is yet to be gained. For this reason, Chapter 8 deals with the clustering algorithm in ATLAS and the implementation of a simple clustering algorithm in the standalone FastCaloSim algorithm.

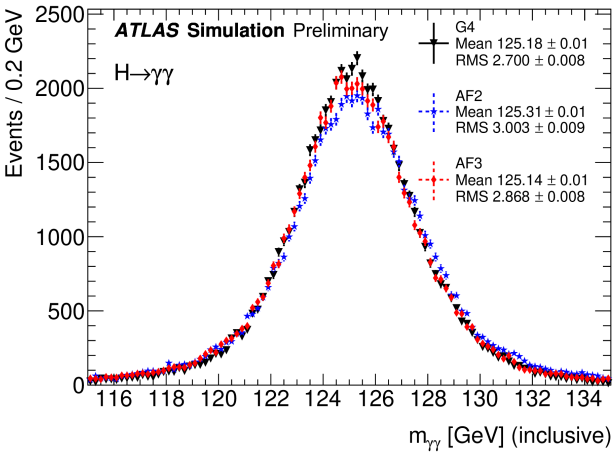

Figure 6.7.: The reconstructed invariant diphoton mass from a Higgs boson decay with two photons with $p_T > 0.35\,m_{\gamma\gamma}$ and $p_T > 0.25\,m_{\gamma\gamma}$ and $|\eta|$<1.37 or 1.52 < $|\eta| < 2.47$ as selection criteria [36].

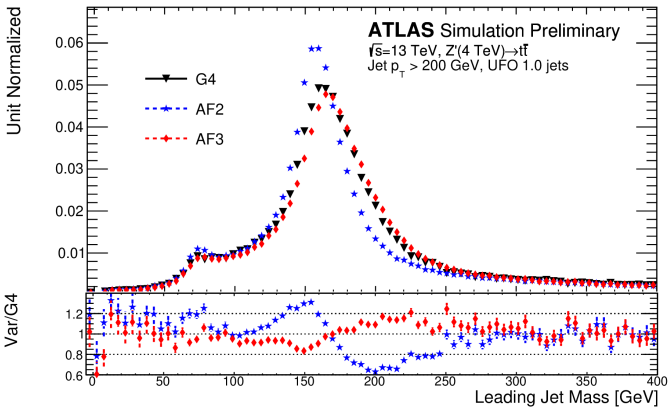

Figure 6.8.: The distribution for the leading UFO 1.0 jet mass for $Z' \to t\bar{t}$ events for GEANT4, AtlFastII and AtlFast3 in comparison [36].

7. Implementation of shower shape variables in FastCaloSim

As stated in Chapter 6, the major advantage of AtlFast3 compared to AtlFastII is the improved accuracy in the simulation. Nevertheless, remaining differences to data are observed, which is an intrinsic problem of the parameterised approach with the goal to reproduce GEANT4 because GEANT4 itself fails to reproduce some of the shower shape variables as observed in data. To further improve the simulation of electrons and photons, the shower shape variables introduced in Chapter 5 are expected to be tuned to real data. Since the development of a data tune requires a large number of small changes in the simulation which need to be evaluated for each software release, running the full ATLAS simulation and reconstruction chain is infeasible. Therefore, the shower shape variables should be implemented directly in the standalone FastCaloSim algorithm, which is the main aim of this Bachelor's thesis. The standalone FastCaloSim algorithm simulates the calorimeter only, neglects pile-up effects and noise, does not run any reconstruction or digitisation, and is not embedded in the Athena software package employed by ATLAS. This is much faster and more useful for investigations into the shower shape variables as well as for prospective work on the FastCaloSim algorithm.

In this chapter, the distributions of the shower shape variables obtained from the implementation in the standalone FastCaloSim algorithm for a total momentum of 65 GeV and a region of $0.20 < |\eta| < 0.25$ will be presented and discussed. A new C++ class was included in the algorithm to calculate and store the shower shape variables for easy access. The calculation of the variables can be enabled as an option when running the standalone FastCaloSim algorithm. The class offers the option to calculate the means of the distributions and save them to a text file, a second option to calculate the variables for each PCA bin separately and a third option to perform a clustering algorithm as described in Chapter 8.

In Table 7.1 the means of some of the most important variables are compared for the standalone FastCaloSim and the FastCaloSim implementation in Athena with noise turned off and without pile-up for 65 GeV photons in the region $0.20 < |\eta| < 0.25$ in or-

der to reassess the implementation. Except for bary_{S1}, asy_1, $r_{33\text{over}37\text{allcalo}}$, E_{mins1}, $E_{2\text{tsts1}}$ and ΔE they are in very good agreement, which yields to the conclusion that, generally speaking, the implementation of the shower shape variables has been successful. For the first three variables of these, further investigations into the origin of the differences are required. To improve the definition of the variables E_{mins1} and $E_{2\text{tsts1}}$ as well as E_{ratio} and ΔE, which depend on the former two, one would have to implement more subtle details in the algorithm. For example, the list of layer 1 cells used for the calculation is probably not quite correct. In the Athena software framework, for each η position, the cells with $\phi \leq 0.1$ are selected, merged and treated as a single cell. This usually corresponds to two merged physical calorimeter cells in reality.

Additionally, it is noteworthy that, when choosing the second maximum for variables like $E_{2\text{tsts1}}$, it is crucial to apply a local maximum criterion, that is to say to check whether the neighbour cells have less deposited energy.

7.1. FastCaloSim and Geant4 in comparison

In this section, the distributions of the shower shape variables calculated using the implementation in the standalone FastCaloSim algorithm will be compared for FastCaloSim and GEANT4 for 65 GeV electrons in the region $0.20 < |\eta| < 0.25$. The variables $w_{\eta 1}$, w_{stot}, f_{side}, E_{maxs1}, E_{mins1} are shown in Figure 7.1, $E_{2\text{ts1}}$, E_{ratio}, ΔE, f_1, $f_{1,\text{core}}$ and asy_1 in Figure 7.2, bary_{S1}, $w_{\eta 2}$, R_η, f_3 and $f_{3,\text{core}}$ in Figure 7.3 and E_{core}, $r_{33\text{over}37\text{allcalo}}$, E_{had1} and R_{had} in Figure 7.4.

In general, the distributions of FastCaloSim and GEANT4 are in very good agreement except for the layer 1 variables w_{stot} in Figure 7.1b, f_{side} in Figure 7.1c, E_{mins1} in Figure 7.1e, $E_{2\text{tsts1}}$ in Figure 7.1f, E_{ratio} in Figure 7.2b and ΔE in Figure 7.2c. For w_{stot} and f_{side}, noise effects play a large role because more strips are considered than for the other variables. The standalone FastCaloSim algorithm does not simulate noise but, when including noise effects, these differences vanish, so that for physics samples, they do not play a role.

The peaks in the distribution of E_{mins1} in Figure 7.1e can be explained by the fact that each hit in the FastCaloSim algorithm is assigned the same amount of discrete energy. So, the smallest peak corresponds to one hit in the strip. The second smallest peak corresponds to two hits and so on.

Moreover, the unexplained second peak at $w_{\eta 2} \simeq 0.0135$ in Figure 7.3b is also noteworthy. However, the mean of the distribution agrees reasonably accurate with the mean

variable	standalone FastCaloSim	Athena	relative difference in %
f_1	$0.18 \pm 0.091 \cdot 10^{-2}$	$0.18 \pm 0.042 \cdot 10^{-2}$	2 ± 0.51
f_3	$0.045 \cdot 10^{-1} \pm 0.054 \cdot 10^{-3}$	$0.035 \cdot 10^{-1} \pm 0.02 \cdot 10^{-3}$	30 ± 1.5
$f_{1,\text{core}}$	$0.14 \pm 0.071 \cdot 10^{-2}$	$0.13 \pm 0.031 \cdot 10^{-2}$	1.7 ± 0.53
$f_{3,\text{core}}$	$0.035 \cdot 10^{-1} \pm 0.045 \cdot 10^{-3}$	$0.037 \cdot 10^{-1} \pm 0.021 \cdot 10^{-3}$	4.8 ± 1.2
$E^{S1}_{3\times2}$ [GeV]	8.8 ± 0.046	8.8 ± 0.02	0.17 ± 2.1
$E^{S1}_{15\times2}$ [GeV]	11 ± 0.057	11 ± 0.025	0.38 ± 2.6
$E^{S2}_{3\times3}$ [GeV]	49 ± 0.06	49 ± 0.026	0.19 ± 2.6
$E^{S2}_{3\times5}$ [GeV]	50 ± 0.061	50 ± 0.027	0.2 ± 2.6
$E^{S2}_{5\times5}$ [GeV]	51 ± 0.061	51 ± 0.027	0.19 ± 2.7
$E^{S2}_{3\times7}$ [GeV]	50 ± 0.061	50 ± 0.027	0.2 ± 2.7
$E^{S2}_{7\times7}$ [GeV]	52 ± 0.061	52 ± 0.027	0.19 ± 2.7
$w_{\eta1}$	$0.57 \pm 0.098 \cdot 10^{-2}$	$0.51 \pm 0.019 \cdot 10^{-2}$	10 ± 0.19
$w_{\eta2}$	$0.01 \pm 0.015 \cdot 10^{-3}$	$0.088 \pm 0.02 \cdot 10^{-4}$	19 ± 0.17
f_{side}	$0.14 \pm 0.048 \cdot 10^{-2}$	$0.14 \pm 0.014 \cdot 10^{-2}$	1.7 ± 0.34
asy_1	$0.034 \pm 0.043 \cdot 10^{-1}$	$0.084 \pm 0.042 \cdot 10^{-2}$	96 ± 5.1
bary_{S1}	$0.035 \pm 0.023 \cdot 10^{-1}$	$0.23 \pm 0.092 \cdot 10^{-3}$	98 ± 1
w_{stot}	$1.6 \pm 0.028 \cdot 10^{-1}$	$1.5 \pm 0.091 \cdot 10^{-2}$	4.8 ± 0.2
E_{mins1} [GeV]	$0.2 \pm 0.043 \cdot 10^{-1}$	$0.045 \pm 0.018 \cdot 10^{-2}$	$3.3 \cdot 10^2 \pm 9.4$
E_{maxs1} [GeV]	5.5 ± 0.029	5.7 ± 0.013	2.8 ± 1.3
E_{2tsts1} [GeV]	$0.37 \pm 0.078 \cdot 10^{-1}$	$0.068 \cdot 10^{-1} \pm 0.02 \cdot 10^{-2}$	$4.4 \cdot 10^2 \pm 11$
ΔE [GeV]	$0.18 \pm 0.078 \cdot 10^{-1}$	$0.023 \pm 0.078 \cdot 10^{-3}$	$6.9 \cdot 10^2 \pm 34$
$r_{\text{33over37allcalo}}$	$0.94 \cdot 10^{-1} \pm 0.031 \cdot 10^{-2}$	$0.052 \pm 0.081 \cdot 10^{-3}$	$1.7 \cdot 10^3 \pm 0.62$
E_{core} [GeV]	$63 \cdot 10^{-1} \pm 0.018$	$62 \pm 0.085 \cdot 10^{-1}$	0.53 ± 0.86
R_η	$0.97 \pm 0.05 \cdot 10^{-3}$	$0.97 \pm 0.022 \cdot 10^{-3}$	0.098 ± 0.056
R_ϕ	$0.97 \pm 0.052 \cdot 10^{-3}$	$0.97 \pm 0.022 \cdot 10^{-3}$	0.01 ± 0.057
E_{ratio}	$0.87 \pm 0.023 \cdot 10^{-1}$	$0.97 \pm 0.01 \cdot 10^{-2}$	11 ± 0.24
R_{had}	$0.024 \pm 0.093 \cdot 10^{-3}$	$0.035 \pm 0.076 \cdot 10^{-3}$	31 ± 2.6
E_T^{Had} [GeV]	$0.15 \pm 0.058 \cdot 10^{-1}$	$0.21 \pm 0.038 \cdot 10^{-1}$	27 ± 2.8

Table 7.1.: Means of some of the most important shower shape variables for the standalone FastCaloSim and the Athena implementation for 65 GeV photons in the region $0.20 < |\eta| < 0.25$.

of the distribution obtained from the full Athena simulation. Additionally, because the input sample covers an η range of $0.20 < |\eta| < 0.25$ only, the distribution of bary_{S1} shown in Figure 7.3a only ranges from 0.2 to 0.25. The hadronic leakage for an electromagnetic shower is naturally very low, which is why the values of E_{had1} and R_{had} shown in Figure 7.4c and 7.4d are very small.

For the energy window variables, four examples of a 3×3 and a 3×2 window in the presampler (S0) and the three layers of the electromagnetic barrel (S1, S2, S3) are shown

in Figure 7.5. The distributions for the other sizes of the windows used for particle identification can be found in Section A.1.1 of the Appendix. Again, the distributions with FastCaloSim and GEANT4 are in good agreement. Comparing the four distributions, it is noteworthy that electrons clearly deposit most of their energy in the second layer of the electromagnetic barrel and only very little in the presampler and the third layer of the electromagnetic barrel. This is as intended with the structure of the calorimeter as described in Chapter 4.4. This observation is also supported by the distributions of the energy fractions in the presampler and the first two layers of the electromagnetic barrel over the sum of the energy in the presampler and the first two layers of the electromagnetic barrel shown in Figure 7.6. The distributions of the energy fractions over the whole calorimeter can be found in Section A.1.1 of the Appendix. They do not differ significantly from the distributions of the energy fractions over the first three layers for electrons and photons as most of the energy is deposited in the second layer.

All these distributions for FastCaloSim and GEANT4 in comparison for 65 GeV photons and pions can be found in Section A.1.2 and A.1.3 of the Appendix. The distributions for pions are not in very good agreement due to the poor modelling of single pions in FastCaloSim. However, these observed differences vanish when comparing reconstructed physics objects such es jets or taus, for which the accuracy in FastCaloSim is excellent as mentioned in Chapter 6.3.

Generally speaking, the distributions look reasonable and are in very good agreement for FastCaloSim and GEANT4. Since GEANT4 itself fails to reproduce some of the shower shape variables as observed in data, the next step towards a more accurate simulation of the shower shape variables is to tune the distributions to data.

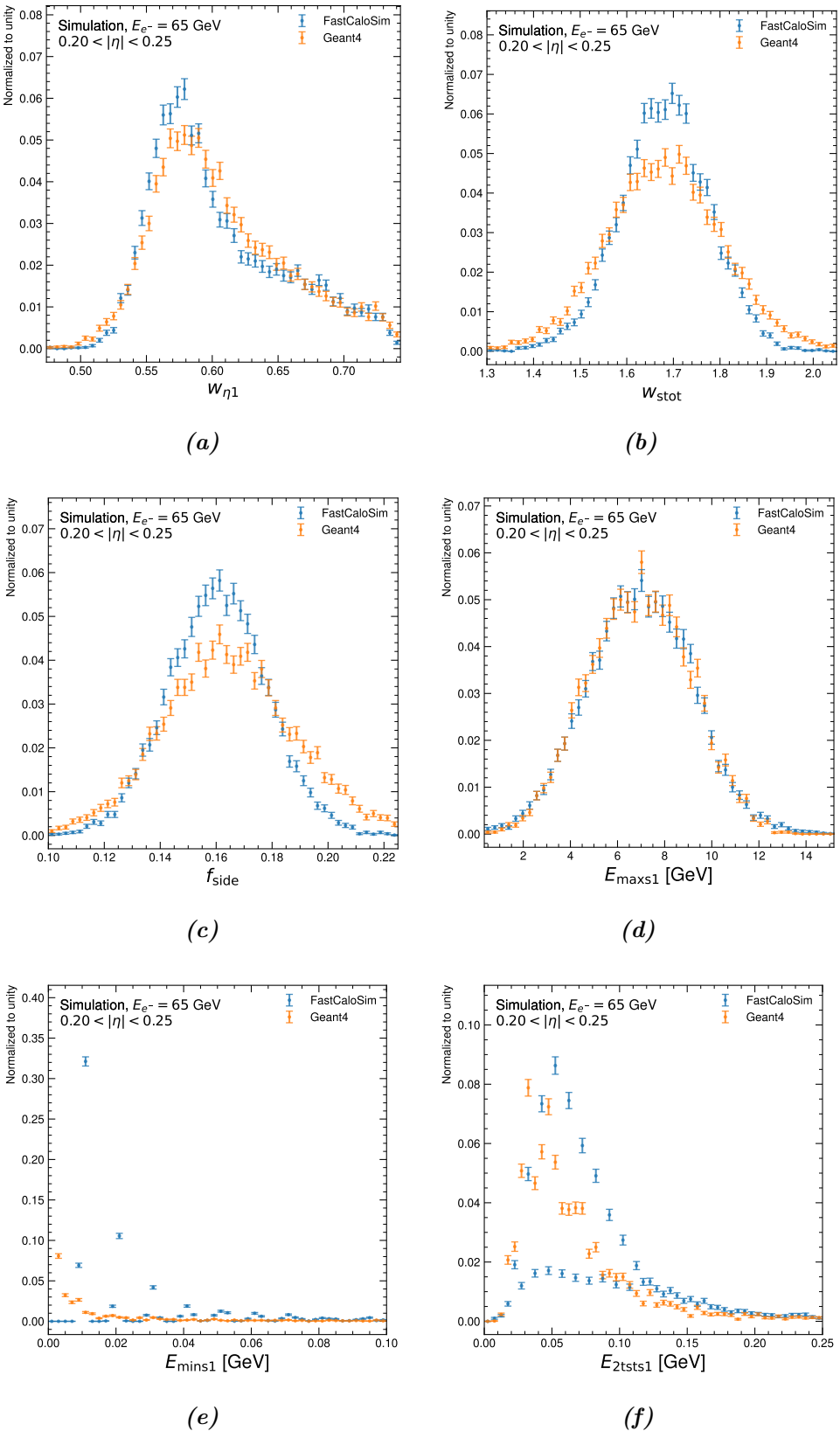

Figure 7.1.: Distributions of the shower shape variables $w_{\eta 1}$, w_{stot}, f_1, E_{maxs1}, E_{mins1} and E_{e2tsts1} for FastCaloSim and GEANT4 in comparison for 65 GeV electrons in the region $0.20 < |\eta| < 0.25$ calculated with the implementation in the standalone FastCaloSim algorithm.

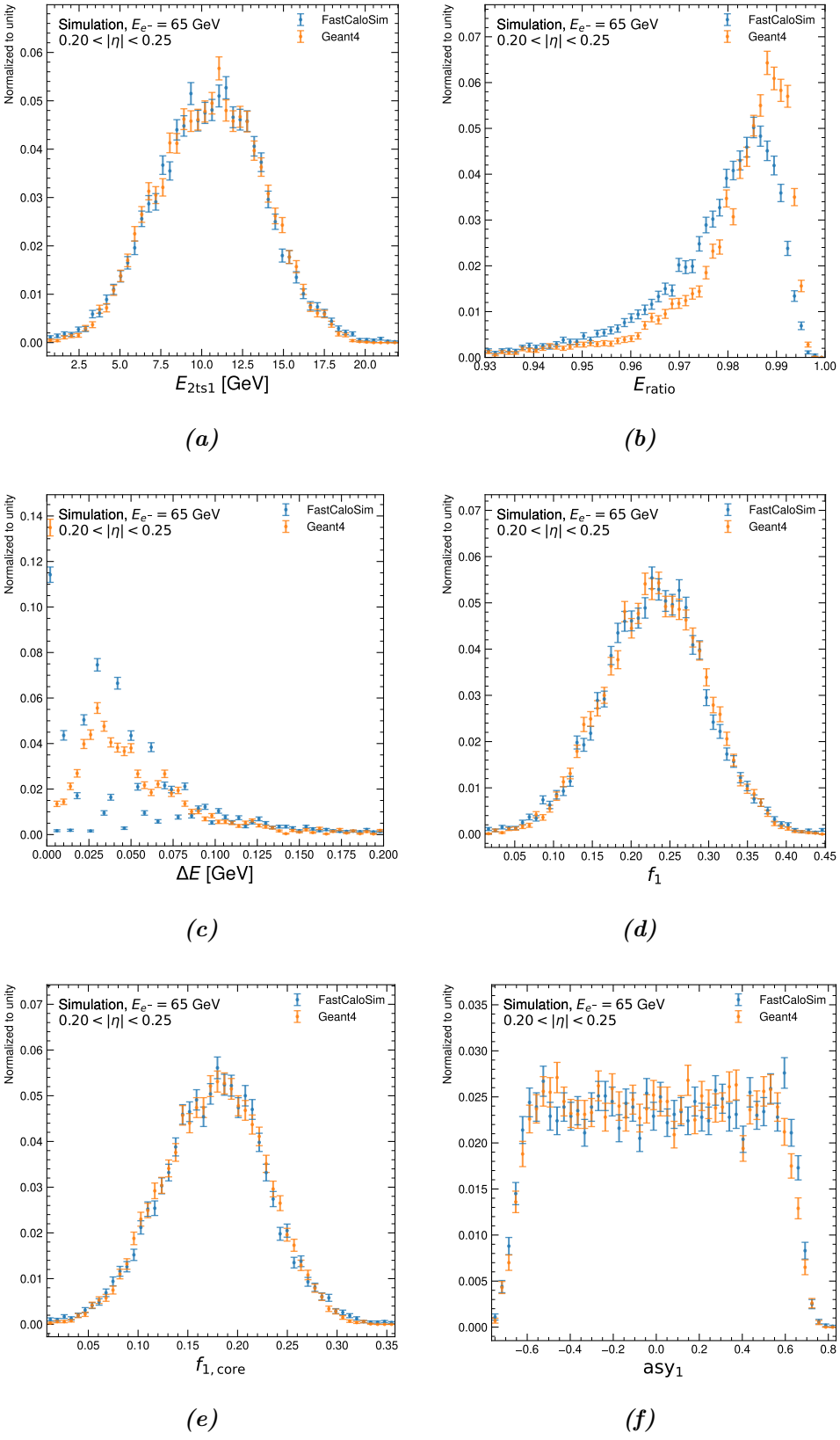

Figure 7.2.: Distributions of the shower shape variables E_{e2ts1}, E_{ratio}, ΔE, f_1, $f_{1,core}$ and asy_1 for FastCaloSim and GEANT4 in comparison for 65 GeV electrons in the region $0.20 < |\eta| < 0.25$ calculated with the implementation in the standalone FastCaloSim algorithm.

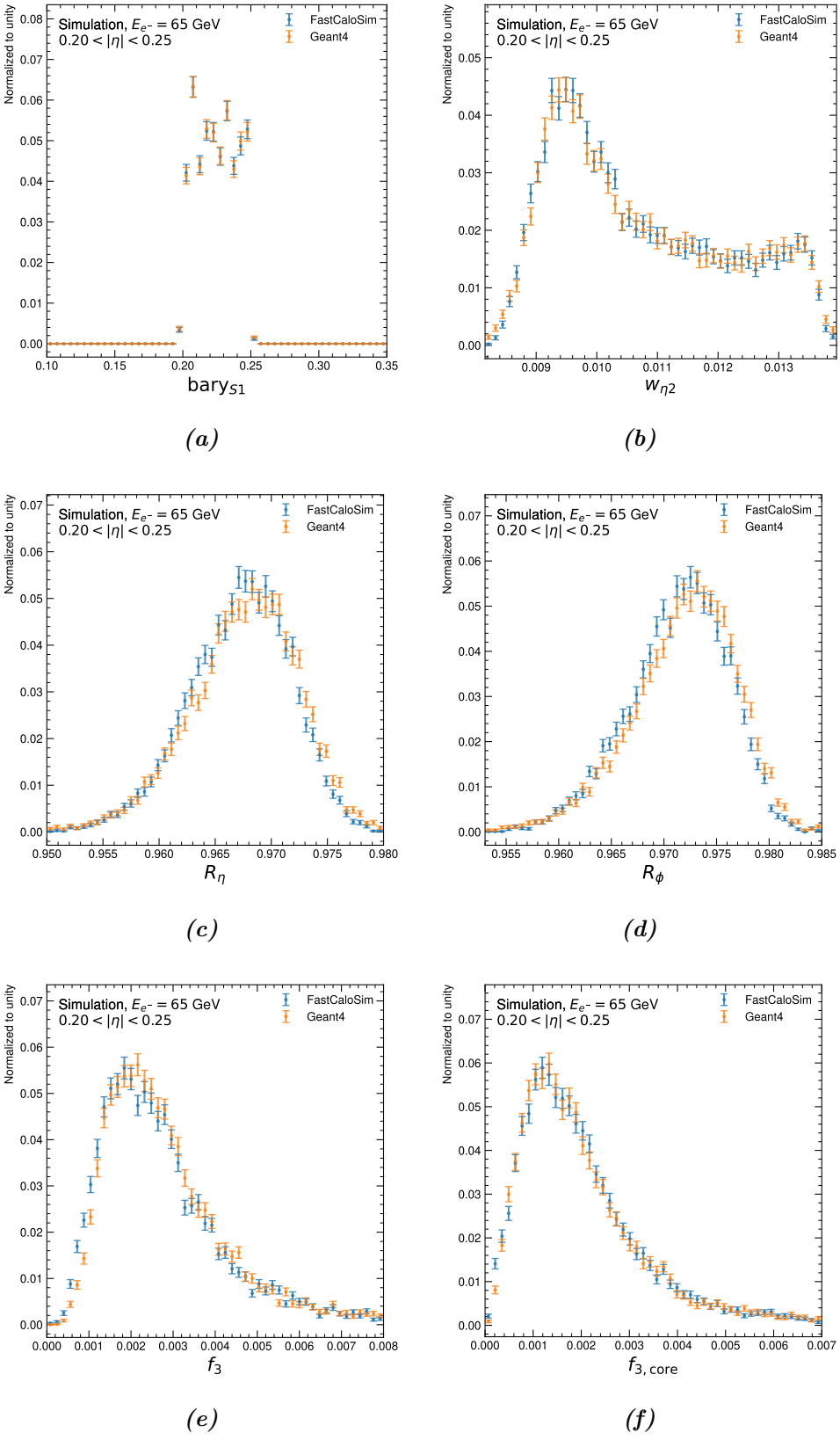

Figure 7.3.: Distributions of the shower shape variables bary$_{S1}$, $w_{\eta 2}$, R_η, R_ϕ, f_3 and $f_{3,\text{core}}$ for FastCaloSim and GEANT4 in comparison for 65 GeV electrons in the region $0.20 < |\eta| < 0.25$ calculated with the implementation in the standalone FastCaloSim algorithm.

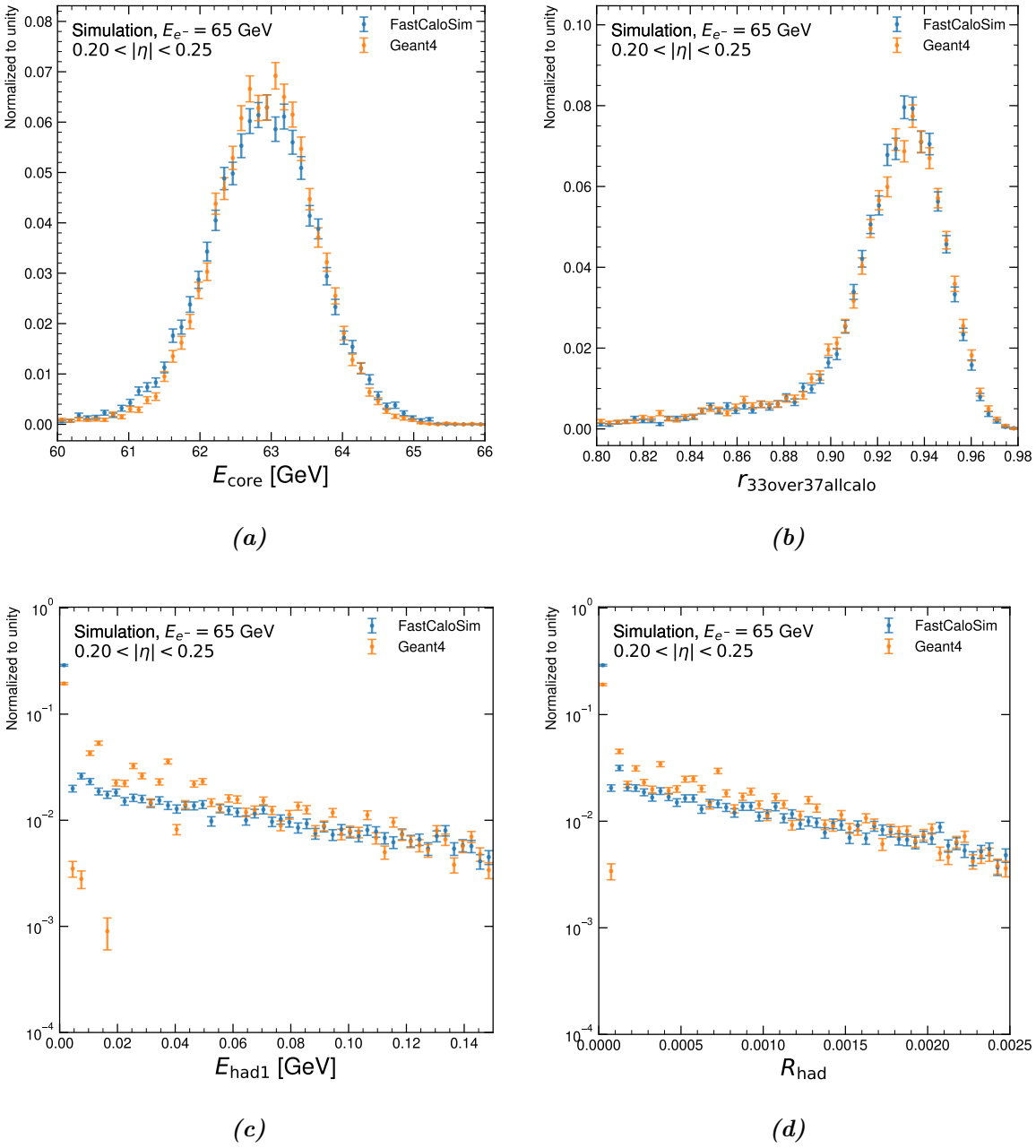

Figure 7.4.: Distributions of the shower shape variables E_{core}, $r_{33\text{over}37\text{allcalo}}$, E_{had1} and R_{had} for FastCaloSim and GEANT4 in comparison for 65 GeV electrons in the region $0.20 < |\eta| < 0.25$ calculated with the implementation in the standalone FastCaloSim algorithm.

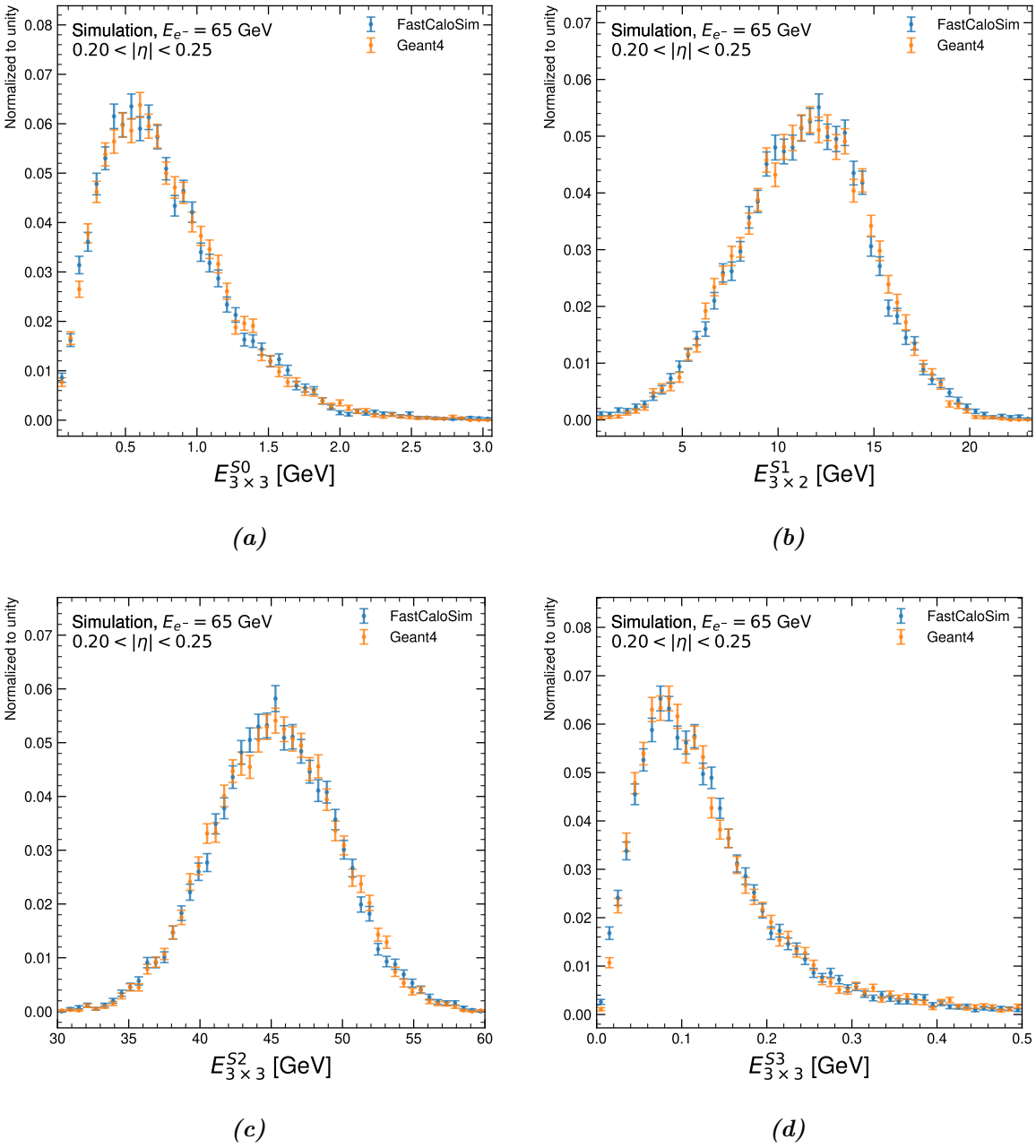

Figure 7.5.: Distributions for an energy window of 3×3 and 3×2 in $\eta \times \phi$ around the cell with the most deposited energy in the presampler (S0) and in the three layers of the electromagnetic barrel (S1, S2 and S3) for 65 GeV electrons in the region $0.20 < |\eta| < 0.25$ for FastCaloSim and GEANT4 in comparison.

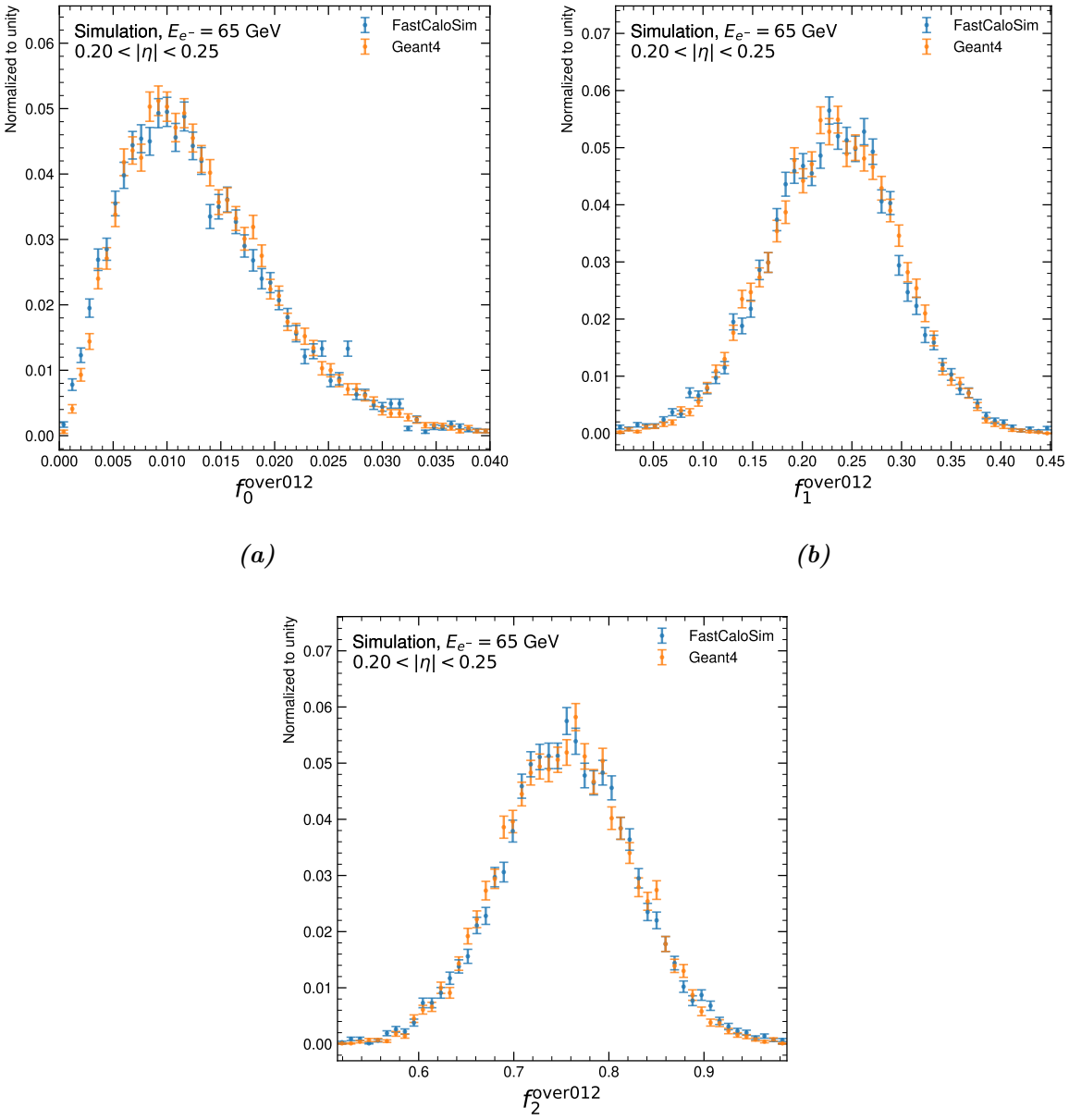

(a) *(b)*

(c)

Figure 7.6.: Distributions of the fractions of energy in presampler (S0) and the first two layers of the electromagnetic barrel (S1 and S2) over the sum of the energies of these three layers for 65 GeV electrons in the range of $0.20 < |\eta| < 0.25$ for FastCaloSim and GEANT4 in comparison.

7.2. Electrons and photons in comparison

In this section, the distributions of the most important shower shape variables calculated with the implementation in the standalone FastCaloSim algorithm will be compared for 65 GeV electrons and photons in the region $0.20 < |\eta| < 0.25$ and are shown in Figure 7.7. The distributions for the rest of the variables for electrons and photons in comparison can be found in the Section A.2 of the Appendix.

The differences in the shower shapes can be explained by the fact that electrons lose their energy in a continuous fashion in which atoms or molecules of the detector material are ionised whereas photons may traverse matter without interacting for a certain distance [38]. This leads to two consequences for the shape of the induced particle shower. First of all, photons deposit their energy, on average, deeper inside the detector, which is confirmed by the distributions of the energy fractions in the presampler (S0) and the first two layers of the electromagnetic calorimeter (S1 and S2) as shown in Figure 7.8. Second of all, the fluctuations in the amount of deposited energy are larger for photon induced particle showers. From the shift of the distributions for photons in Figure 7.7, it is clear that photon induced showers are more narrow than electron induced showers. The hadronic leakage R_{had} shown in Figure 7.7f is in both cases very small as expected for all electromagnetic showers.

Overall, the distributions are well-behaved and reasonable, and therefore confirm the conclusion that the implementation of the shower shape variables has been successful.

7.3. Electromagnetic and hadronic showers in comparison

In this section, the distributions of the most important shower shape variables calculated with the implementation in the standalone FastCaloSim algorithm will be compared for FastCaloSim for electromagnetic and hadronic showers. In Figure 7.9, the distributions for 65 GeV electrons, photons and pions in the region $0.20 < |\eta| < 0.25$ are shown. The distributions for the rest of the variables for electromagnetic and hadronic showers in comparison can be found in Section A.3 of the Appendix.

Generally speaking, all variables show very good separation power as the distributions for pions look significantly different from the distributions for electrons and pions. This confirms that the shower shape variables are suitable for electron and photon identification.

Variables like w_{stot}, R_ϕ and $w_{\eta 2}$ are shown in Figures 7.9c, 7.9d and 7.9e and show that

hadronic showers are broader than electromagnetic showers. The hadronic leakage R_{had} shown in Figure 7.9f has naturally a peak at almost one for hadronic showers and at zero for electromagnetic showers.

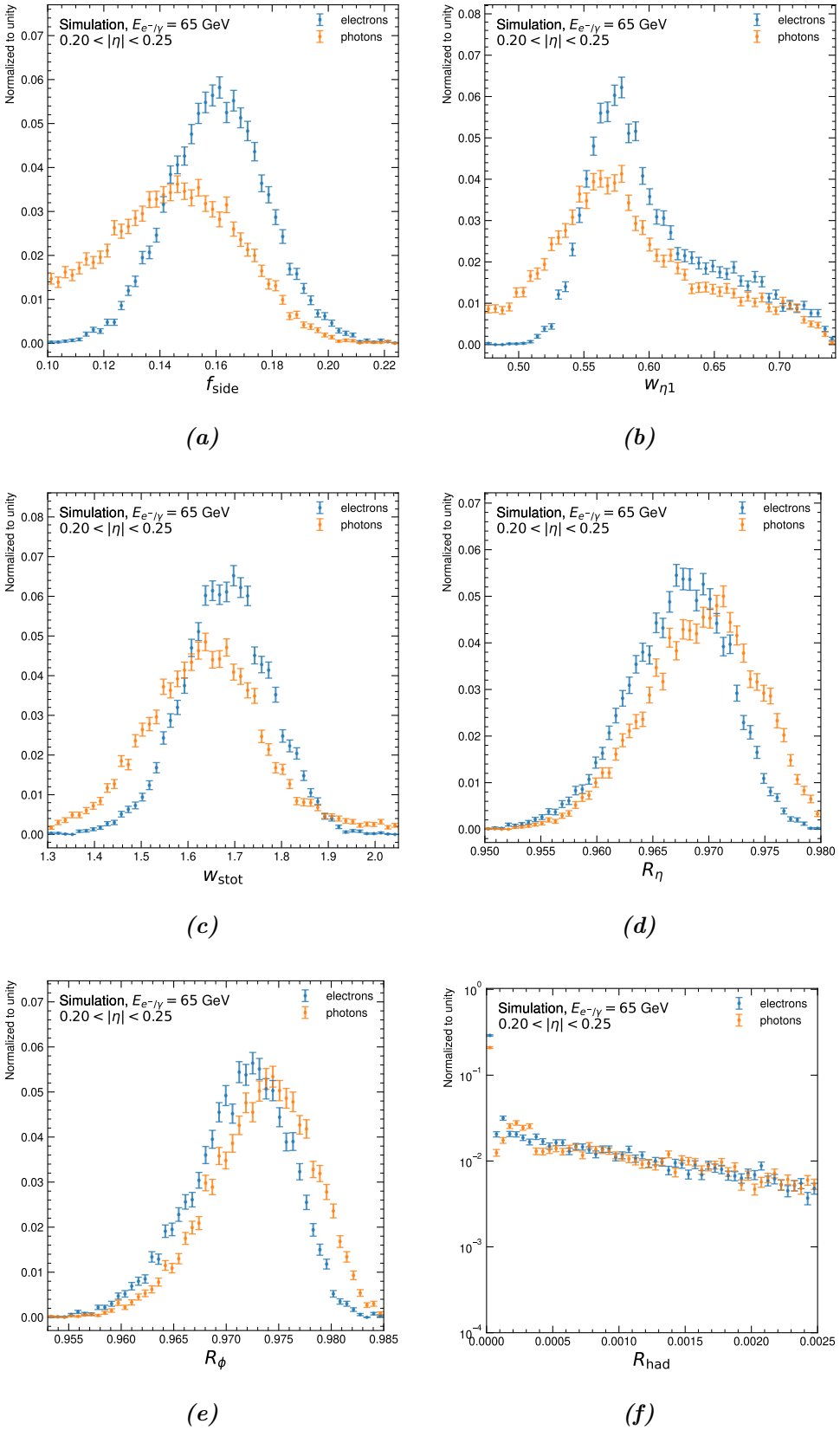

Figure 7.7.: Distributions for some of the most important shower shape variables f_{side}, $w_{\eta 1}$, w_{stot}, R_η, R_ϕ and R_{had} for 65 GeV electrons and photons in the region $0.20 < |\eta| < 0.25$ in comparison.

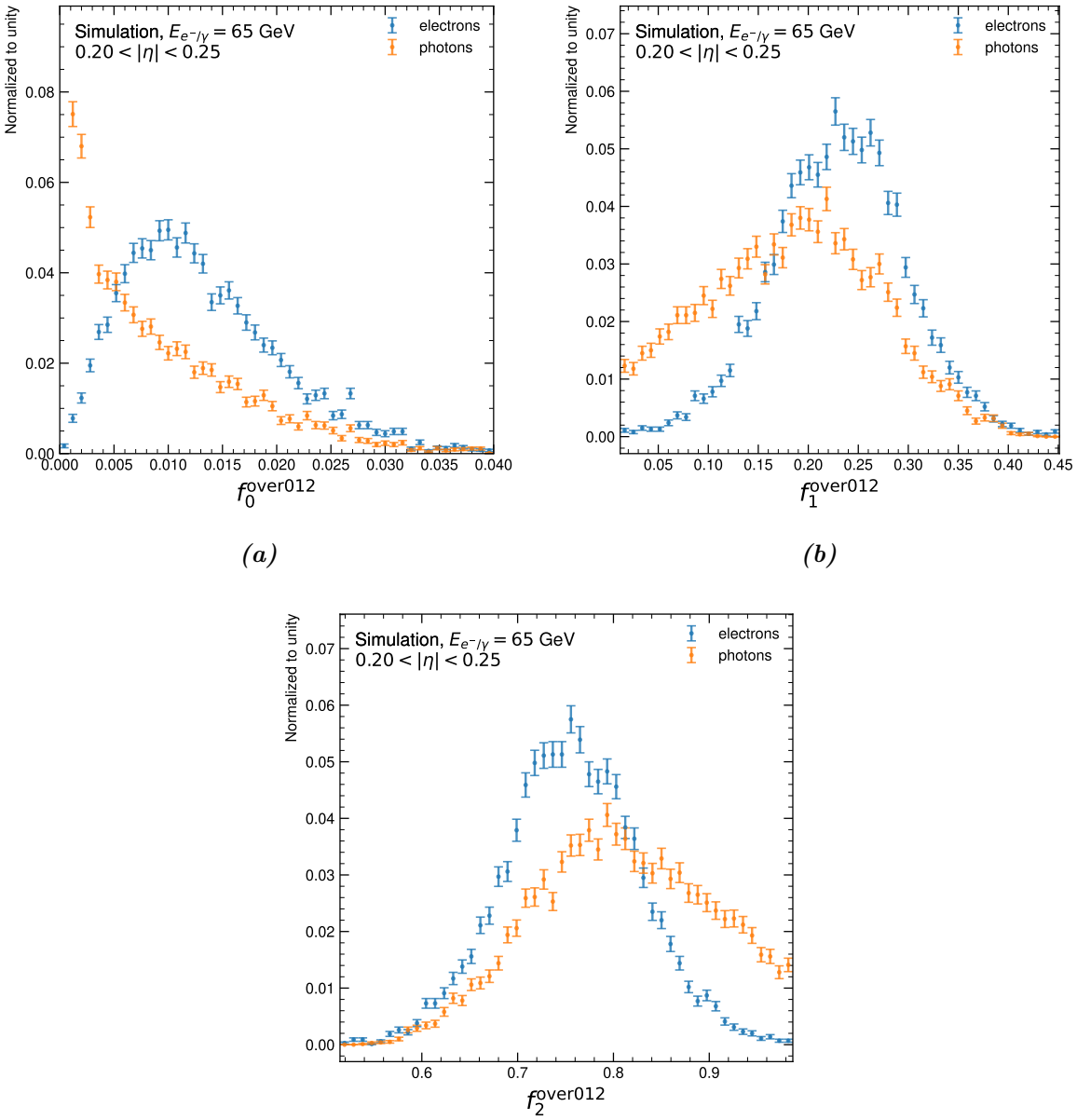

Figure 7.8.: Distributions of the fractions of energy in presampler (S0) and the first two layers of the electromagnetic barrel (S1 and S2) over the sum of the energies of these three layers for 65 GeV electrons and photons in the region $0.20 < |\eta| < 0.25$ in comparison.

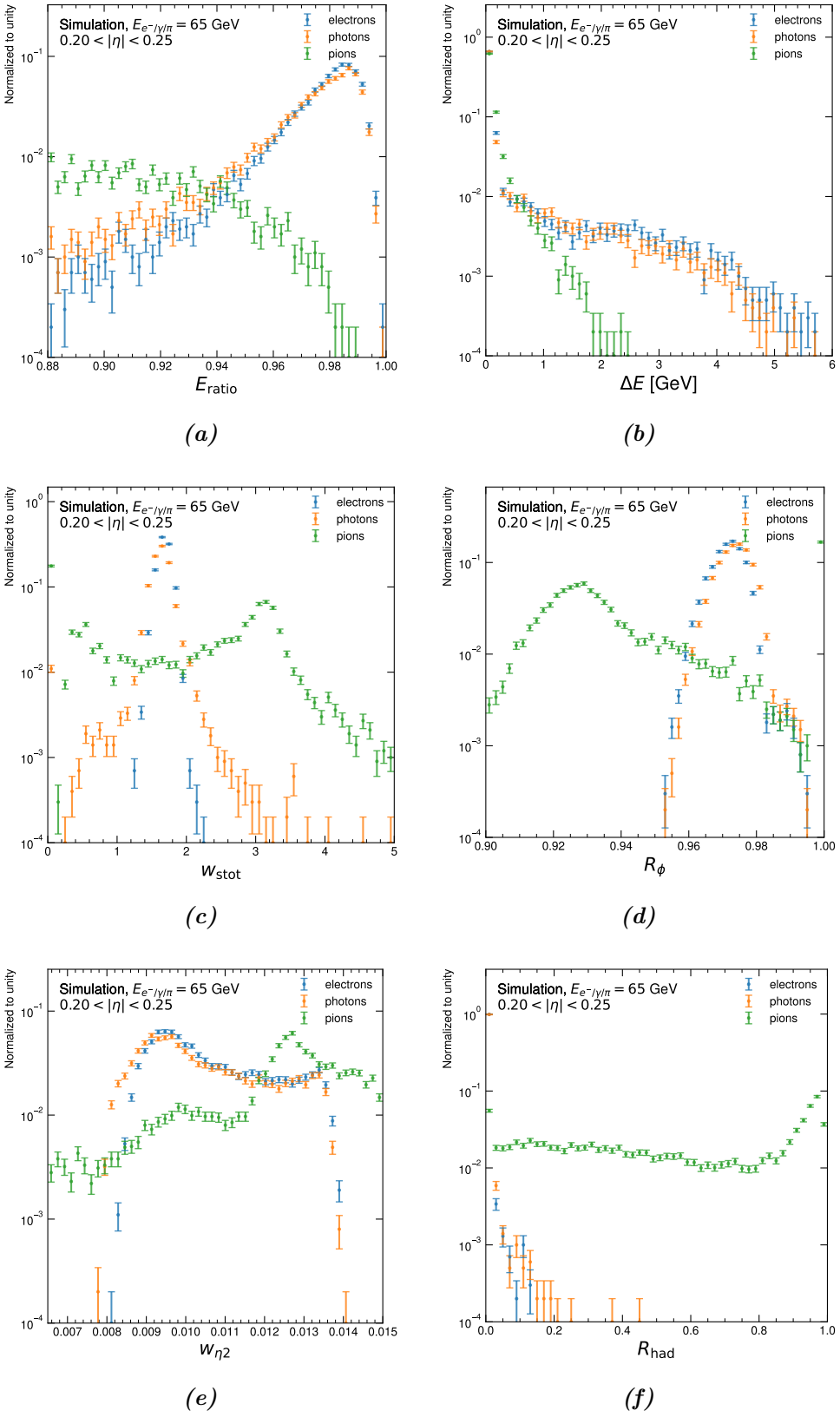

Figure 7.9.: Distributions for E_{ratio}, ΔE, w_{stot}, R_η, $w_{\eta 2}$ and R_{had} for 65 GeV electrons, photons and pions in the region $0.20 < |\eta| < 0.25$ in comparison.

8. Integration of a clustering algorithm in FastCaloSim

For the reconstruction of physics objects in ATLAS, the deposited energies in the calorimeter cells are grouped together. This is called clustering [39, 40] and is aimed to suppress noise. Two different algorithms are used for that purpose, a sliding-window algorithm for electron and photon reconstruction and a topological algorithm for jet and missing transverse energy reconstruction. A simple version of the latter was implemented in the standalone FastCaloSim algorithm for this thesis. In this chapter, the full algorithm as well as the implemented simple version will be described.

8.1. The topological clustering algorithm in ATLAS

The topological algorithm groups neighbouring cells into clusters if their energies are significant compared to the expected noise. This includes two steps, the cluster maker and the cluster splitter. In the first step, a list of seed cells is prepared, to which all cells with a signal to noise ratio above a certain threshold t_{seed} are added. Then, the neighbouring cells to a seed cell are added to the corresponding cluster of the seed cell if their signal to noise ratio is above a certain threshold t_{cell}. The neighbour cells are added to a neighbour seed list if their signal to noise ratio is above a third threshold $t_{\text{neighbour}}$, which is then used as a new seed list. In this way, the neighbours of the neighbours etc. are added and a new neighbour list is prepared repeatedly until the list is empty. If a cell is a neighbour to be included in more than one cluster, these clusters are merged. In the final step of the cluster maker, all clusters are removed with a transverse energy E_T less than a threshold, which is defined as the sum of the transverse energy in the cells in the cluster. There are two types of topological clusters in ATLAS: "633" for the reconstruction of EM clusters with considerably higher energy than the noise with minimum fake rate and "420" for the reconstruction of low energy clusters. The parameters for these two types of the algorithm are shown in Table 8.1.

Parameter	EM 633	Had 420
Calorimeters	EM only	All
Cluster cut before splitting	$E_T > 5\,\text{GeV}$	$\lvert E_T\rvert > 0\,\text{GeV}$
t_{seed}	$6\sigma_{\text{noise}}$	$4\sigma_{\text{noise}}$
$t_{\text{neighbour}}$	$3\sigma_{\text{noise}}$	$2\sigma_{\text{noise}}$
t_{cell}	$3\sigma_{\text{noise}}$	$0\sigma_{\text{noise}}$

Table 8.1.: Parameters for the two cluster types used in ATLAS [40].

In some cases, clusters for individual particles are not isolated but adjacent or even overlap. In this case, they are all included in a single large cluster after the first step of the clustering algorithm. For this reason, these clusters are separated in the second step of the topological clustering algorithm if local maxima can be located. A set of cells in a cluster is defined as a local maximum if their sum of energies is greater than 500 MeV and the energy is greater than the energy of the neighbouring cells. Then, a cluster is constructed around the local maximum by adding the adjacent cells used before. No threshold is applied here, and adjacent or overlapping clusters are not merged. Shared cells are removed from the neighbour list and all clusters. Then they are added to a shared cell list. Cells on this list are assigned to the two most energetic clusters with weights according to the energy of the two clusters and the distance of the shared cell to the cluster centroids. This sharing algorithm ensures that each cell is shared by two clusters at most. In Figure 8.1, the topological cluster formation in the forward calorimeter for a simulated dijet event with at least one jet entering the calorimeter is visualised.

8.2. Clustering in FastCaloSim

A simple version of the topological clustering algorithm was implemented in the standalone FastCaloSim algorithm as part of this thesis in order to compare GEANT4 and FastCaloSim and find possible residual differences. As there is no simulation of noise in the standalone FastCaloSim algorithm, the thresholds are not defined with regard to the signal to noise ratio but are set as absolute values for the energy so that they roughly correspond to the signal to noise thresholds. For the seed list, a threshold of $E_{\text{seed}}^{\text{thr}} = 300\,\text{MeV}$ and for the neighbour cells to be added to the clusters a threshold of $E_{\text{core}}^{\text{thr}} = 100\,\text{MeV}$ is applied. There is no additional threshold for the cells that are added to the neighbour list so that all neighbours are considered as new seeds. The clusters are merged if they have at least one shared cell. The algorithm does not perform cluster splitting.

The number of constructed clusters with this implementation of the clustering algorithm

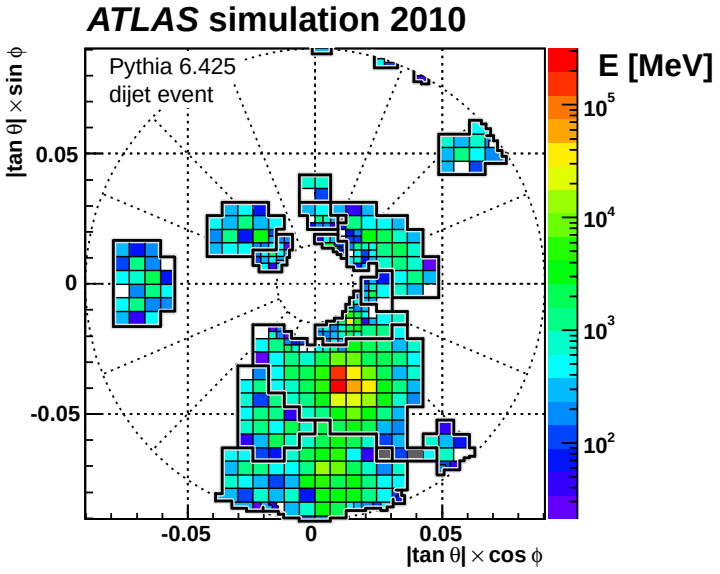

Figure 8.1.: Topological cluster formation in the forward calorimeter for a simulated dijet event with at least one jet entering this calorimeter [39].

in the standalone FastCaloSim is shown in Figure 8.3a for 131 GeV charged pions. In general, the distribution is in the expected order of magnitude although the peak is slightly too low and the tail is slightly too short when comparing to the distribution in Figure 8.2 showing the number of reconstructed clusters for simulated charged and neutral pions with 100 GeV at $|\eta| = 0.3$. The distribution for FastCaloSim is narrower and has a larger peak at 2 than for the distribution with GEANT4. These significant differences could indicate problems in the shower shape parameterisation, which might explain some of the differences observed in the leading jet mass for $Z' \to t\bar{t}$ events as described in Chapter 6.3.

However, looking at other cluster properties it becomes clear that further work beyond this thesis on the implementation of the cluster algorithm is necessary. In Figure 8.3b, the distance between two clusters $\Delta R = \sqrt{\Delta\eta^2 + \Delta\phi^2}$ is shown. The coordinates of the position of a cluster are defined as

$$\eta_{\text{clus}} = \frac{\sum_{i=1}^{N_{\text{cell}}} |E_{\text{cell},i}| \cdot \eta_{\text{cell},}}{\sum_{i=1}^{N_{\text{cell}}} |E_{\text{cell},i}|}$$
$$\phi_{\text{clus}} = \frac{\sum_{i=1}^{N_{\text{cell}}} |E_{\text{cell},i}| \cdot \phi_{\text{cell},i}}{\sum_{i=1}^{N_{\text{cell}}} |E_{\text{cell},i}|},$$

with N_{cell} denoting the number of associated cells for the cluster, E_{cell} the energy of a cell, and η_{cell} and ϕ_{cell} the coordinates of the cell, respectively [39]. It is not understood why there is a large peak close to zero since very close clusters should be merged.

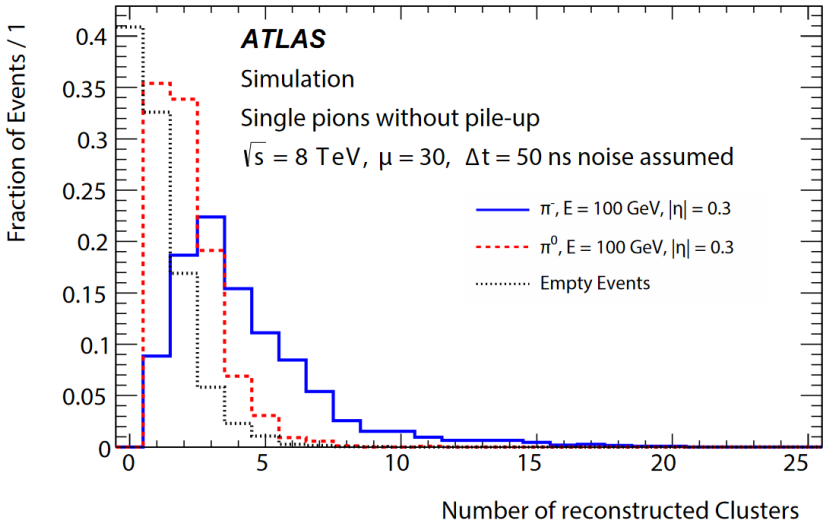

Figure 8.2.: Number of reconstructed clusters for simulated charged and neutral pions with 100 GeV at $|\eta| = 0.3$ [39].

There is also a large peak for very low energetic clusters as shown in Figure 8.3c. This should not be the case because the thresholds should prevent clusters without or with very little energy. A possible explanation for this might be that there are single isolated cells, which qualify as seed cells but do not have enough high energetic neighbours to form a cluster or to be merged with another cluster. This would also allow very short distances between two clusters if they each consist of only very few cells or even only one single cell. Taking into account this effect would naturally reduce the number of clusters, which yields to the opposite of the desired effect. Certainly, cluster splitting is not performed in this implementation and could increase the number of clusters. Furthermore, a peak at an energy slightly lower than the incoming particle's energy is expected but not observed. Additionally, the distribution for cluster depth

$$d_{\text{cluster}} = \frac{\sum_{i=0}^{N_{\text{cell}}} E_{\text{cell},i} \cdot w}{\sum_{i=0}^{N_{\text{cell}}} E_{\text{cell},i}},$$

with the distance to the beamline in x as the weight w for cells in the electromagnetic barrel and in z for the electromagnetic end-cap shown in Figure 8.3d does not look as expected, and indicates, again, that the clusters are not built correctly.

All in all, further development on the clustering algorithm in the standalone FastCaloSim is necessary. Nevertheless, it works well enough to expose before unknown differences between FastCaloSim and GEANT4 which might help investigating the remaining differences in higher level reconstructed physics observables such as the leading jet mass in high p_T

jets further.

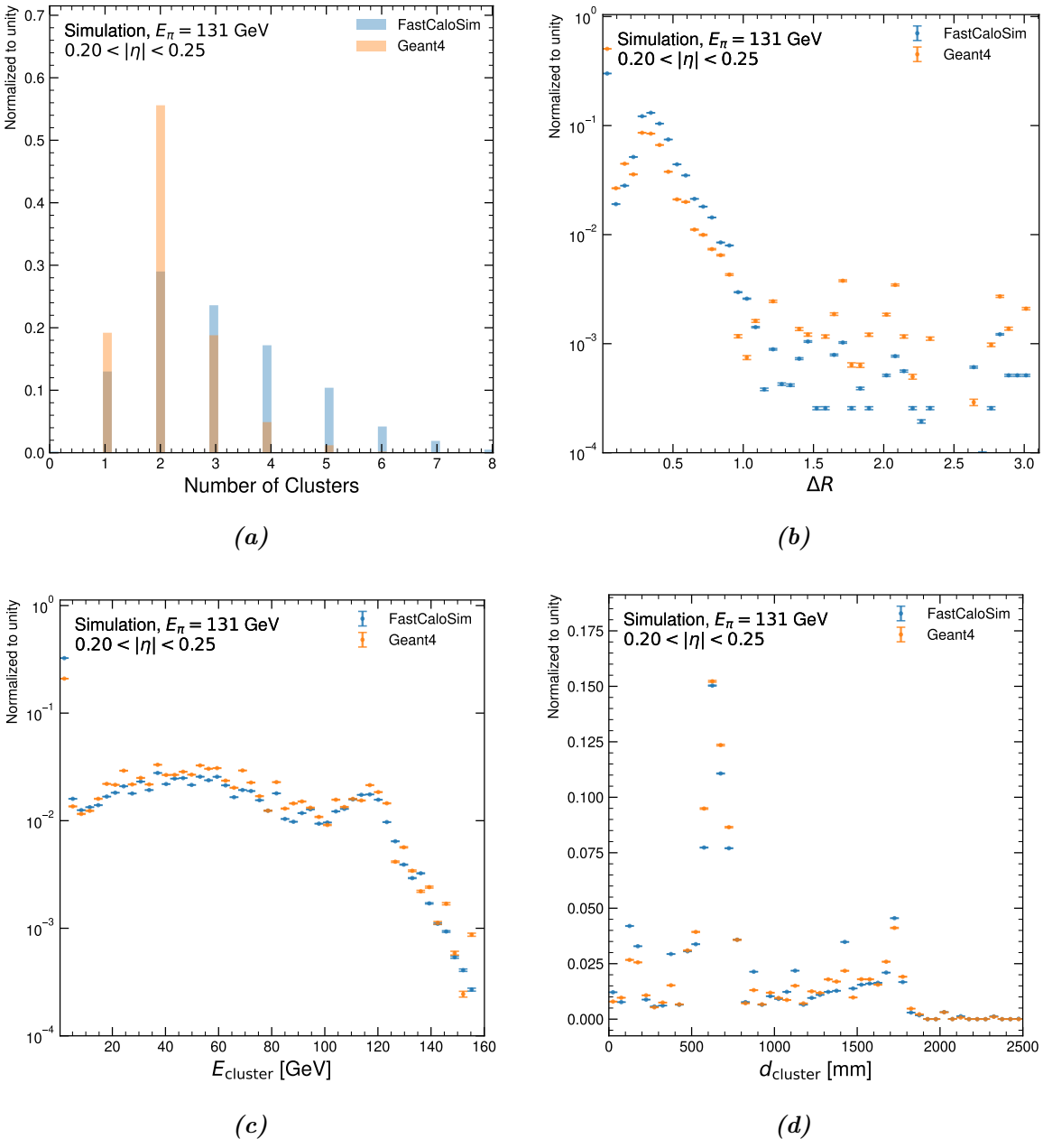

Figure 8.3.: Number of clusters (a) constructed with the simple topological clustering algorithm in the standalone FastCaloSim, the distance between to clusters ΔR (b), the energy of each cluster E_{cluster} (c) and the cluster depth d_{cluster} (d) for 131 GeV pions for the GEANT4 and the FastCaloSim.

9. Conclusions

In this Bachelor's thesis, variables to identify particles were investigated in the ATLAS Fast Calorimeter Simulation. For this purpose, the variables have been implemented in the standalone FastCaloSimV2 algorithm. The FastCaloSimV2 algorithm is part of the AtlFast3 toolkit. Comparing to its predecessor AtlFastII, it has improved accuracy in reproducing the full simulation with GEANT4. Both are designed to speed up the simulation of the detector response because otherwise the required CPU resources would outgrow the available capacity due to the expected increased integrated luminosity in Run 3 and beyond.

Comparing the means of the distributions for the implementation in the standalone FastCaloSim algorithm and in Athena, it is clear that the implementation has been successful, generally speaking. Comparing the distributions gained from the implementation in the standalone FastCaloSim algorithm for FastCaloSim and GEANT4, the excellent agreement is striking. However, because GEANT4 itself fails to reproduce some of the shower shape variables as observed in data, the next step towards a more accurate simulation of the shower shape variables is to tune the distributions to data.

Comparing the distributions for photons and electrons, one can conclude that electron and photon induced showers have a very similar behaviour, which is expected since both are electromagnetic showers. From the small shift in the distributions concerning the shower width, f_{side}, $w_{\eta 1}$, w_{stot}, R_η and R_ϕ, one can observe that photon induced showers are slightly more narrow.

Comparing the distribution for electrons, photons and pions, the significant differences for hadronic and electromagnetic showers are striking. This demonstrates, again, that the implementation of the variables is satisfactory as the main purpose of these variables is to discriminate between signal, meaning electrons and photons, and background, which mainly includes hadronic jets.

In addition to the shower shape variables, a simple clustering algorithm has been implemented successfully in the standalone FastCaloSim algorithm. This contributes to a better understanding of the remaining differences between AtlFast3 and GEANT4 in high level variables like the leading jet mass in $Z' \to t\bar{t}$ events. The differences in the number

of reconstructed clusters for FastCaloSim and GEANT4 suggests that clustering might be one of the reasons for these differences.

All in all, even though small details in the implementation of some of the shower shape variables and the clustering algorithm in the standalone FastCaloSim algorithm can still be improved, like the cell list used for layer 1 variables and the cluster properties ΔR, E_{cluster} and d_{cluster}, the results of this thesis can be used for investigations into the shower shape variables as well as for prospective work on the FastCaloSim algorithm.

With improving accuracy in the simulation, an increasing part of the physics analyses in ATLAS will be able to use AtlFast3, the next generation of fast simulation in ATLAS. This is crucial since using the full simulation for most analyses will no longer be an option at some point in Run 3 and beyond on grounds of CPU resources.

A. Additional distributions of the shower shape variables

A.1. FastCaloSim and Geant4 in comparison

A.1.1. Electrons

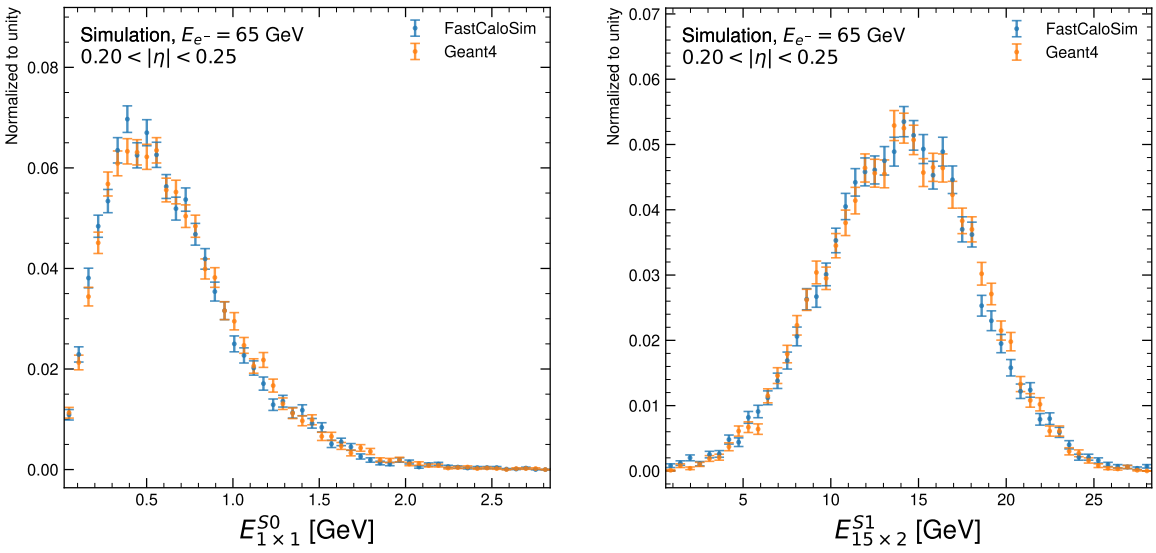

(a) *(b)*

Figure A.1.: Distributions of energy windows in $\eta \times \phi$ around the cell with the most deposited energy in the presampler (S0) and in the first layer of the electromagnetic barrel (S1) for 65 GeV electrons in the region $0.20 < |\eta| < 0.25$.

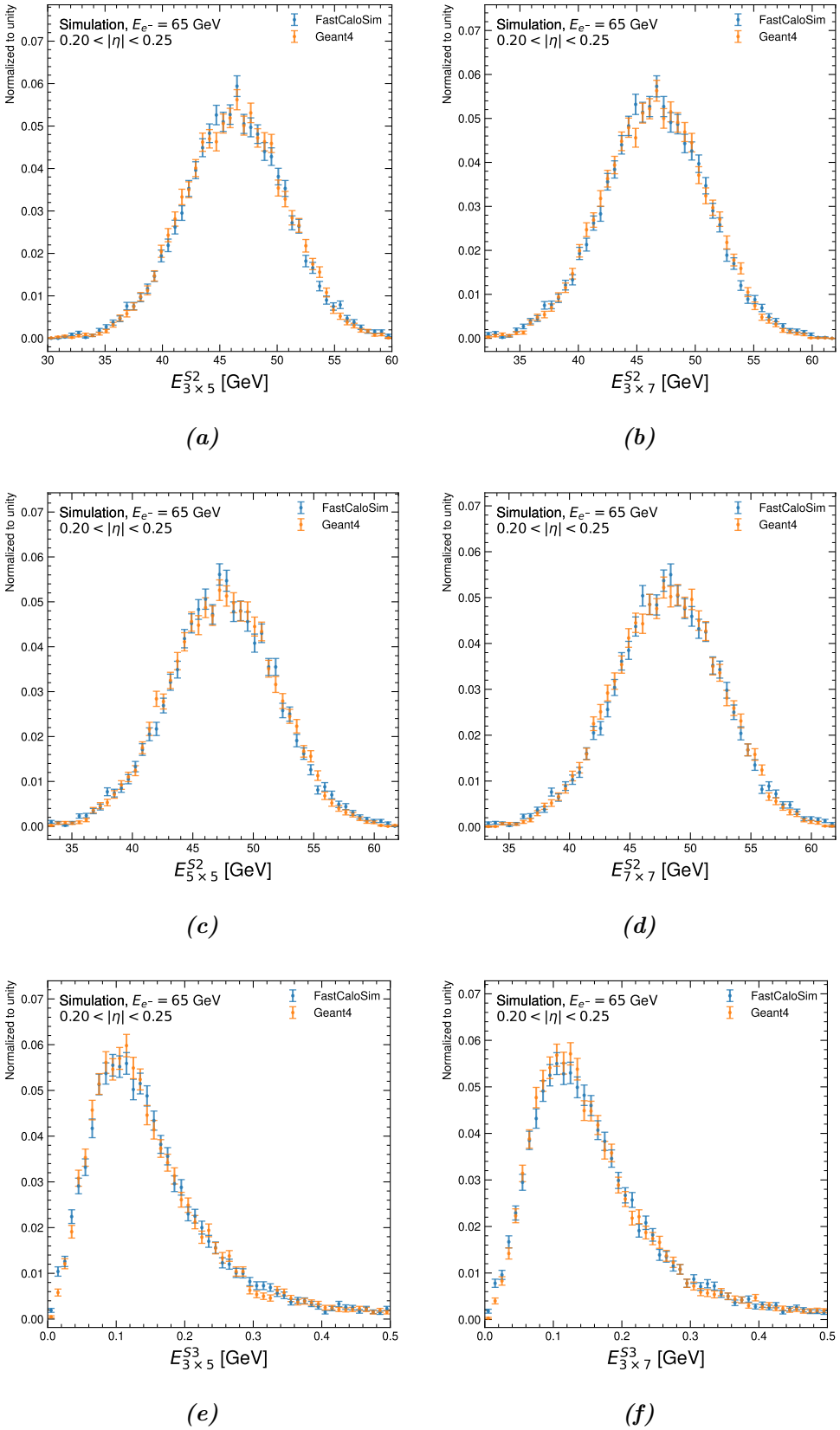

Figure A.2.: Distributions of energy windows in $\eta \times \phi$ around the cell with the most deposited energy in the second and third layer of the electromagnetic barrel (S2 and S3) for 65 GeV electrons in the region $0.20 < |\eta| < 0.25$.

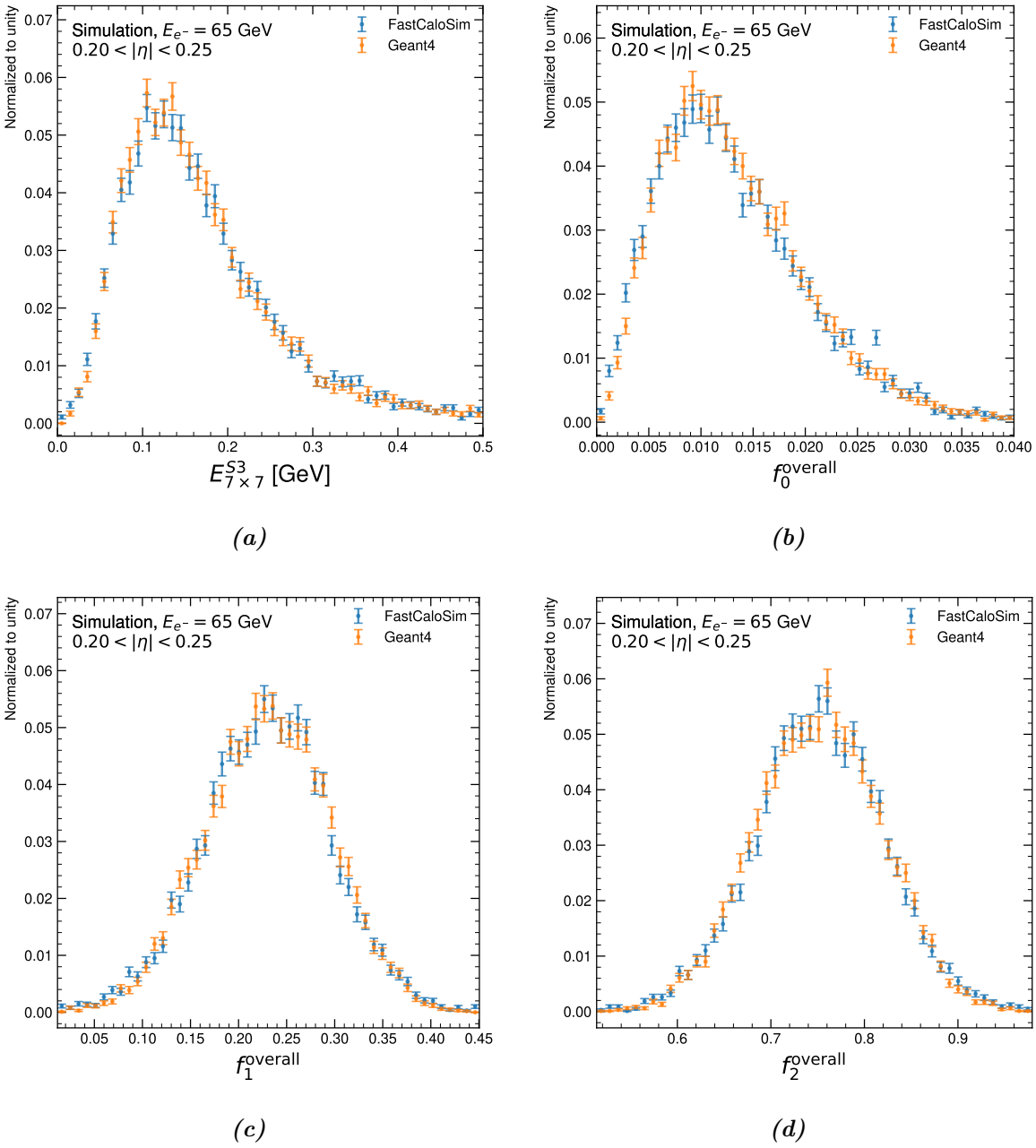

Figure A.3.: Distribution of an energy window in $\eta \times \phi$ around the cell with the most deposited energy in the the third layer of the electromagnetic barrel (S3) (a) and distributions of fractions of energy in the first three layers over the whole calorimeter (b)-(d) for 65 GeV electrons in the region $0.20 < |\eta| < 0.25$.

A.1.2. Photons

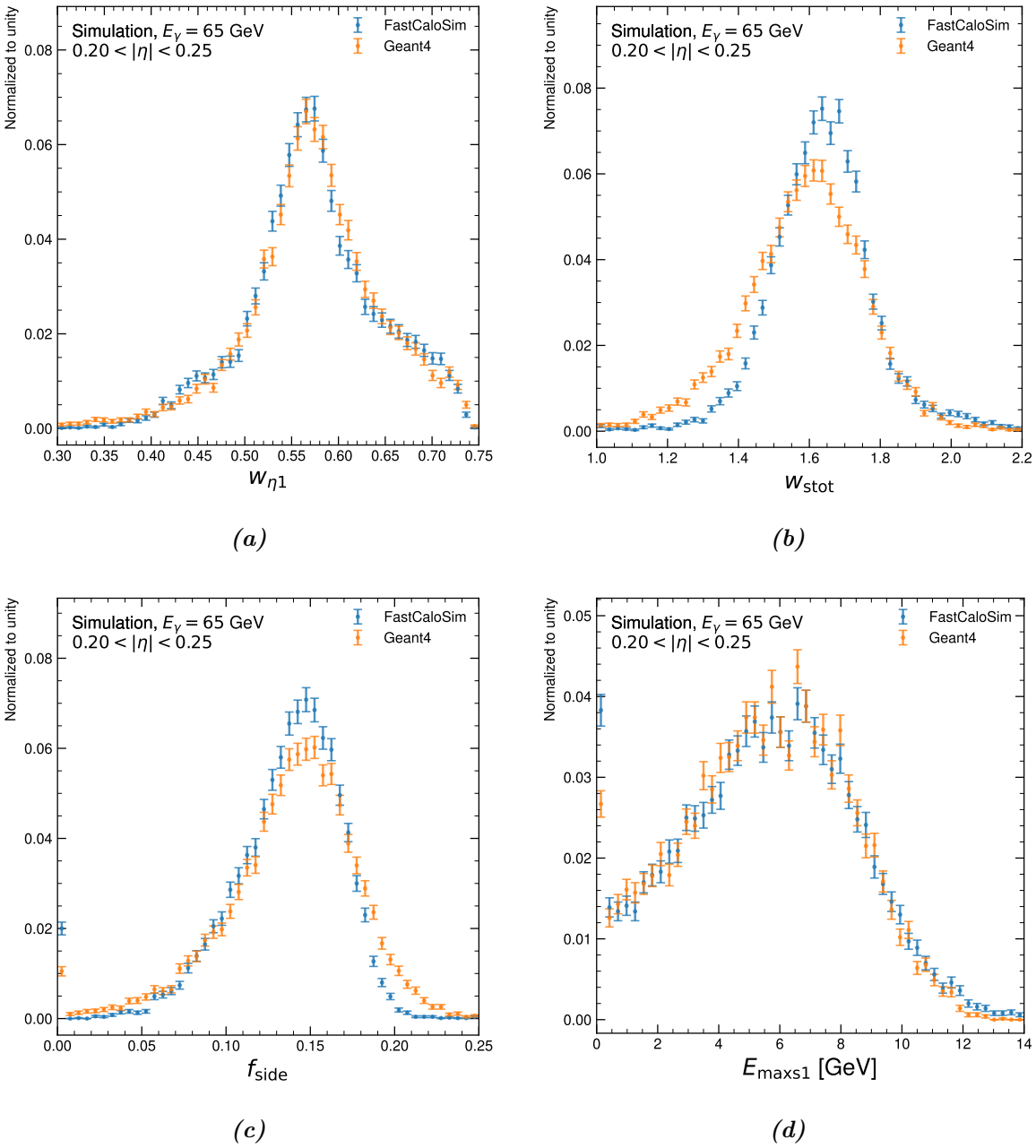

Figure A.4.: Distributions of the shower shape variables $w_{\eta 1}$, w_{stot}, f_{side} and E_{maxs1} for FastCaloSim and GEANT4 in comparison for 65 GeV photons in the region $0.20 < |\eta| < 0.25$ calculated with the implementation in the standalone FastCaloSim algorithm.

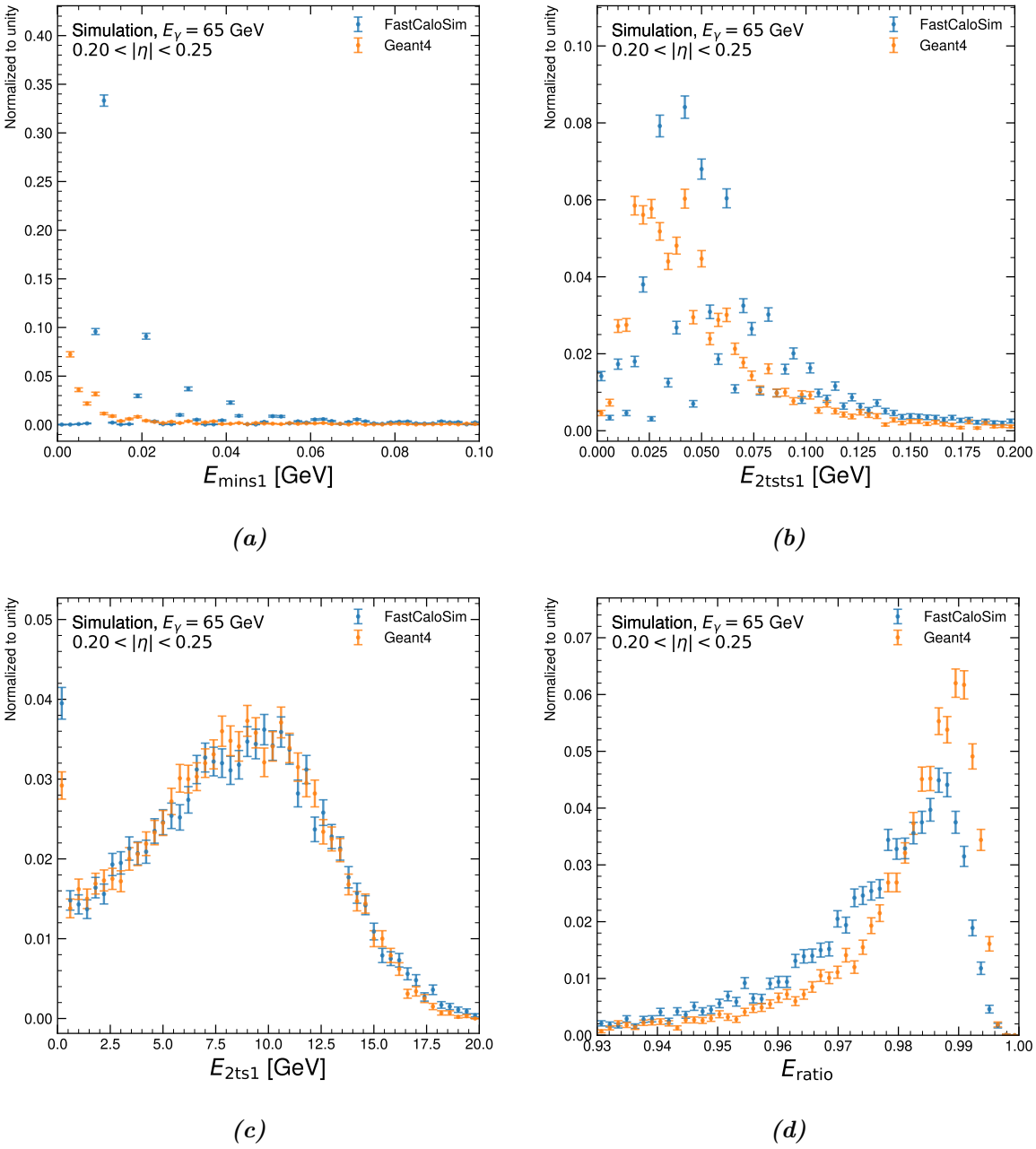

Figure A.5.: Distributions of the shower shape variables E_{mins1}, E_{e2tsts1}, E_{e2ts1} and E_{ratio}, for FastCaloSim and GEANT4 in comparison for 65 GeV photons in the region $0.20 < |\eta| < 0.25$ calculated with the implementation in the standalone FastCaloSim algorithm.

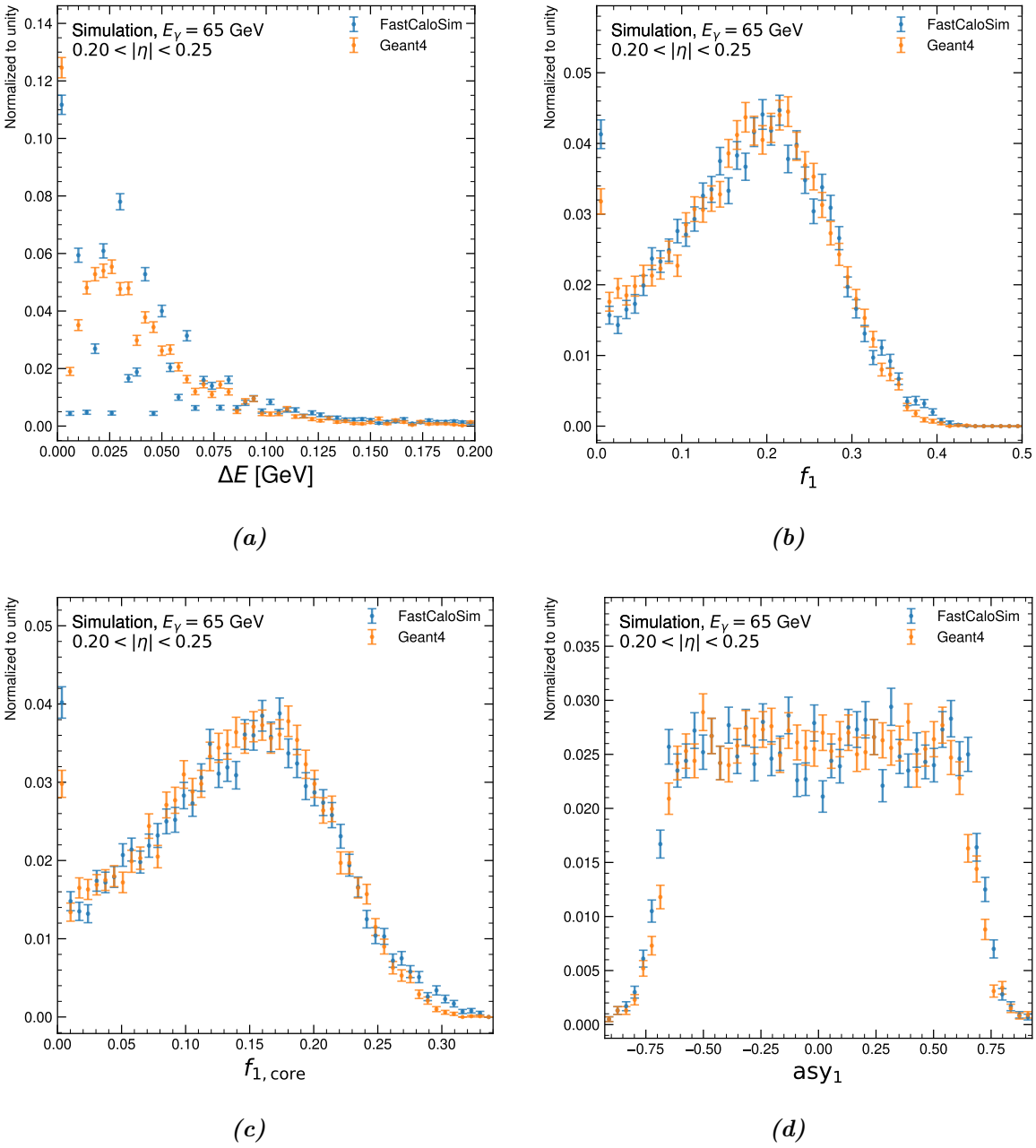

Figure A.6.: Distributions of the shower shape variables ΔE, f_1, $f_{1,\mathrm{core}}$ and asy_1 for FastCaloSim and GEANT4 in comparison for 65 GeV photons in the region $0.20 < |\eta| < 0.25$ calculated with the implementation in the standalone FastCaloSim algorithm.

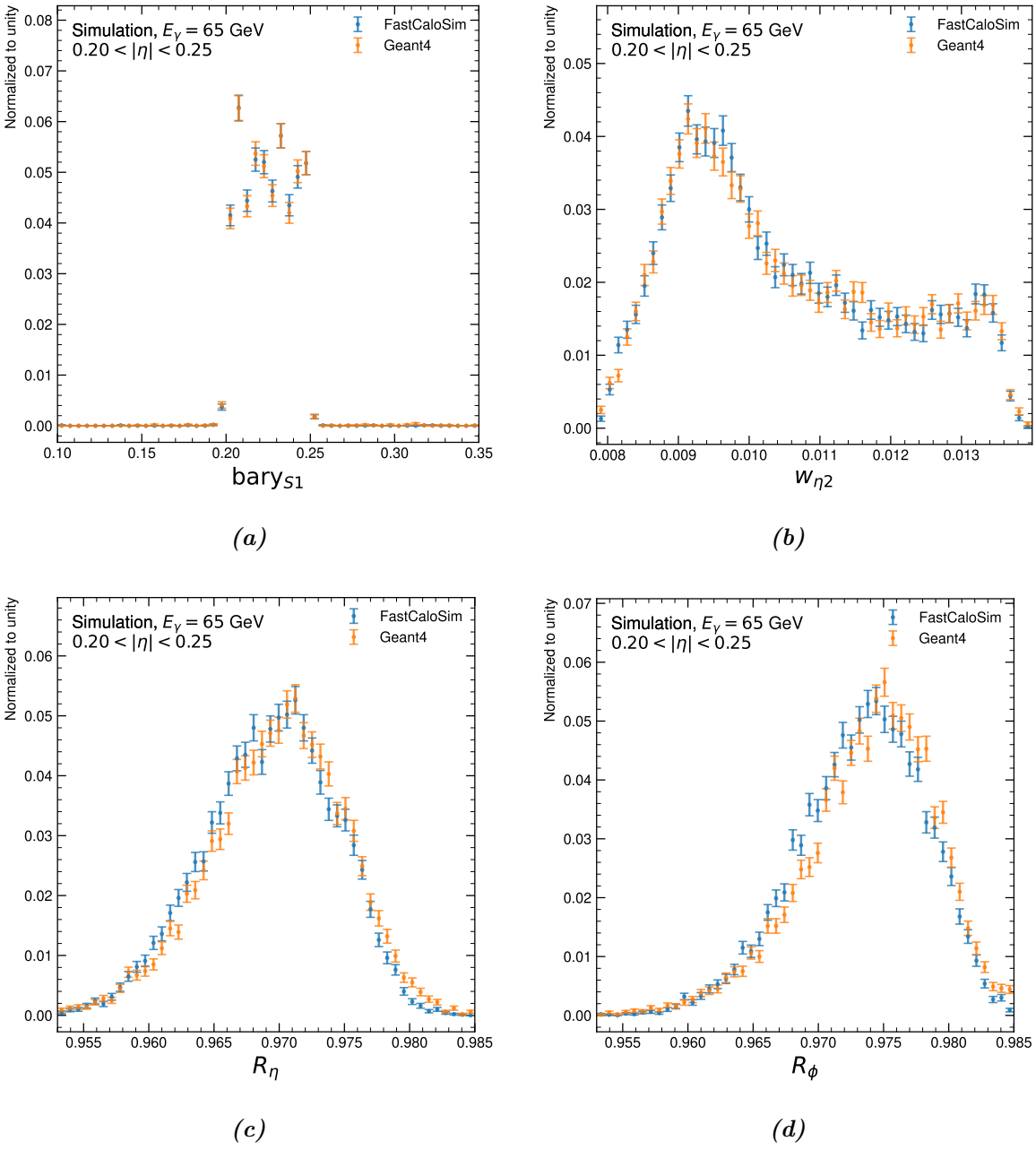

Figure A.7.: Distributions of the shower shape variables bary_{S1}, $w_{\eta 2}$, R_η and R_ϕ for FastCaloSim and GEANT4 in comparison for 65 GeV photons in the region $0.20 < |\eta| < 0.25$ calculated with the implementation in the standalone FastCaloSim algorithm.

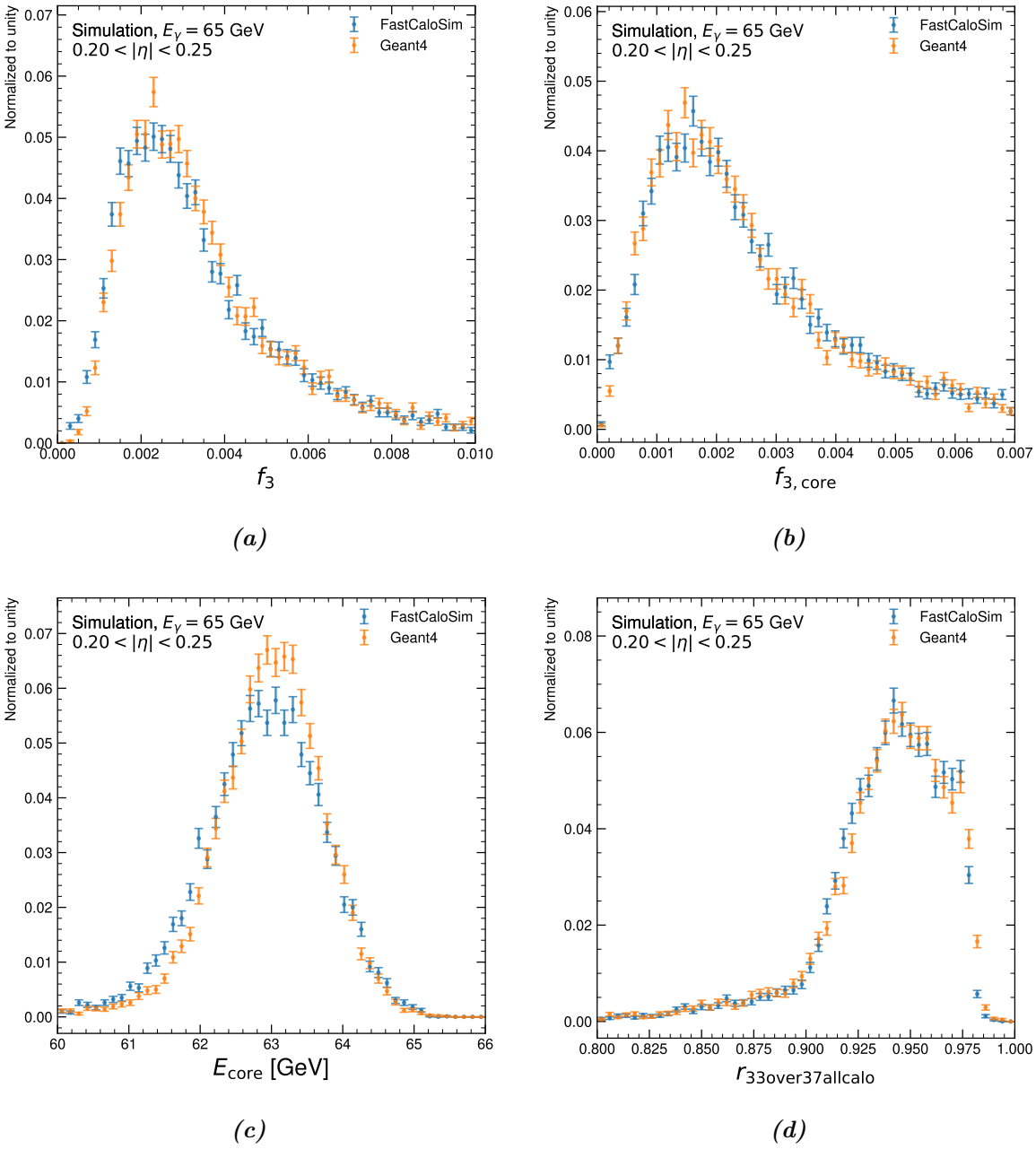

Figure A.8.: Distributions of the shower shape variables f_3, $f_{3,\mathrm{core}}$, E_{core} and $r_{33\mathrm{over}37\mathrm{allcalo}}$ for FastCaloSim and GEANT4 in comparison for 65 GeV photons in the region $0.20 < |\eta| < 0.25$ calculated with the implementation in the standalone FastCaloSim algorithm.

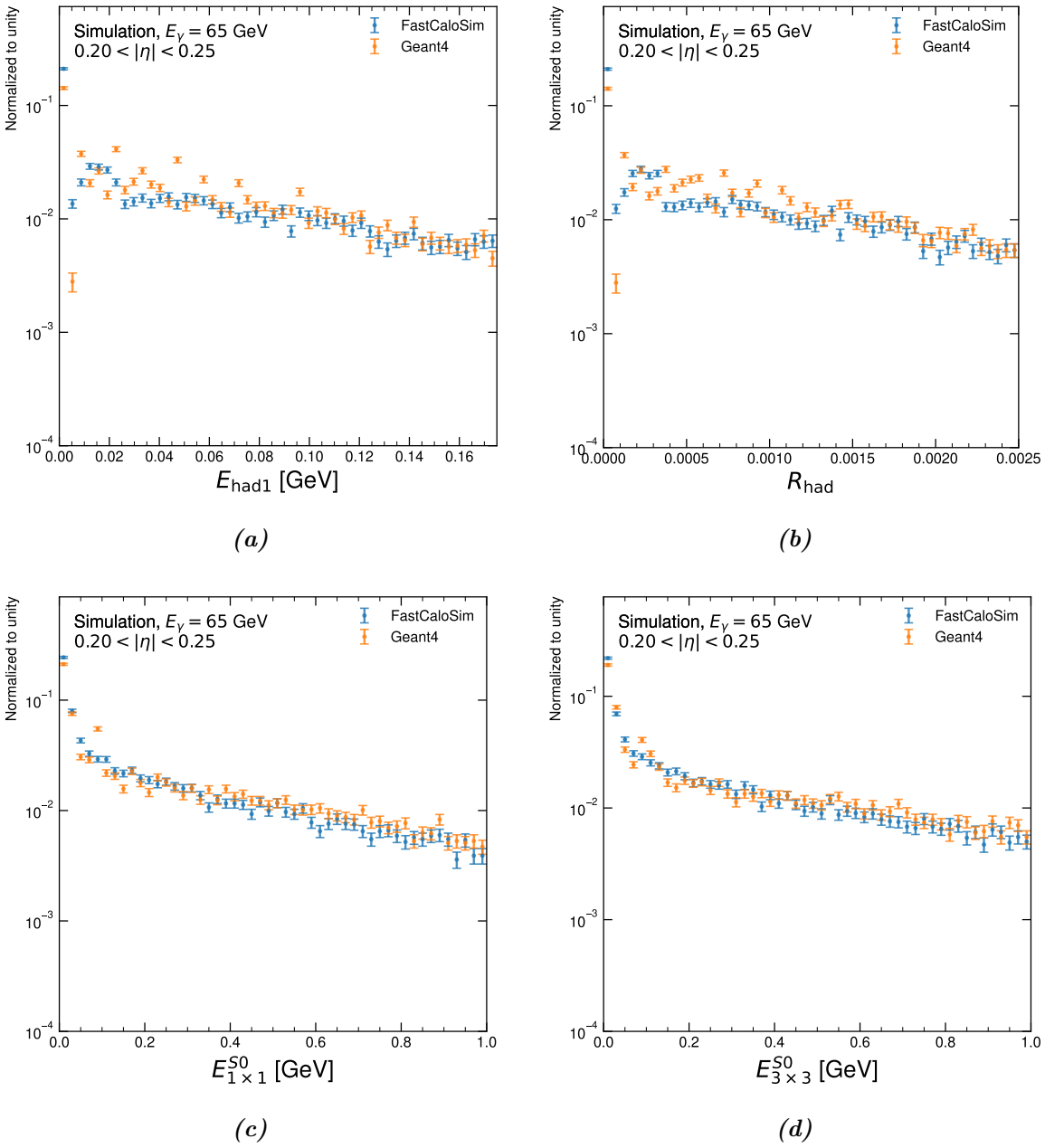

Figure A.9.: Distributions of the shower shape variables E_{had1} (a), R_{had} (b) and energy windows in $\eta \times \phi$ around the cell with the most deposited energy in the presampler (S0) (c), (d) for FastCaloSim and GEANT4 in comparison for 65 GeV photons in the region $0.20 < |\eta| < 0.25$ calculated with the implementation in the standalone FastCaloSim algorithm.

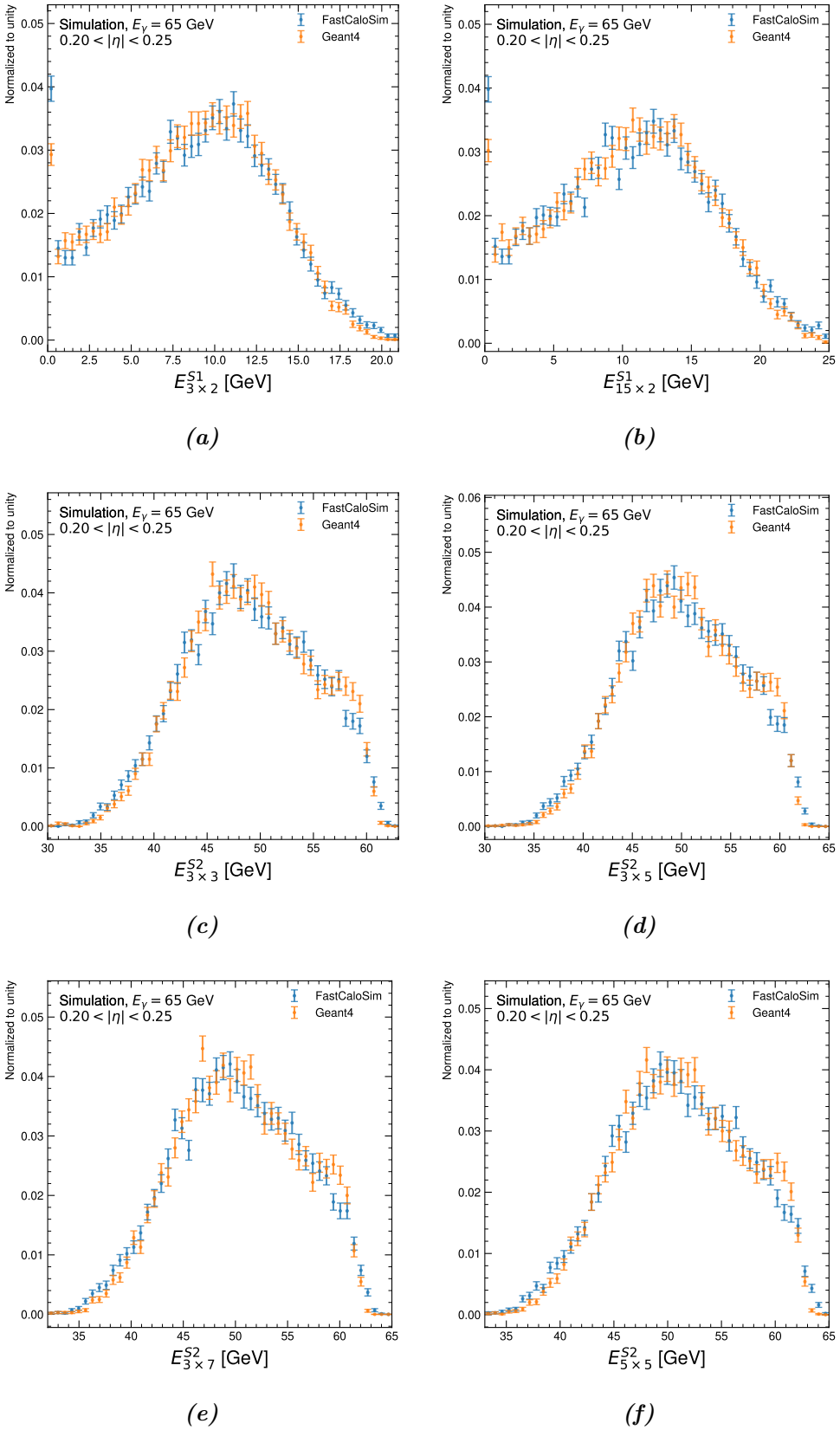

Figure A.10.: Distributions for energy windows in $\eta \times \phi$ around the cell with the most deposited energy in the first two layers of the electromagnetic barrel (S1 and S2) for 65 GeV photons in the region $0.20 < |\eta| < 0.25$.

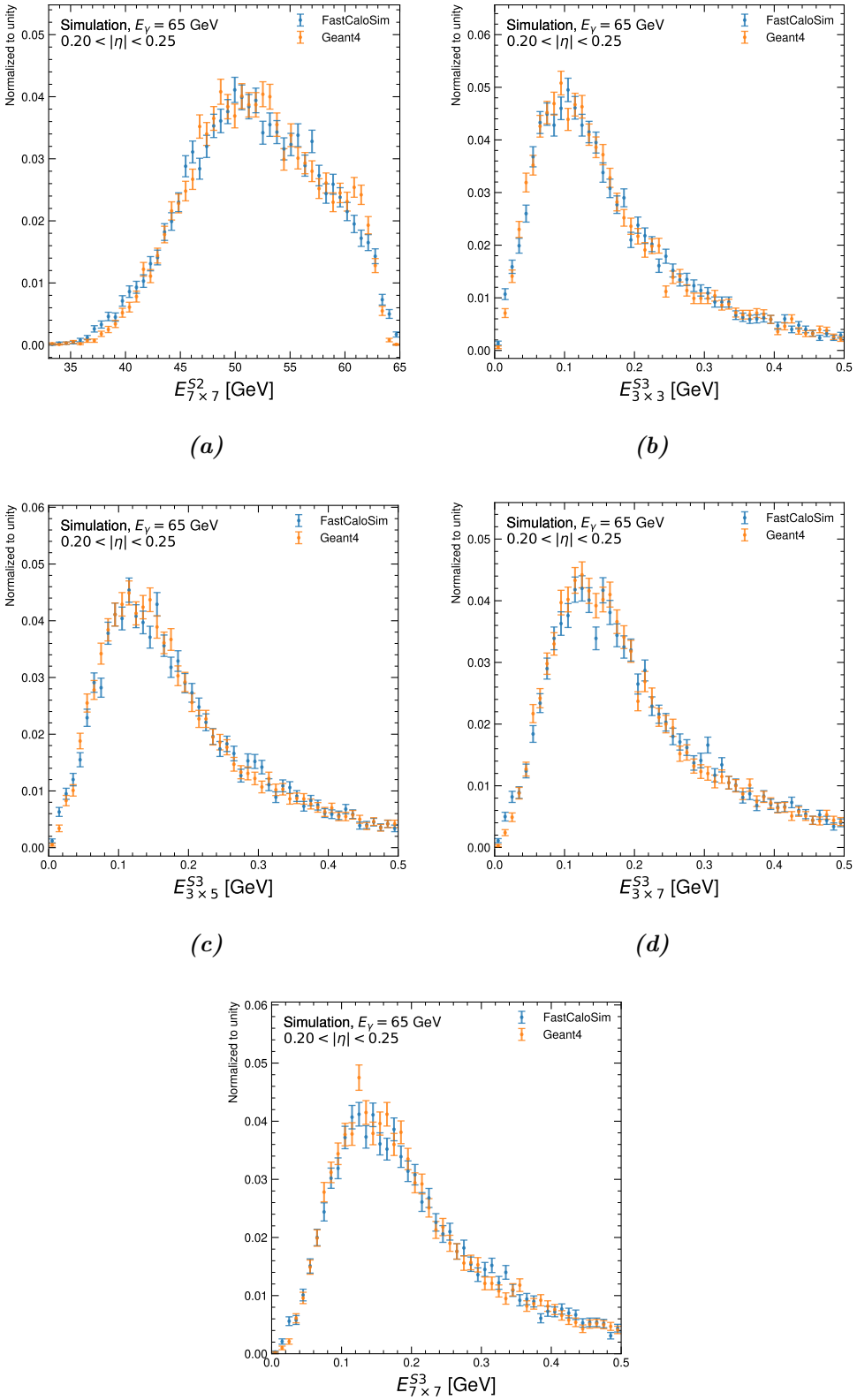

(a) *(b)* *(c)* *(d)* *(e)*

Figure A.11.: Distributions for energy windows in $\eta \times \phi$ around the cell with the most deposited energy in the second and third layer of the electromagnetic barrel (S2 and S3) for 65 GeV photons in the region $0.20 < |\eta| < 0.25$.

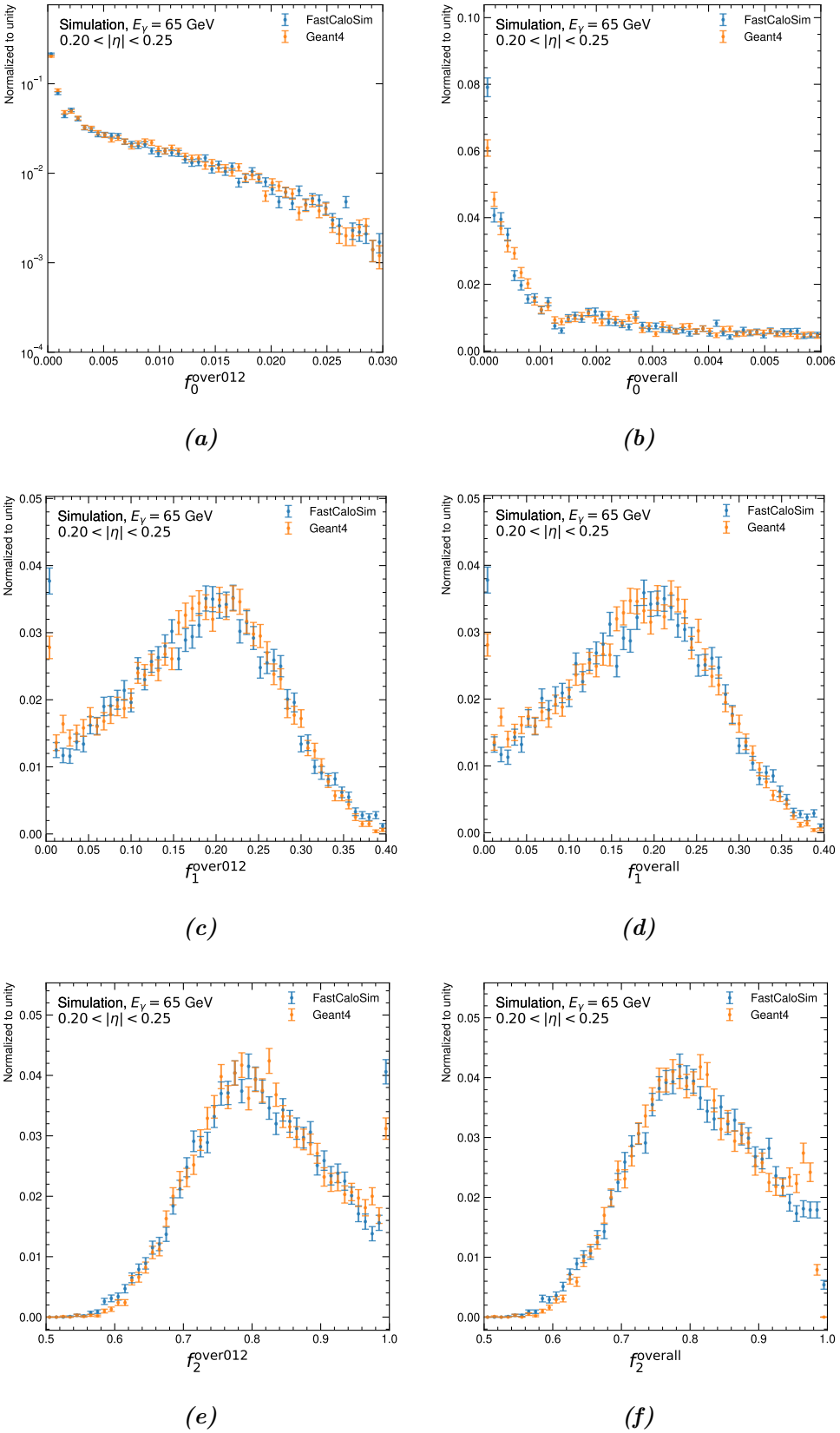

Figure A.12.: Distributions of fractions of energy in the first three layers over the sum of these (a), (c) and (e) and over the whole calorimeter (b), (d) and (f) for 65 GeV photons in the region $0.20 < |\eta| < 0.25$.

A.1.3. Pions

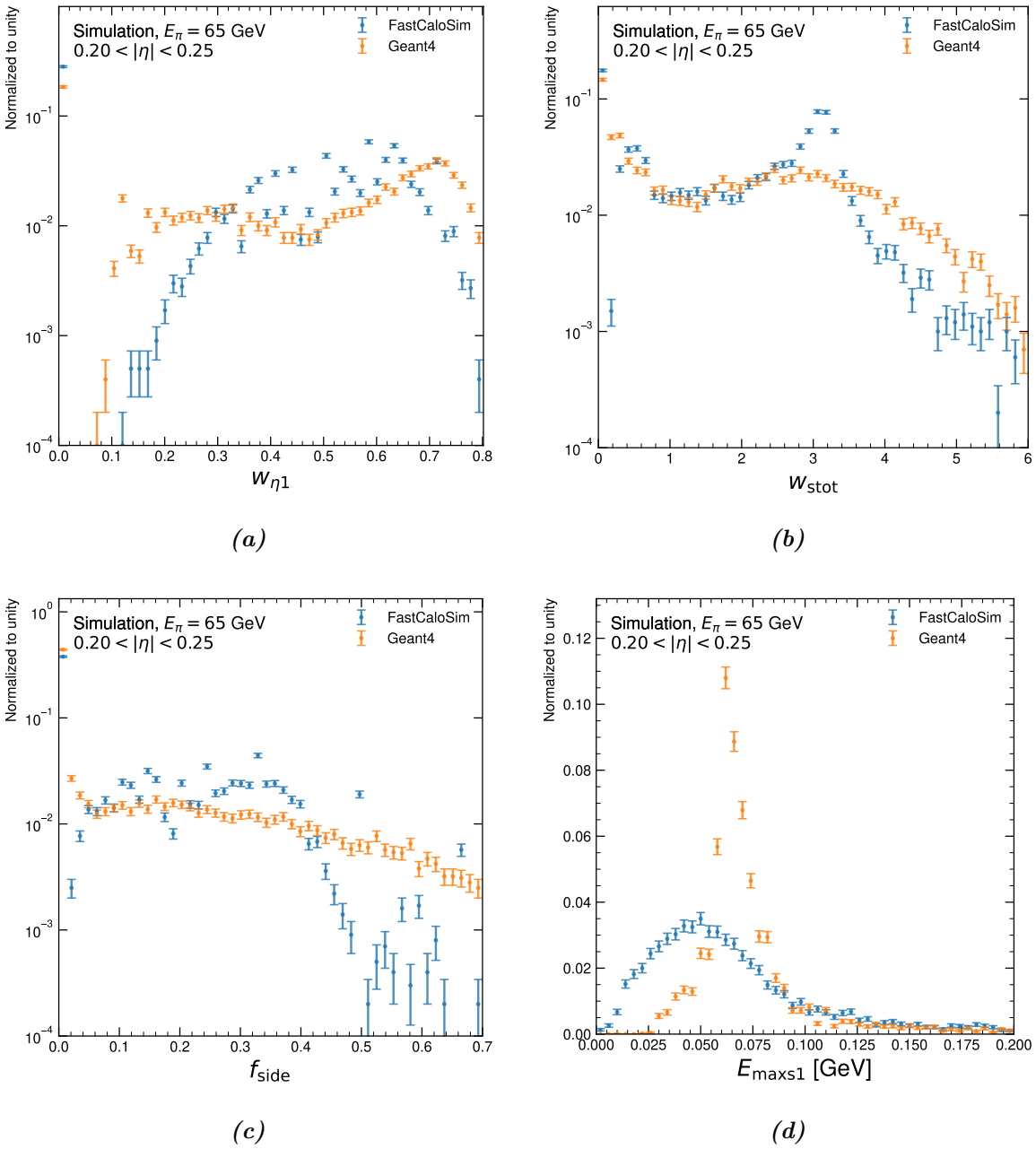

Figure A.13.: Distributions of the shower shape variables $w_{\eta 1}$, w_{stot}, f_{side} and E_{maxs1} for FastCaloSim and GEANT4 in comparison for 65 GeV pions in the region $0.20 < |\eta| < 0.25$ calculated with the implementation in the standalone FastCaloSim algorithm.

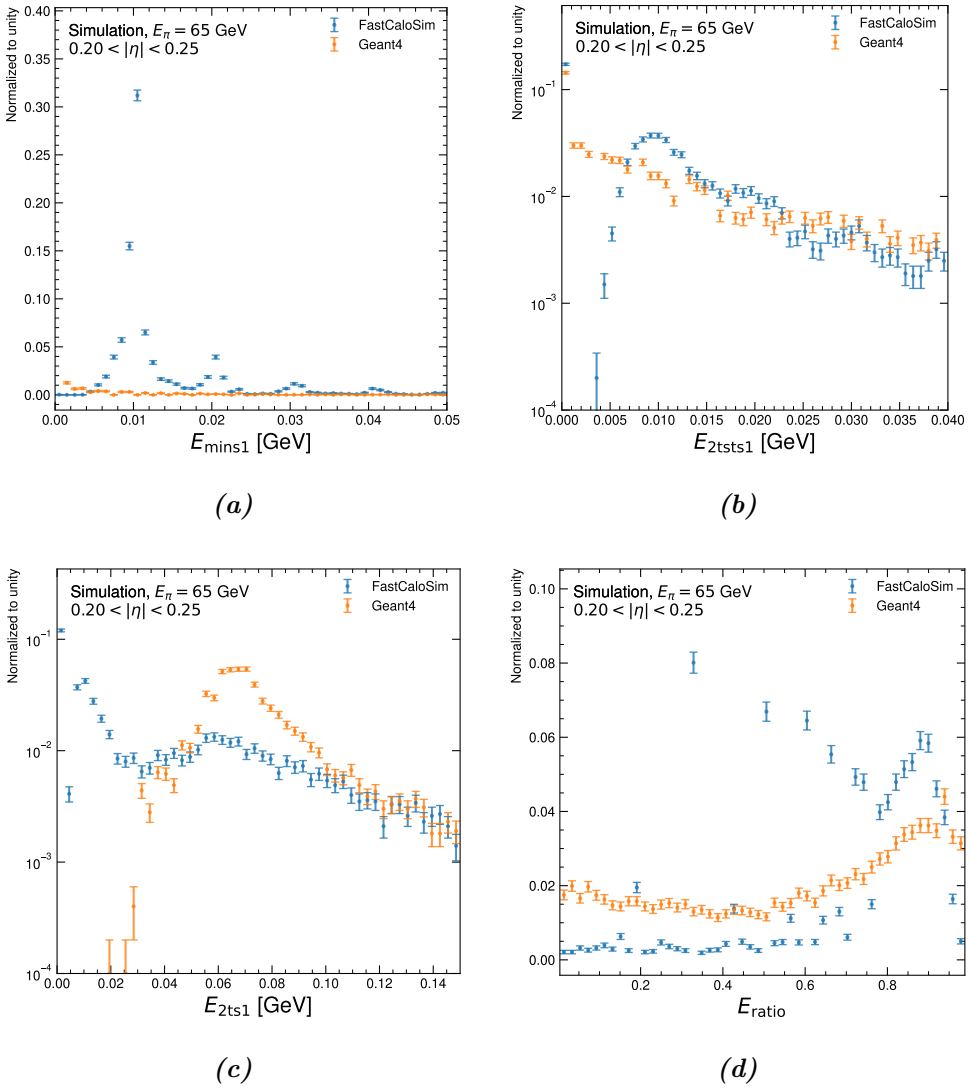

Figure A.14.: Distributions of the shower shape variables E_{mins1}, E_{e2tsts1}, E_{e2ts1} and E_{ratio} for FastCaloSim and GEANT4 in comparison for 65 GeV pions in the region $0.20 < |\eta| < 0.25$ calculated with the implementation in the standalone FastCaloSim algorithm.

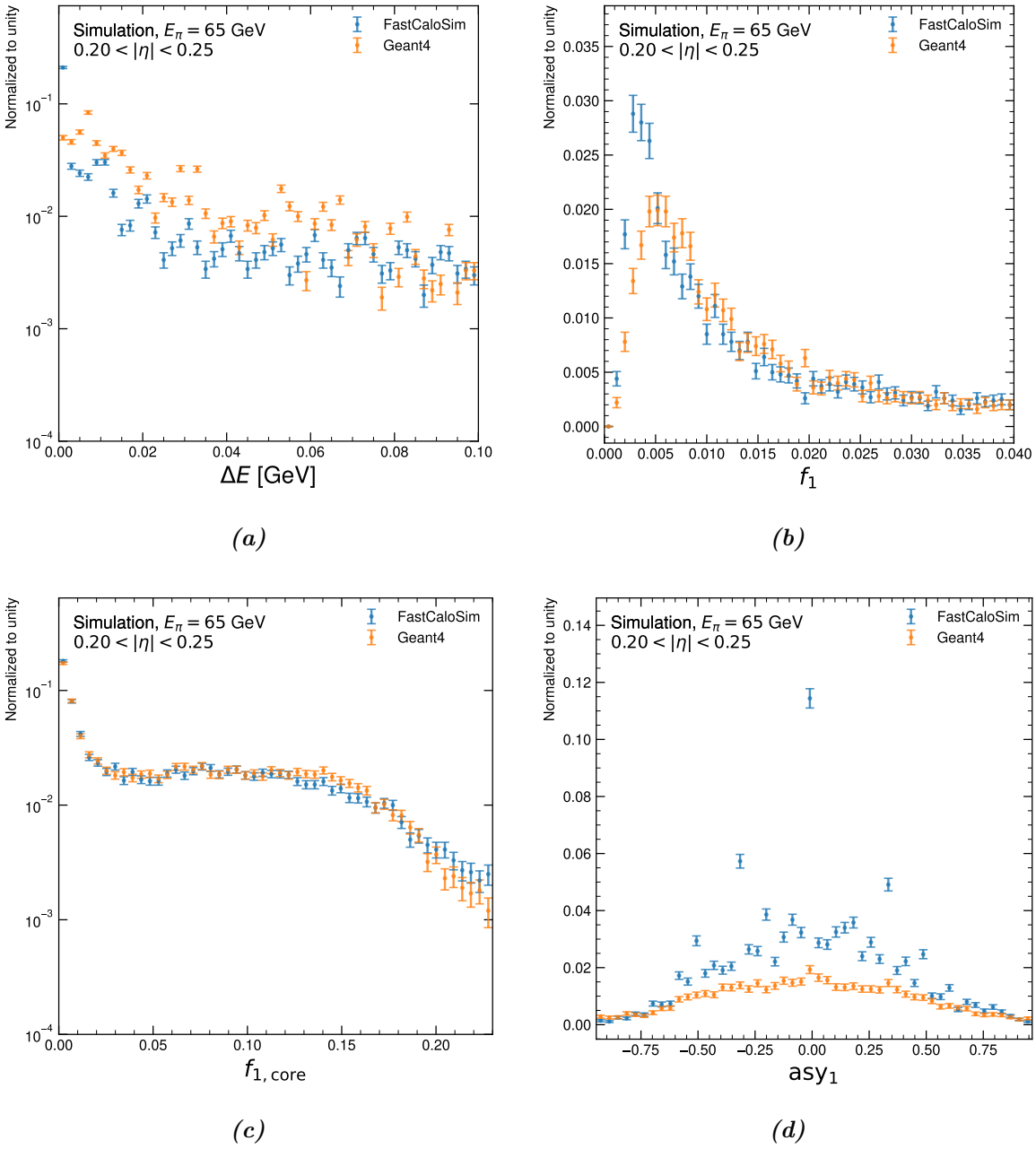

Figure A.15.: Distributions of the shower shape variables ΔE, f_1, $f_{1,\text{core}}$ and asy$_1$ for FastCaloSim and GEANT4 in comparison for 65 GeV pions in the region $0.20 < |\eta| < 0.25$ calculated with the implementation in the standalone FastCaloSim algorithm.

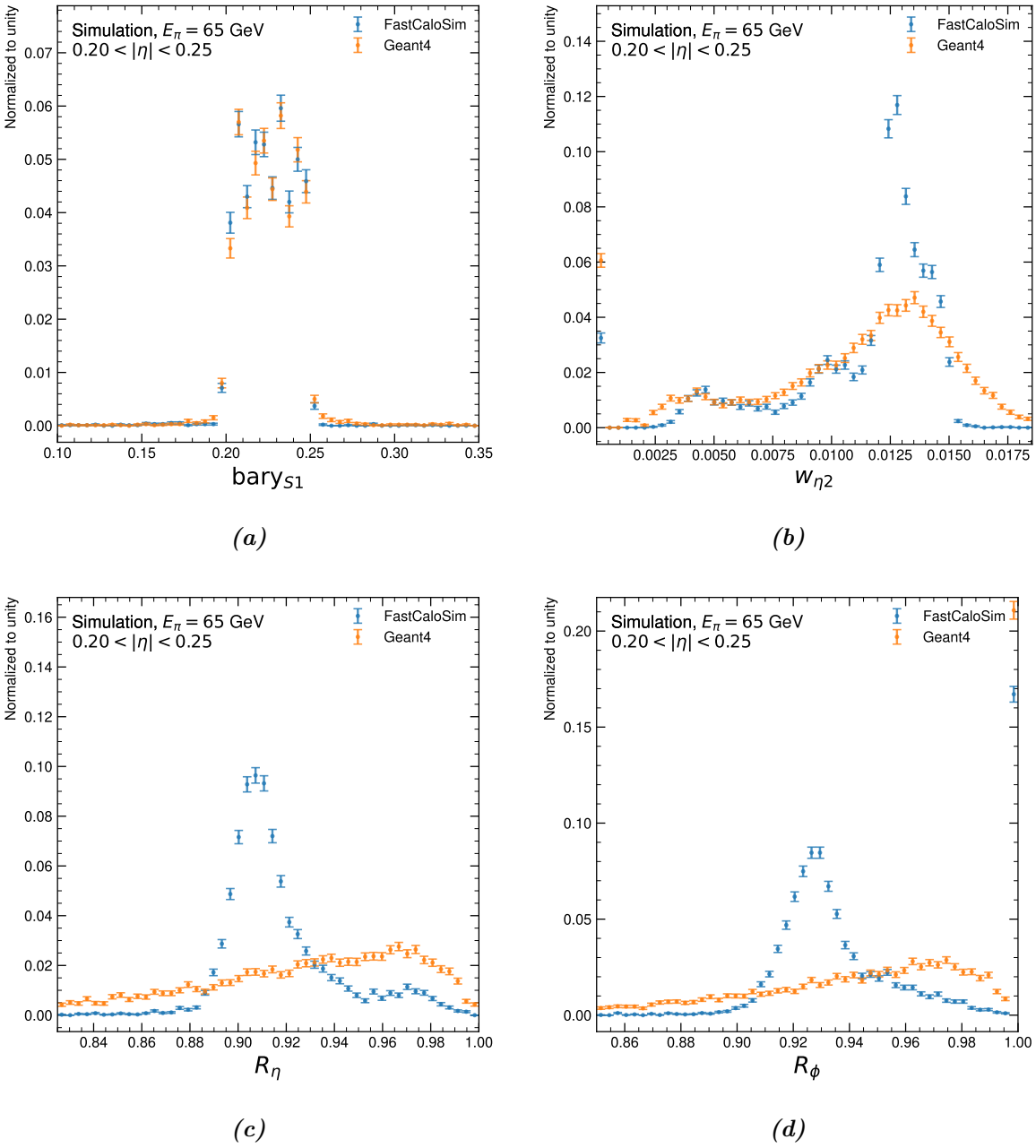

Figure A.16.: Distributions of the shower shape variables bary_{S1}, $w_{\eta 2}$, R_η and R_ϕ for FastCaloSim and GEANT4 in comparison for 65 GeV pions in the region $0.20 < |\eta| < 0.25$ calculated with the implementation in the standalone FastCaloSim algorithm.

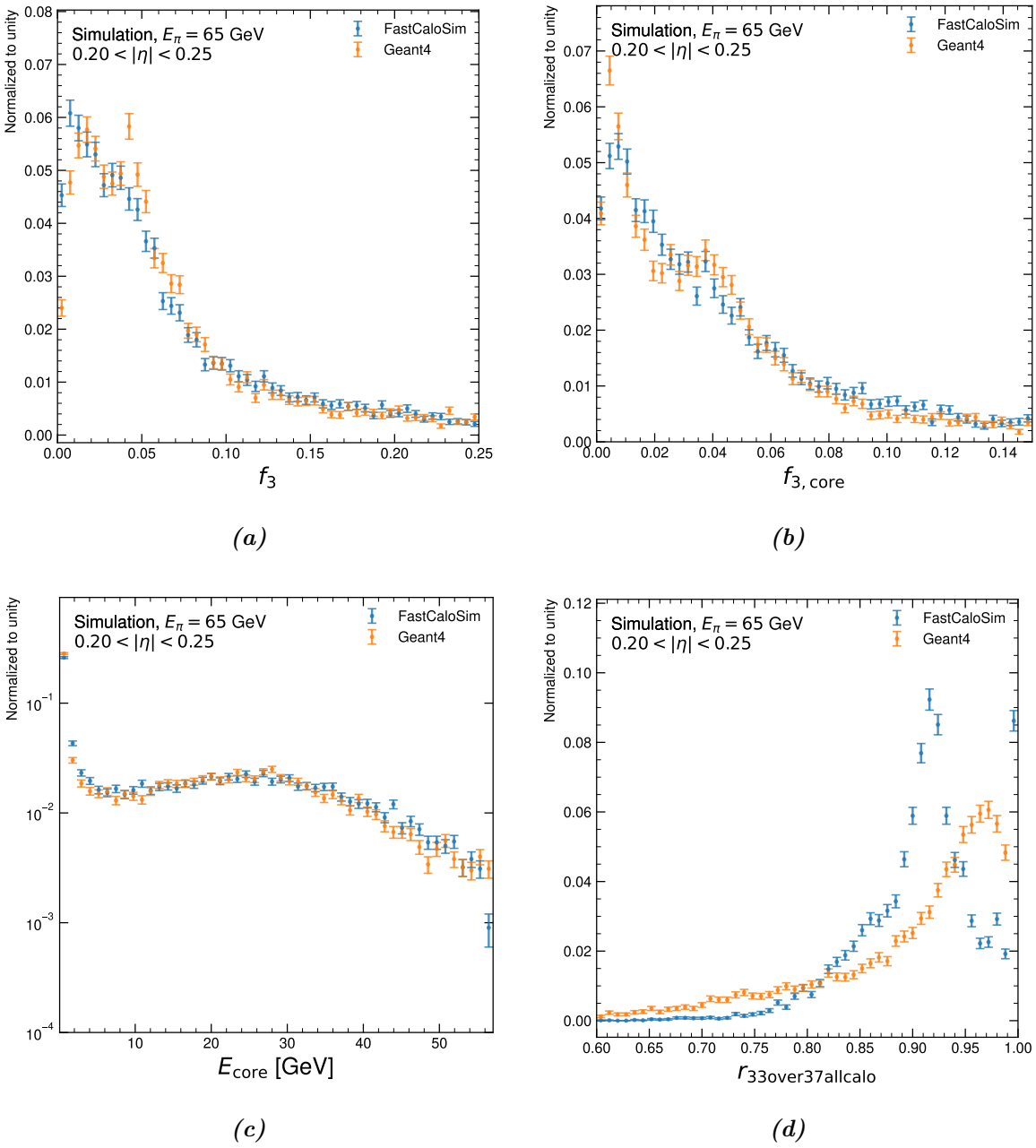

Figure A.17.: Distributions of the shower shape variables f_3, $f_{3,\mathrm{core}}$, E_{core} and $r_{33\mathrm{over}37\mathrm{allcalo}}$ for FastCaloSim and GEANT4 in comparison for 65 GeV pions in the region $0.20 < |\eta| < 0.25$ calculated with the implementation in the standalone FastCaloSim algorithm.

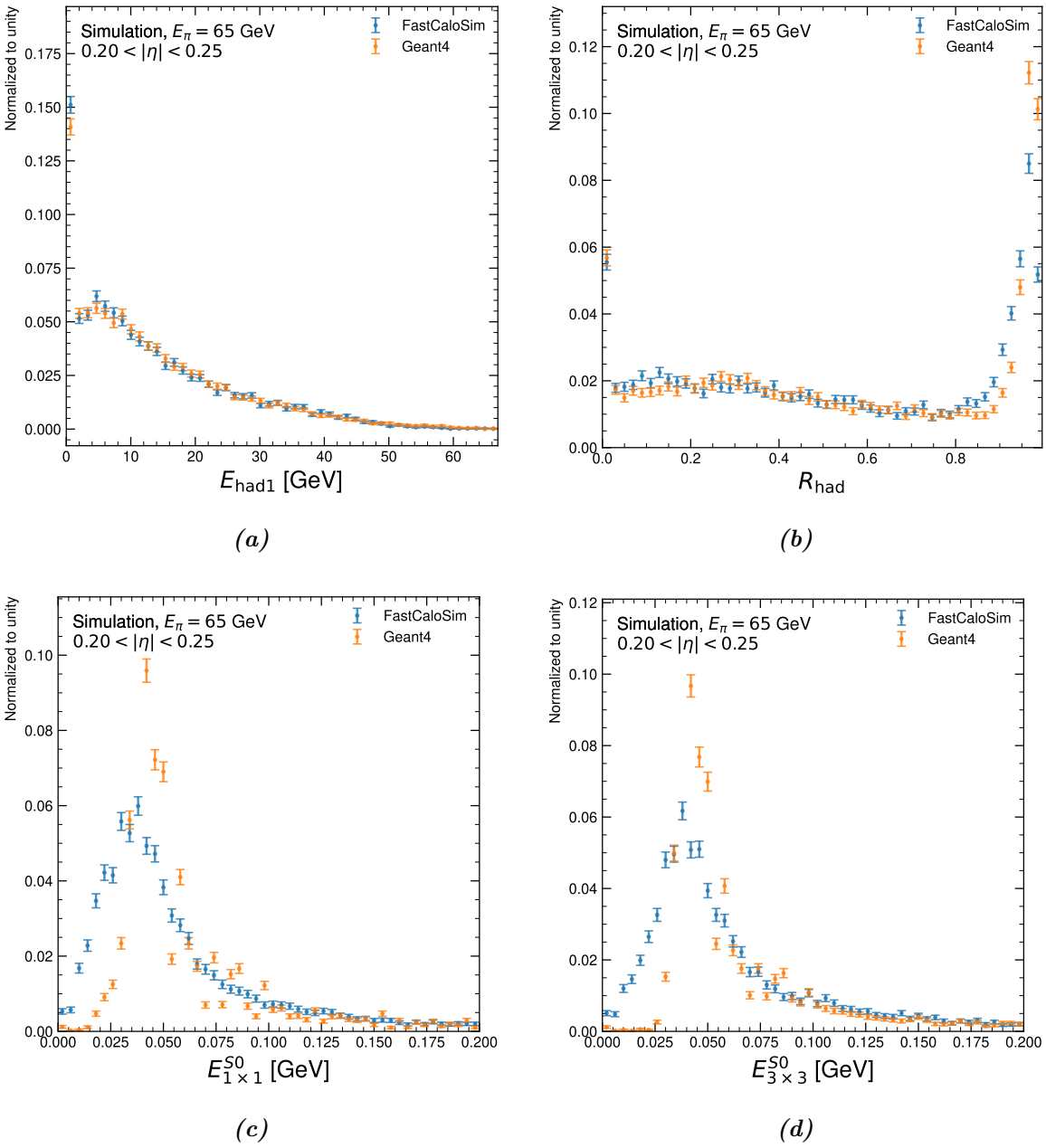

Figure A.18.: Distributions of the shower shape variables E_{had1} (a) and R_{had} (b) and energy windows in $\eta\times\phi$ around the cell with the most deposited energy in the presampler (S0) (c), (d) for FastCaloSim and GEANT4 in comparison for 65 GeV pions in the region $0.20 < |\eta| < 0.25$ calculated with the implementation in the standalone FastCaloSim algorithm.

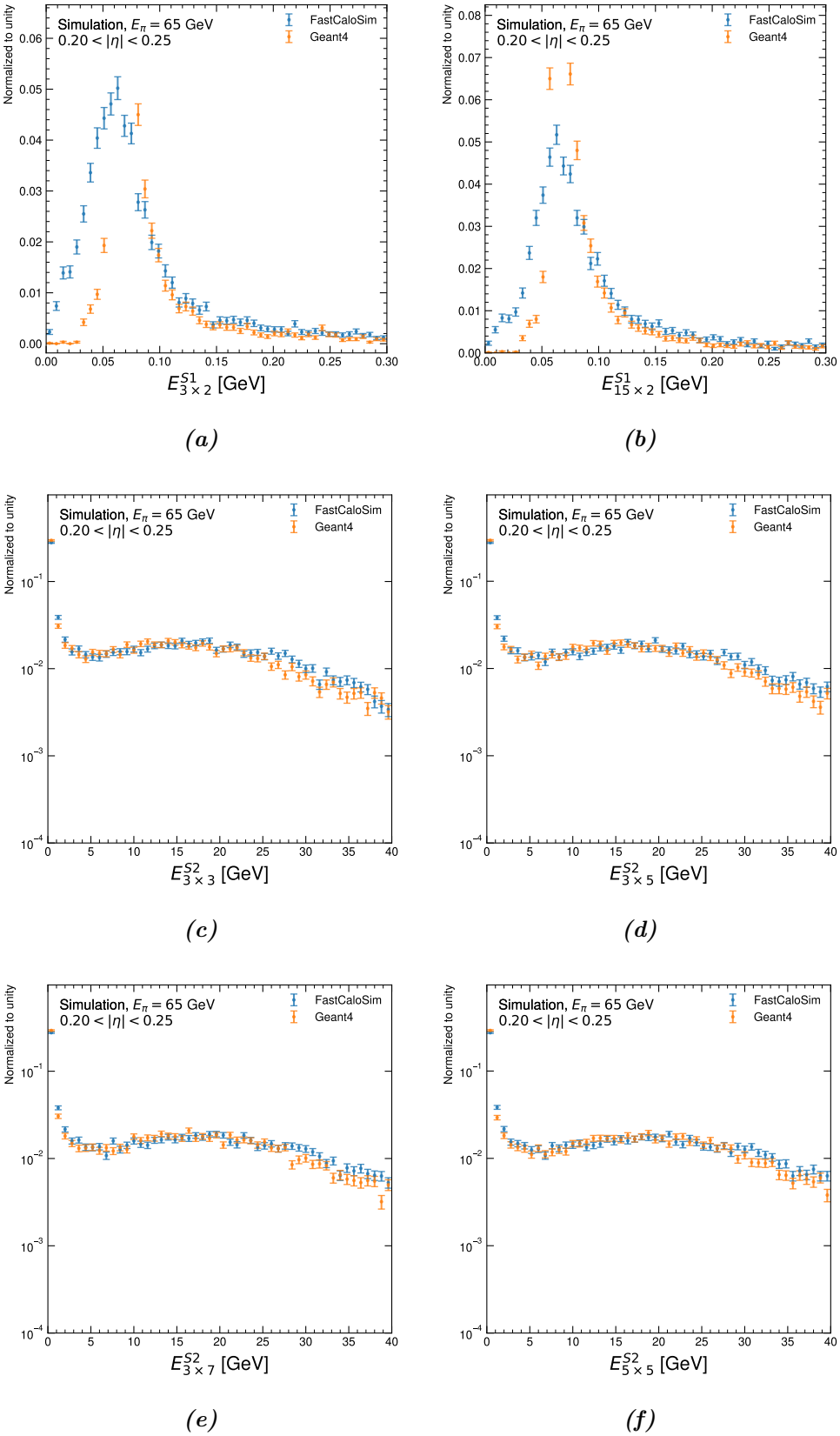

(a) *(b)* *(c)* *(d)* *(e)* *(f)*

Figure A.19.: Distributions for energy windows in $\eta \times \phi$ around the cell with the most deposited energy in the first two layers of the electromagnetic barrel (S1 and S2) for 65 GeV pions in the region $0.20 < |\eta| < 0.25$.

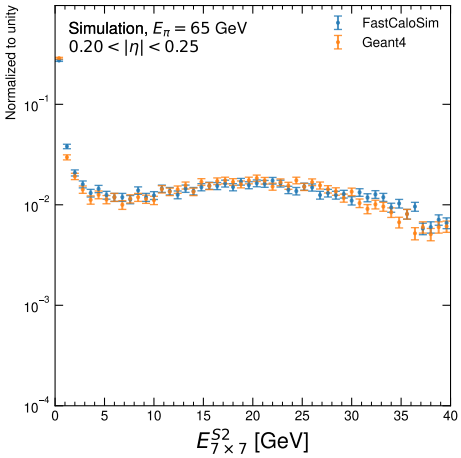

(a)

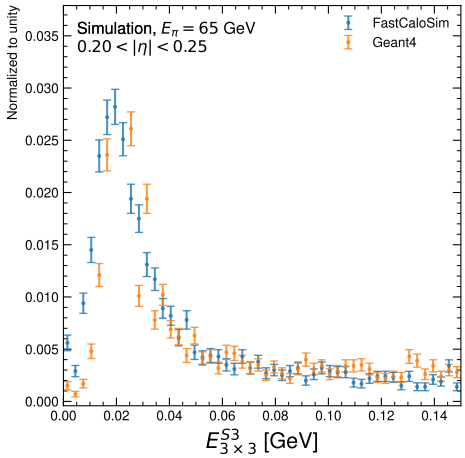

(b)

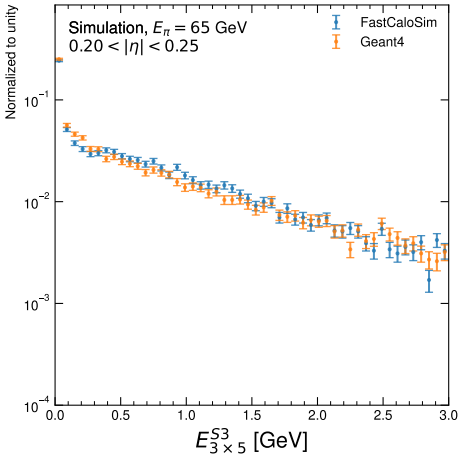

(c)

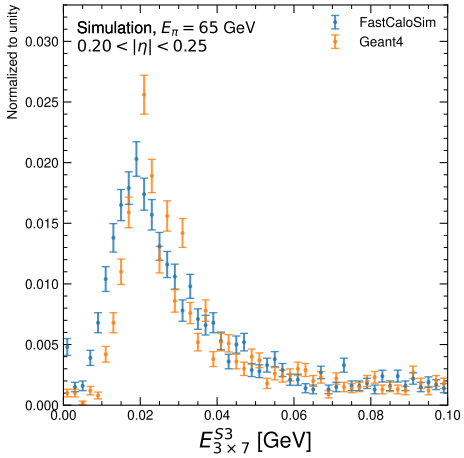

(d)

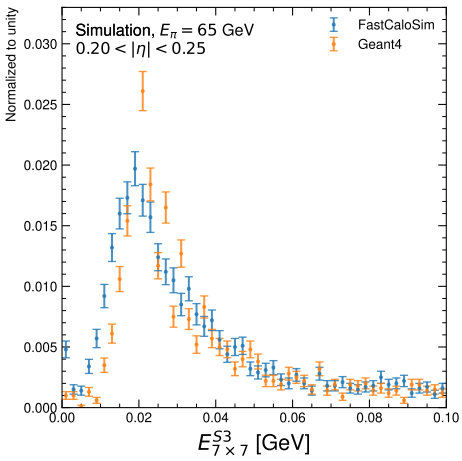

(e)

Figure A.20.: Distributions for energy windows $\eta \times \phi$ around the cell with the most deposited energy in the second and third layer of the electromagnetic barrel (S2 and S3) for 65 GeV pions in the region $0.20 < |\eta| < 0.25$.

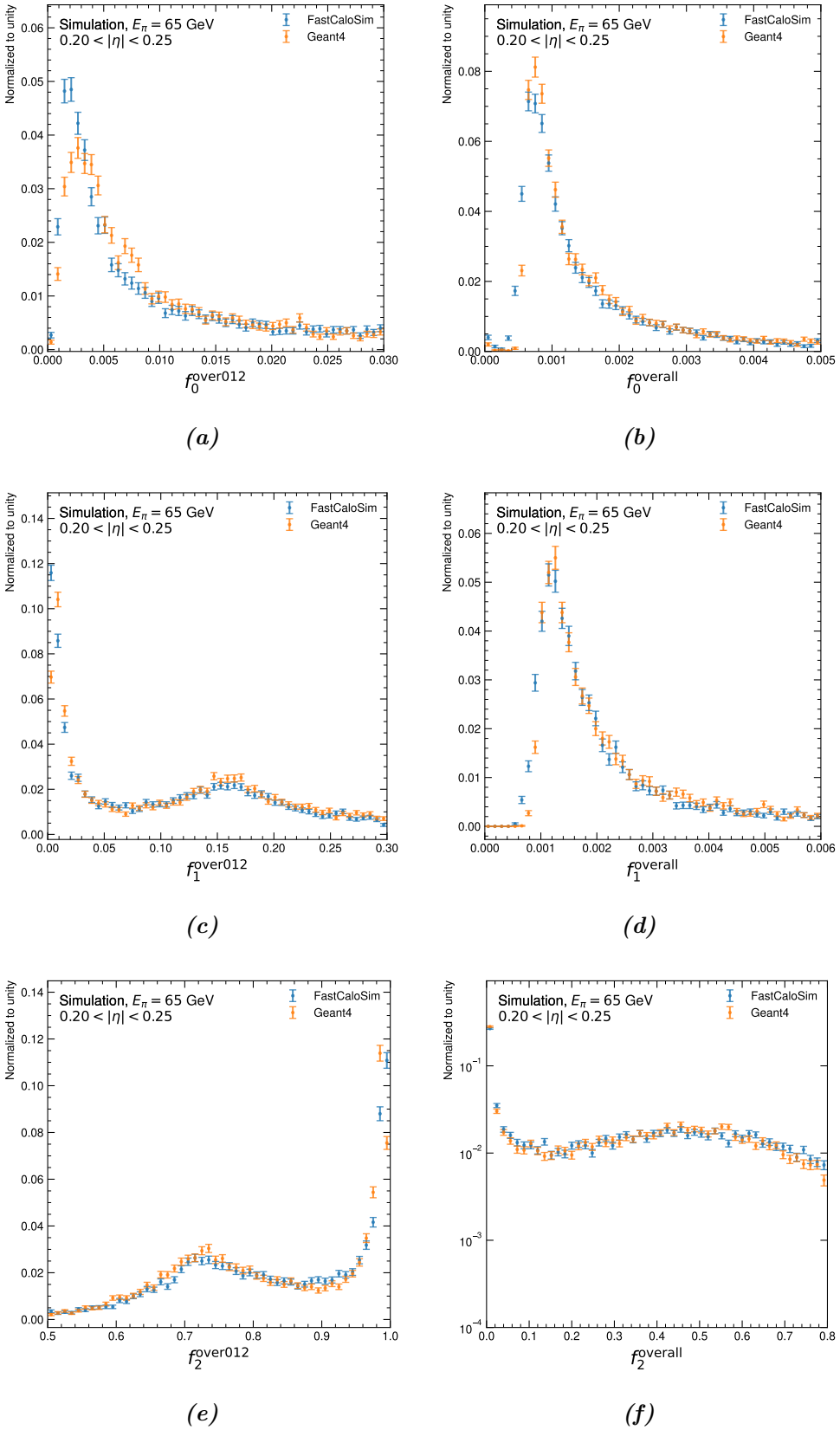

Figure A.21.: Distributions of fractions of energy in the first three layers over the sum of these (a), (c) and (e) and over the whole calorimeter (b), (d) and f for 65 GeV pions in the region $0.20 < |\eta| < 0.25$.

A.2. Electrons and photons in comparison

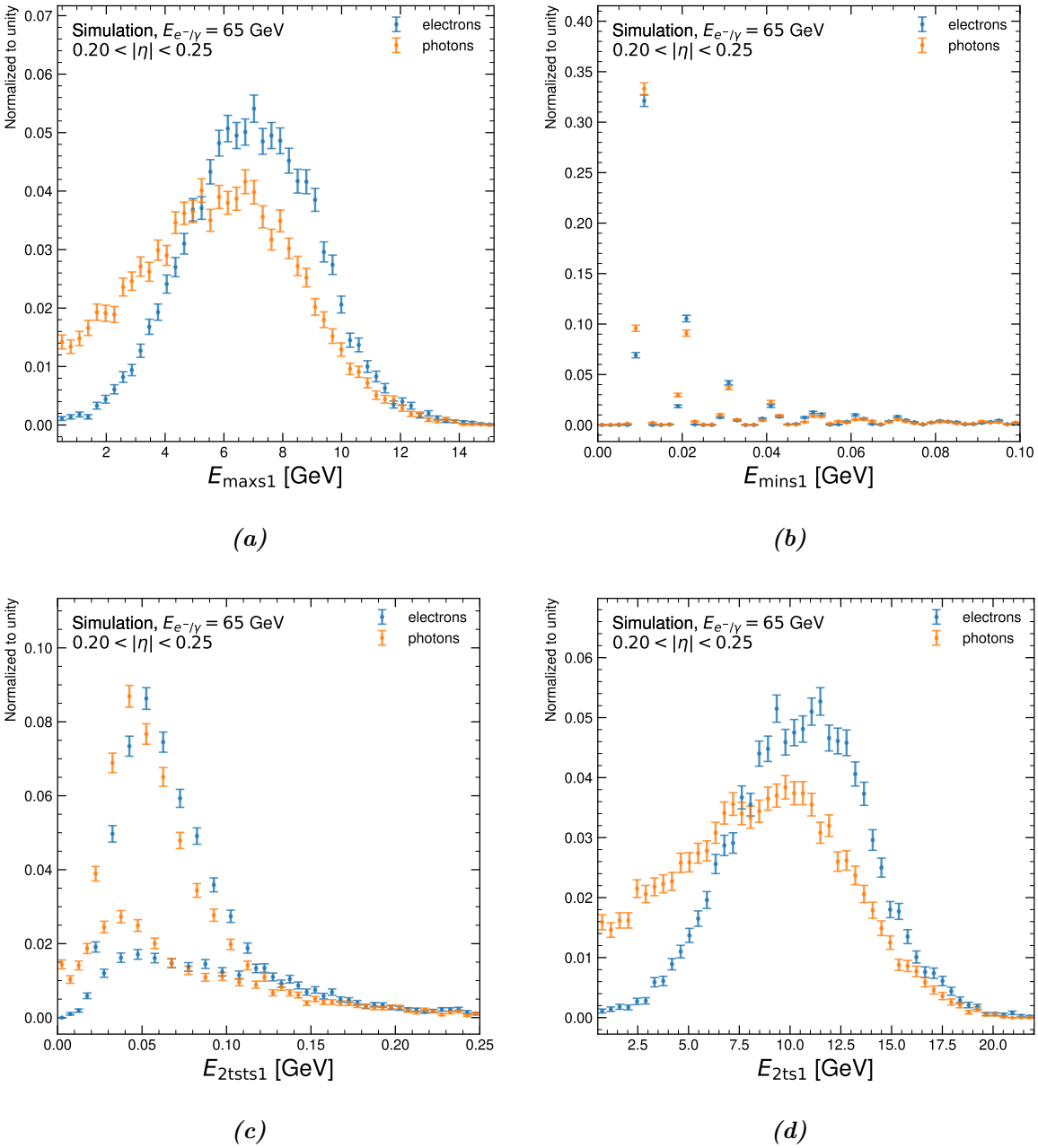

Figure A.22.: Distributions of the shower shape variables E_{maxs1}, E_{mins1}, E_{2tsts1} and E_{2ts1} for 65 GeV electrons and photons in the region $0.20 < |\eta| < 0.25$ in comparison for FastCaloSim.

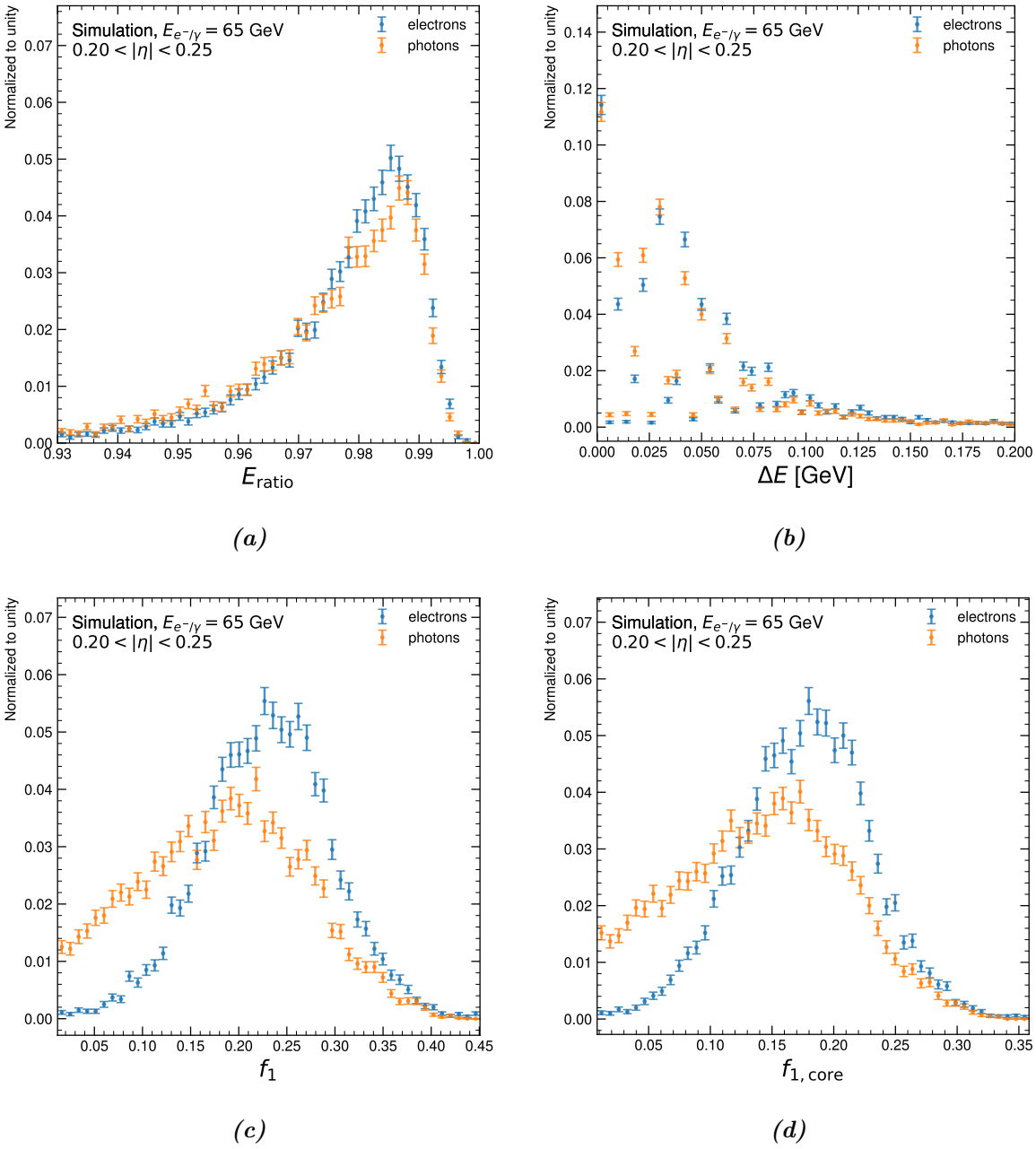

Figure A.23.: Distributions of the shower shape variables E_{ratio}, ΔE, f_1 and $f_{1,\text{core}}$ for 65 GeV electrons and photons in the region $0.20 < |\eta| < 0.25$ in comparison for FastCaloSim.

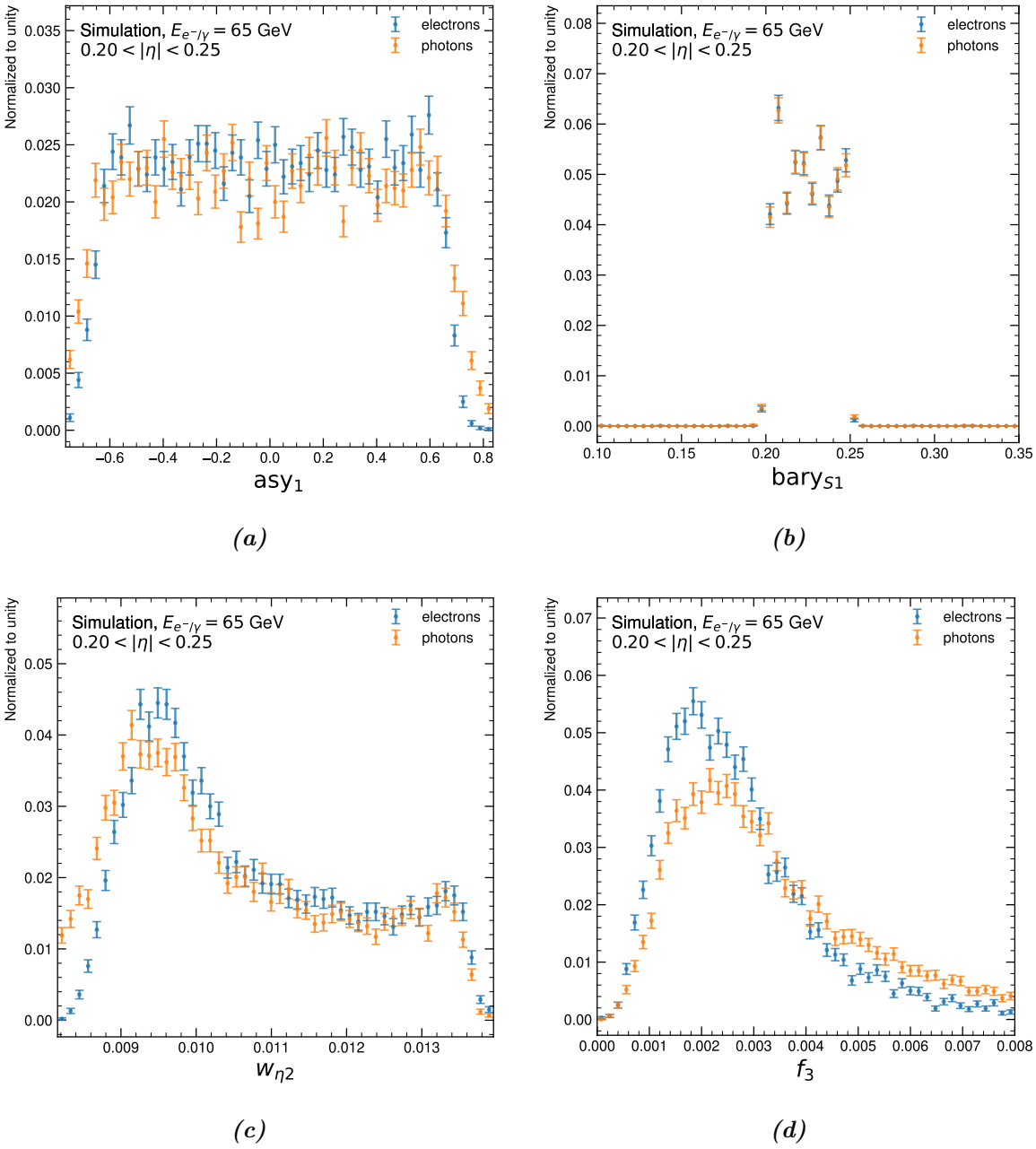

Figure A.24.: Distributions of the shower shape variables asy_1, bary_{S1}, $w_{\eta 2}$ and f_3 for 65 GeV electrons and photons in the region $0.20 < |\eta| < 0.25$ in comparison for FastCaloSim.

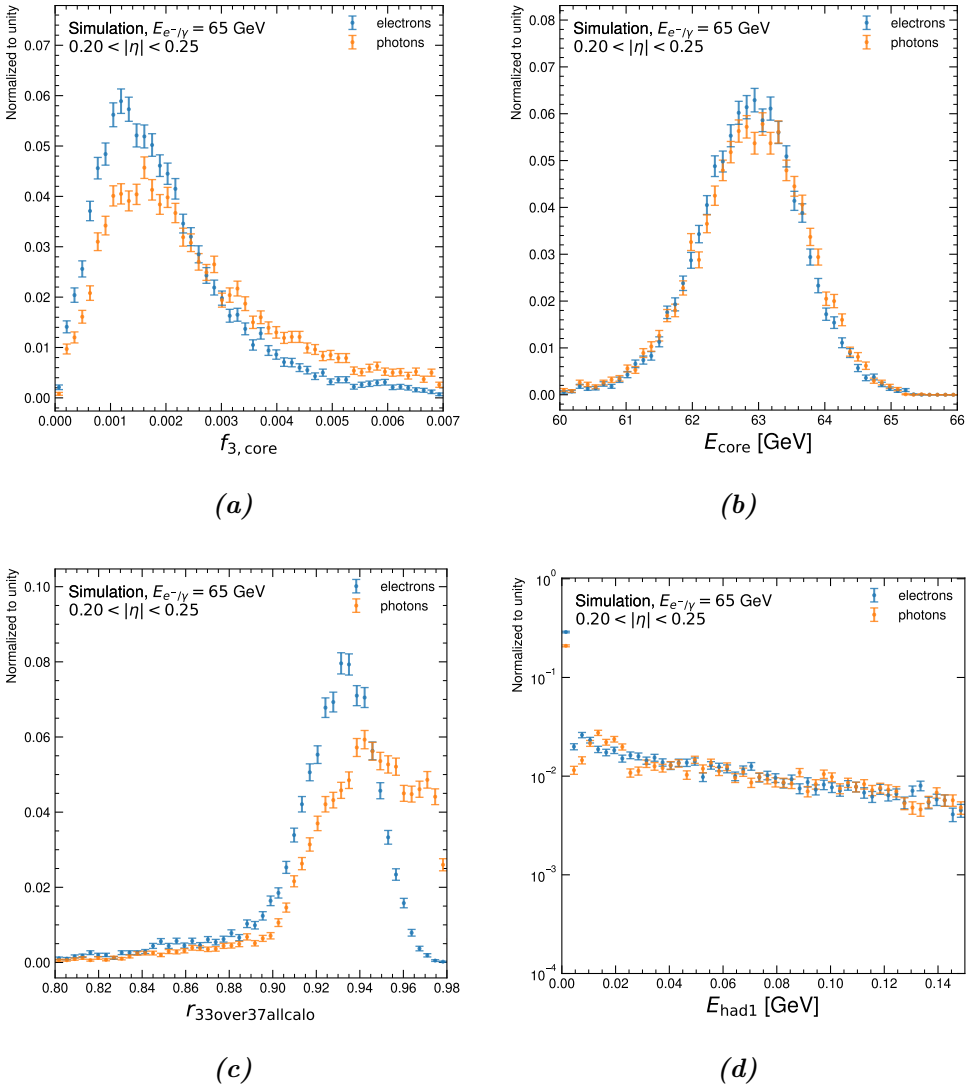

Figure A.25.: Distributions of the shower shape variables $f_{3,\mathrm{core}}$, E_{core}, $r_{33\mathrm{over}37\mathrm{allcalo}}$ and E_{had} for 65 GeV electrons and photons in the region $0.20 < |\eta| < 0.25$ in comparison for FastCaloSim.

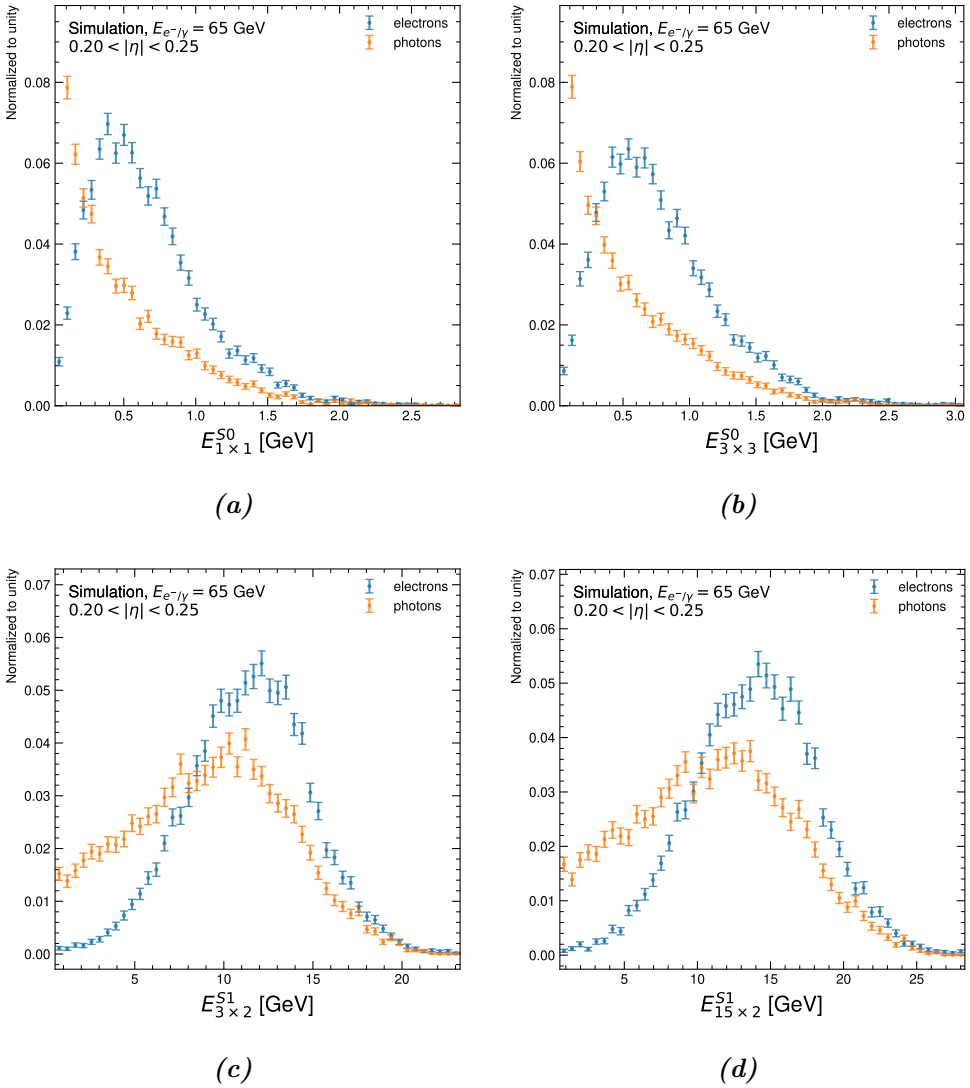

Figure A.26.: Distributions for energy windows in $\eta \times \phi$ around the cell with the most deposited energy in the presampler (S0) and the first layer of the electromagnetic barrel (S1) for 65 GeV electrons and photons in the region $0.20 < |\eta| < 0.25$ in comparison for FastCaloSim.

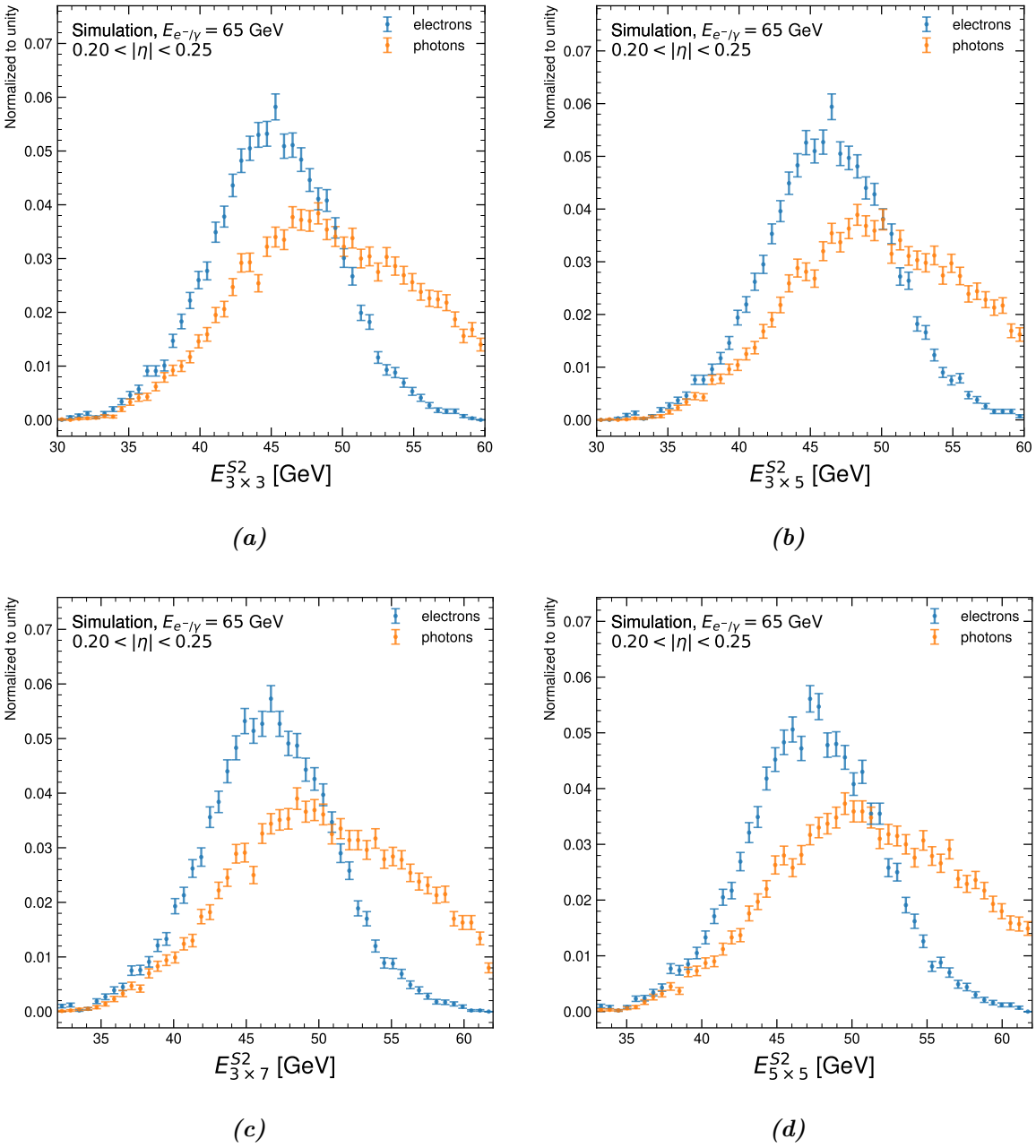

(a) *(b)*

(c) *(d)*

Figure A.27.: Distributions for energy windows in $\eta \times \phi$ around the cell with the most deposited energy in the second layer of the electromagnetic barrel (S2) for 65 GeV electrons and photons in the region $0.20 < |\eta| < 0.25$ in comparison for FastCaloSim.

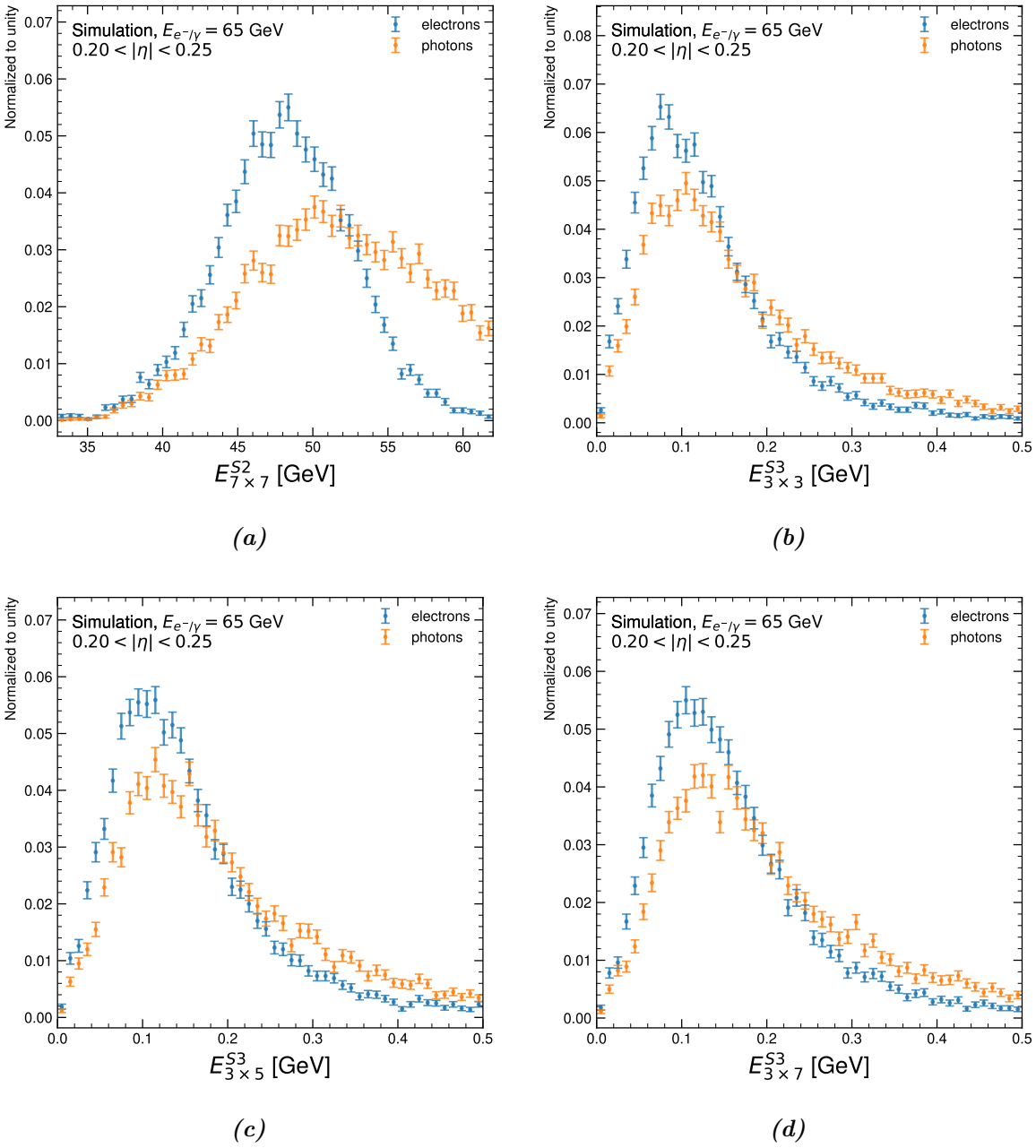

Figure A.28.: Distributions for energy windows in $\eta \times \phi$ around the cell with the most deposited energy in the second and third layer of the electromagnetic barrel (S2 and S3) for 65 GeV electrons and photons in the region $0.20 < |\eta| < 0.25$ in comparison.

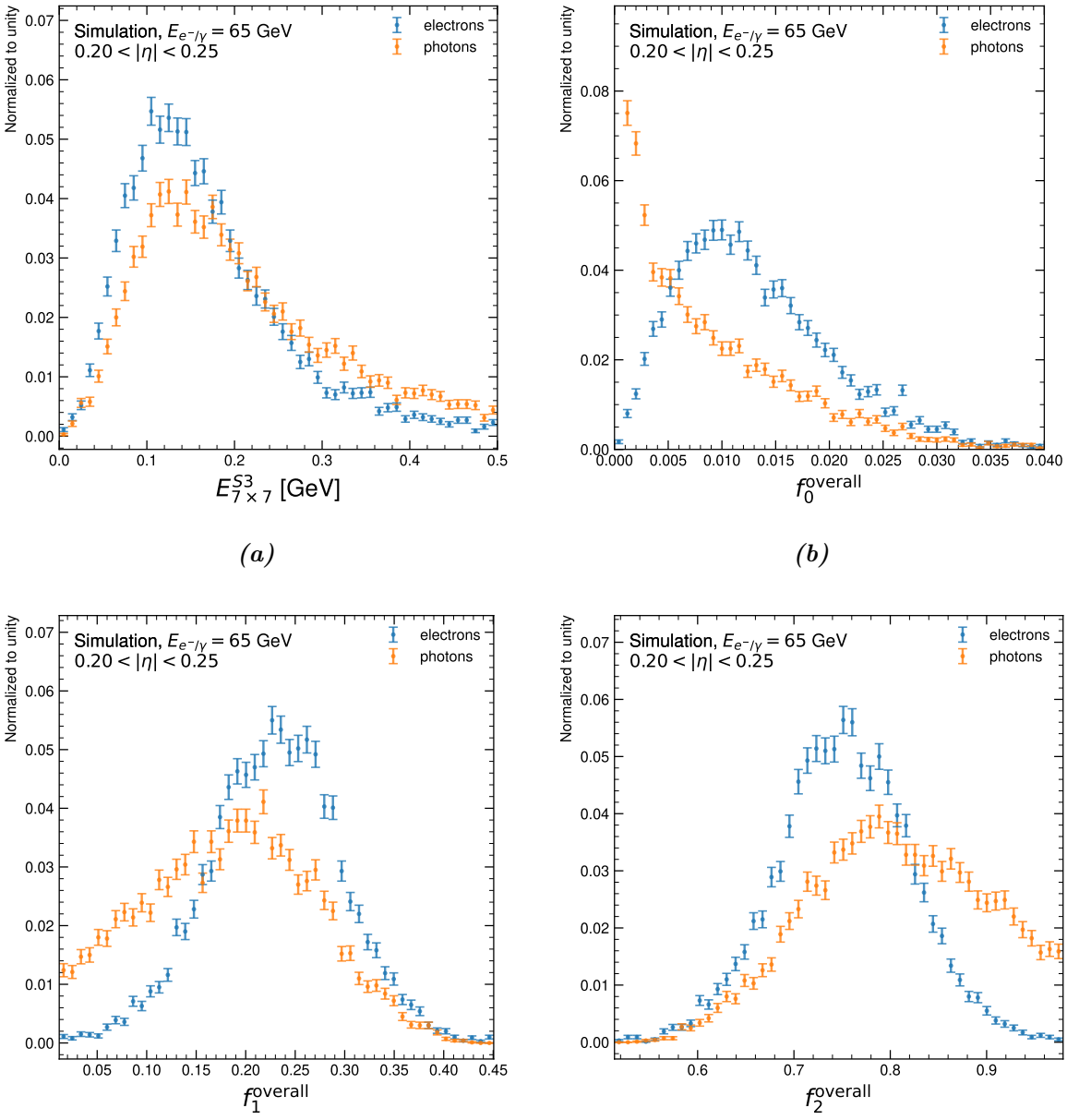

Figure A.29.: Distributions for an energy window in $\eta \times \phi$ around the cell with the most deposited energy in the third layer of the electromagnetic barrel (S3) (a) and for fractions of energy in the first three layers over the energy in the whole calorimeter (b)-(d) for 65 GeV electrons and photons in the region $0.20 < |\eta| < 0.25$ in comparison for FastCaloSim.

A.3. Electromagnetic and hadronic showers in comparison

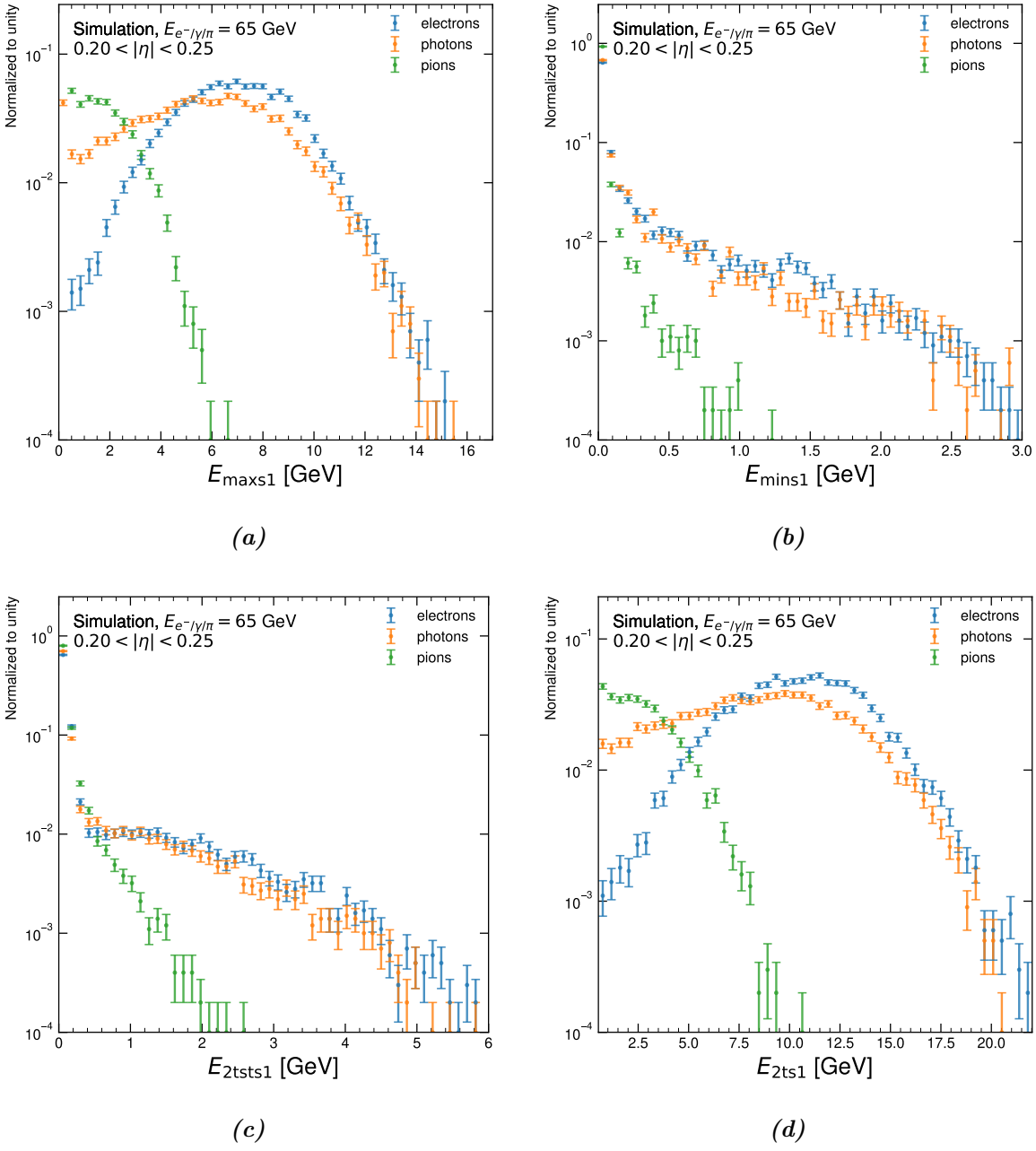

Figure A.30.: Distributions for E_{maxs1}, E_{mins1}, E_{2tsts1} and E_{2ts1} for 65 GeV electromagnetic and hadronic showers in the region $0.20 < |\eta| < 0.25$ in comparison for FastCaloSim.

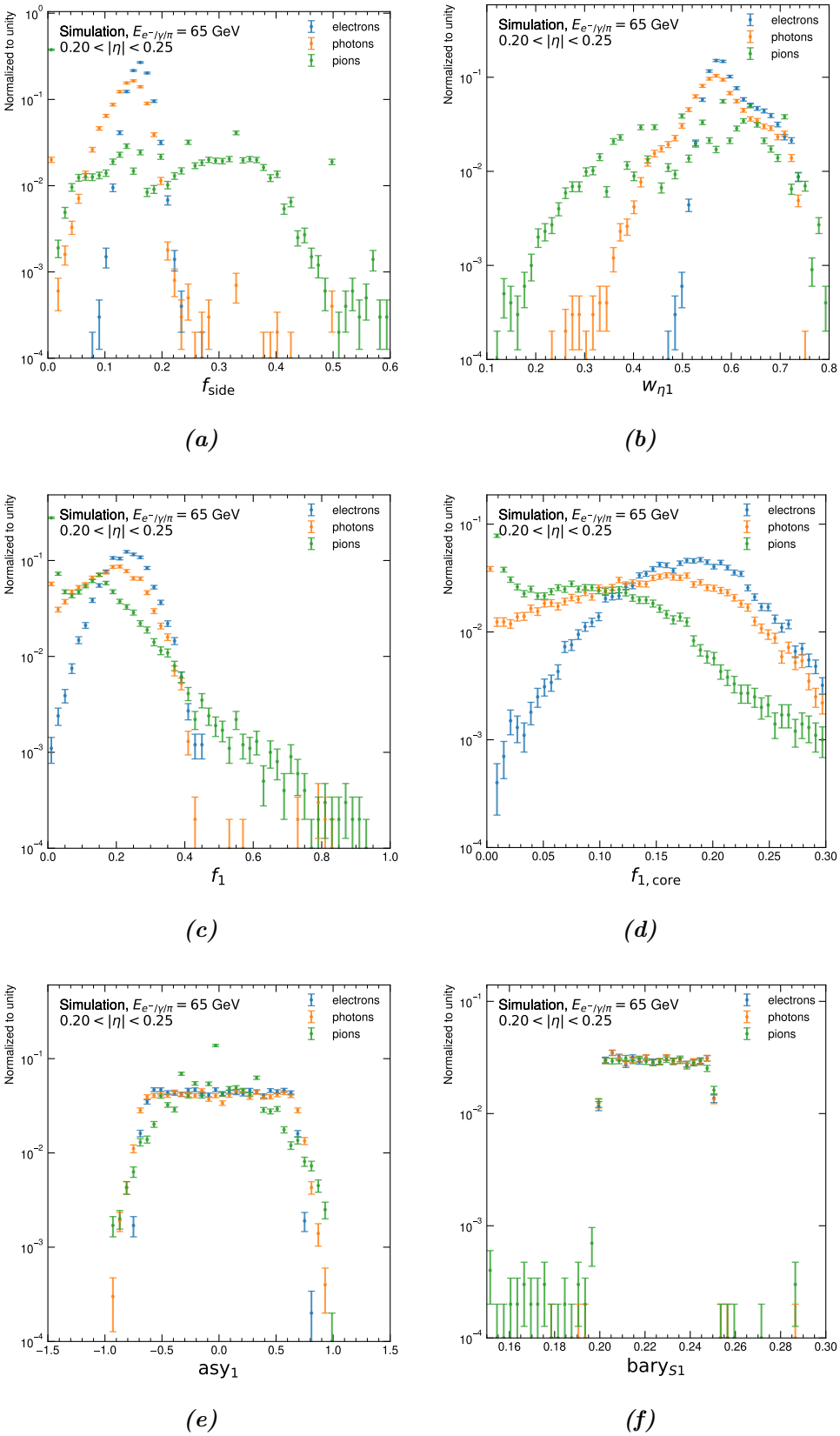

Figure A.31.: Distributions of the shower shape variables f_{side}, $w_{\eta 1}$, f_1, $f_{1,\text{core}}$, asy_1 and bary_{S1} for 65 GeV electromagnetic and hadronic showers in the region $0.20 < |\eta| < 0.25$ in comparison for FastCaloSim.

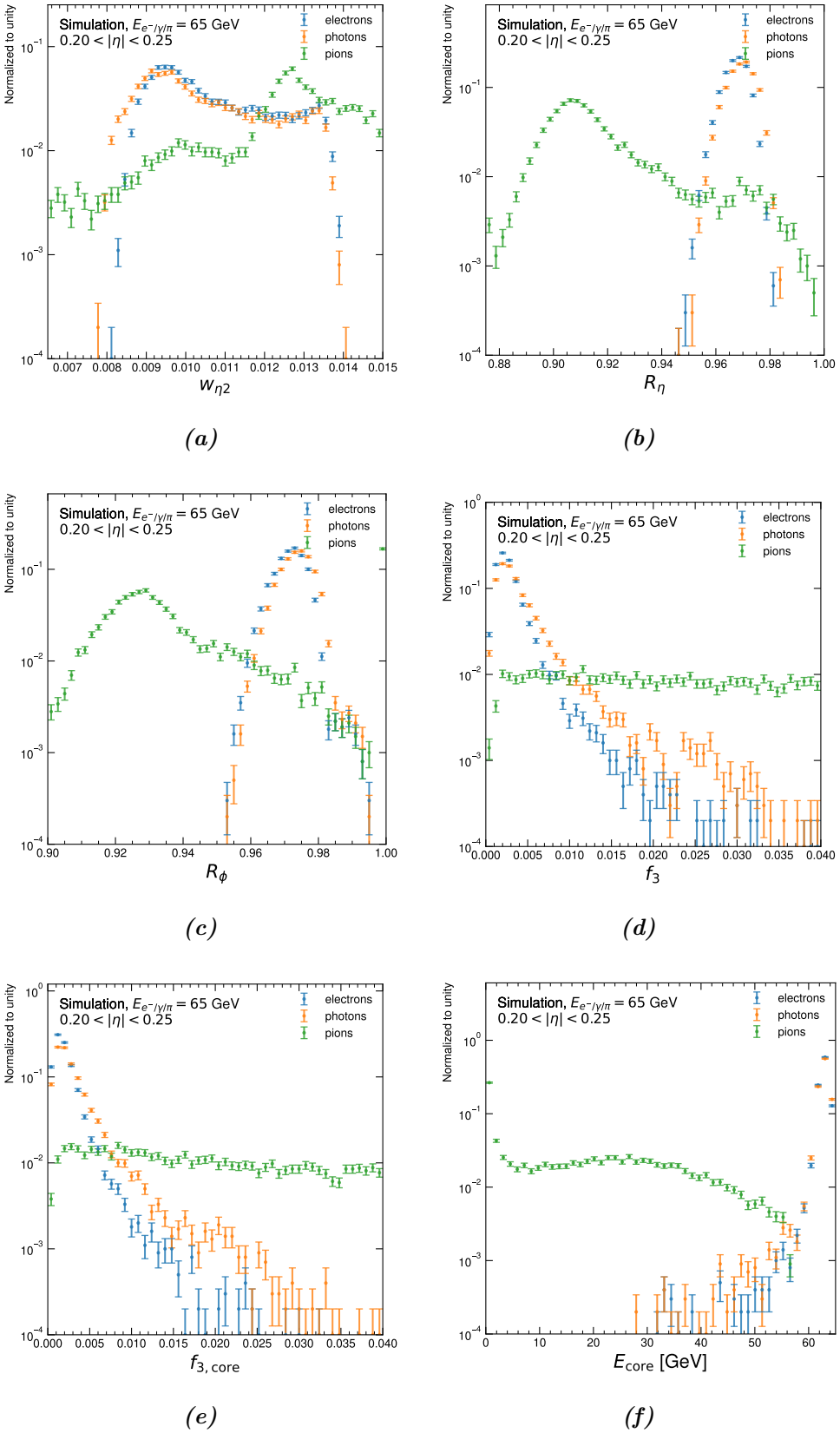

Figure A.32.: Distributions of the shower shape variables $w_{\eta 2}$, R_η, R_ϕ, f_3, $f_{3,\mathrm{core}}$ and E_{core} for 65 GeV electromagnetic and hadronic showers in the region $0.20 < |\eta| < 0.25$ in comparison for FastCaloSim.

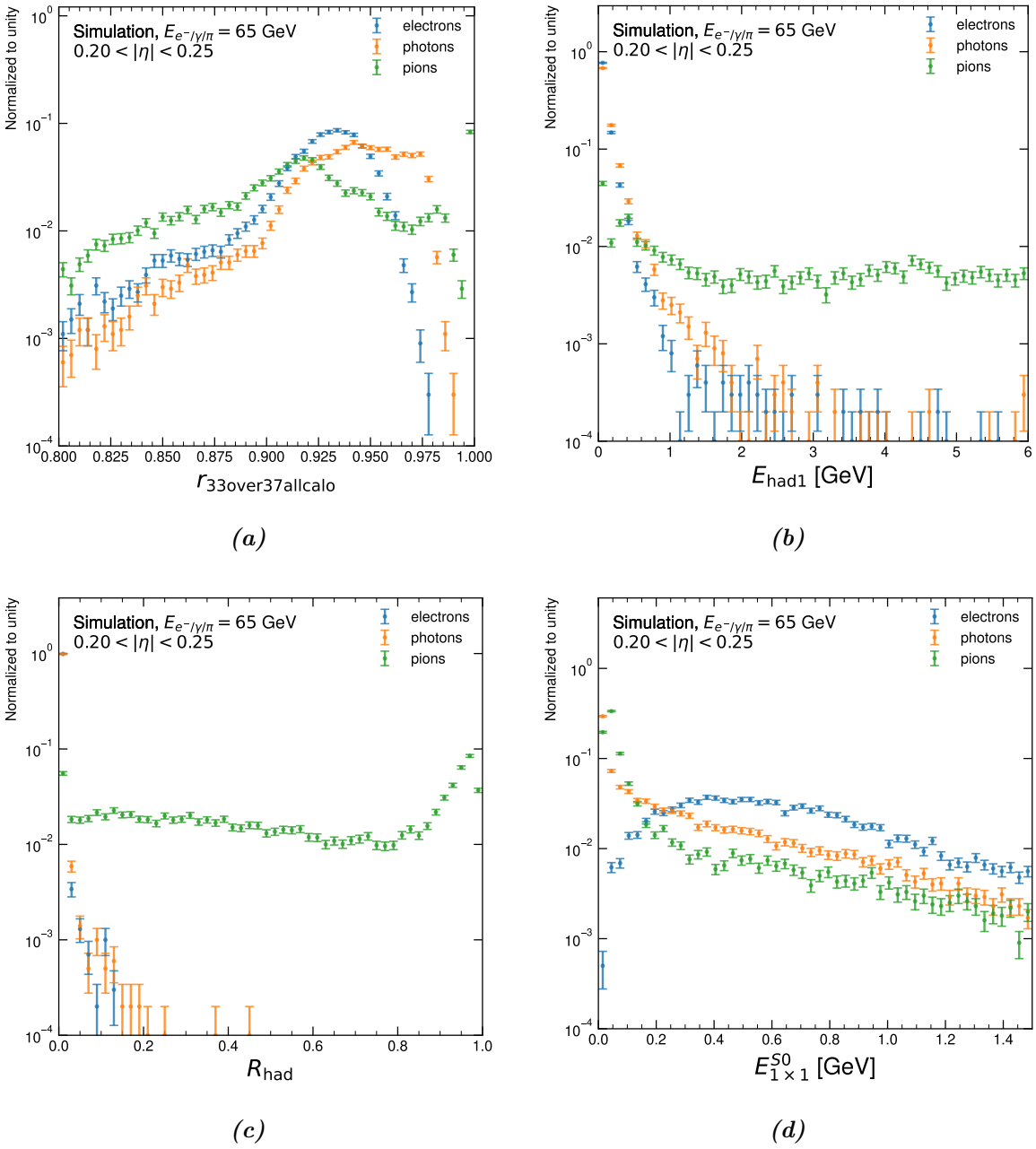

Figure A.33.: Distributions of the shower shape variables $r_{33over37allcalo}$ (a) and E_{had} (b) and R_{had} (c) and an energy window in $\eta \times \phi$ in the presampler (S0) for 65 GeV electromagnetic and hadronic showers in the region $0.20 < |\eta| < 0.25$ in comparison for FastCaloSim.

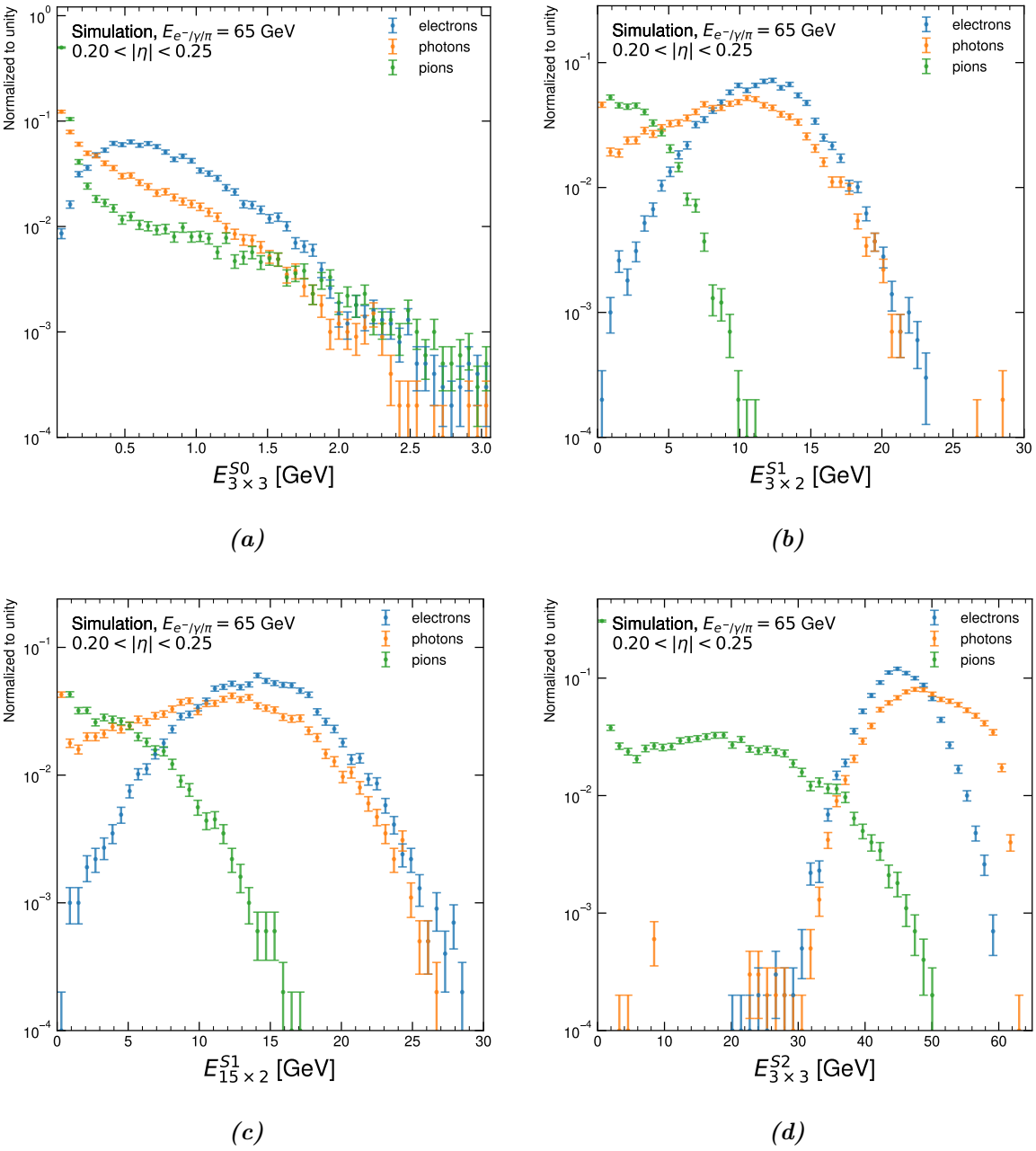

(a) *(b)* *(c)* *(d)*

Figure A.34.: Distributions for energy windows in $\eta \times \phi$ around the cell with the most deposited energy in the presampler (S0) and the first two layers of the electromagnetic barrel (S1 and S2) for 65 GeV electromagnetic and hadronic showers in the region $0.20 < |\eta| < 0.25$ in comparison for FastCaloSim.

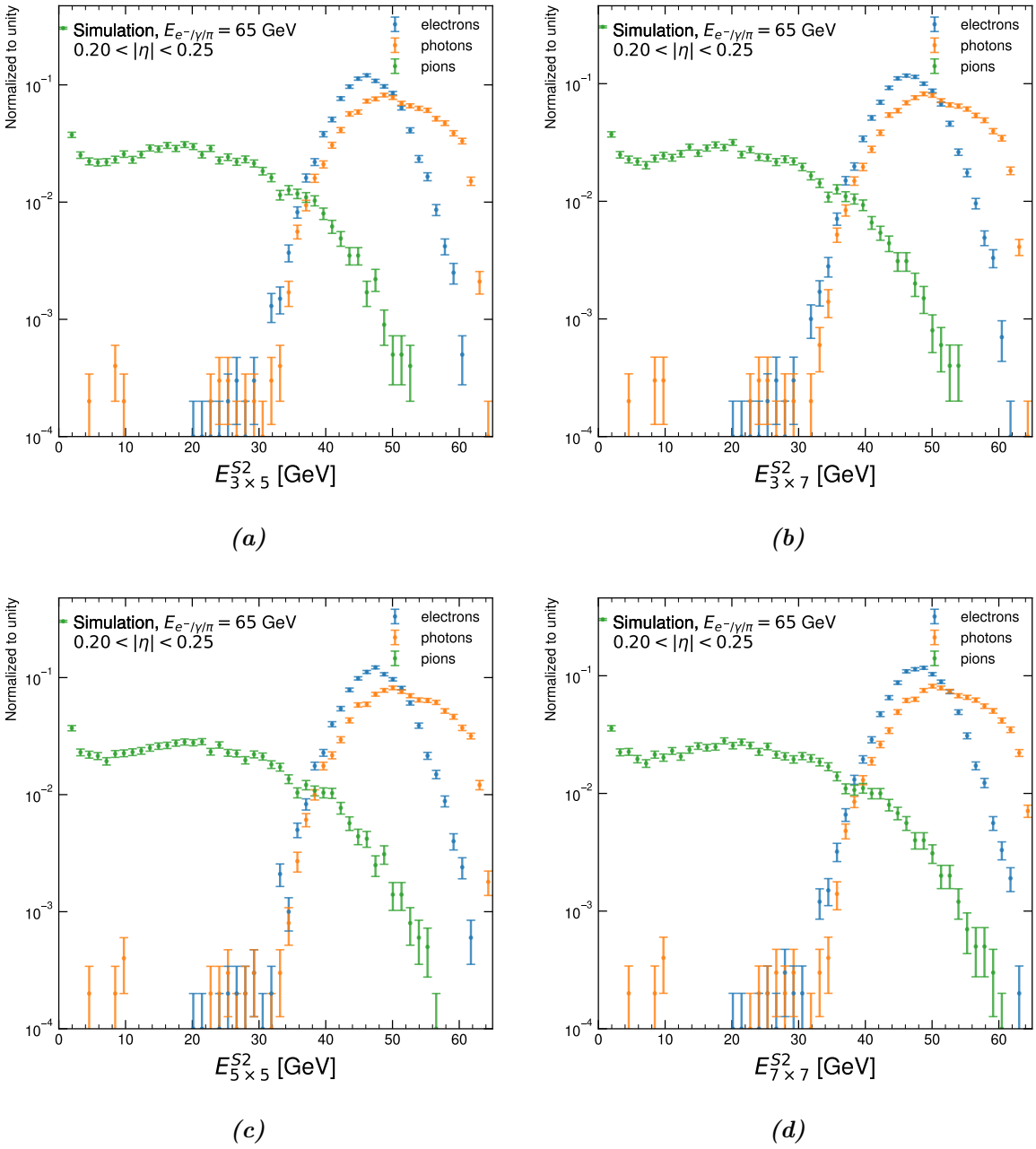

(a) *(b)*

(c) *(d)*

Figure A.35.: Distributions for energy windows $\eta \times \phi$ around the cell with the most deposited energy in the second layer of the electromagnetic barrel (S2) for 65 GeV electromagnetic and hadronic showers in the region $0.20 < |\eta| < 0.25$ in comparison for FastCaloSim.

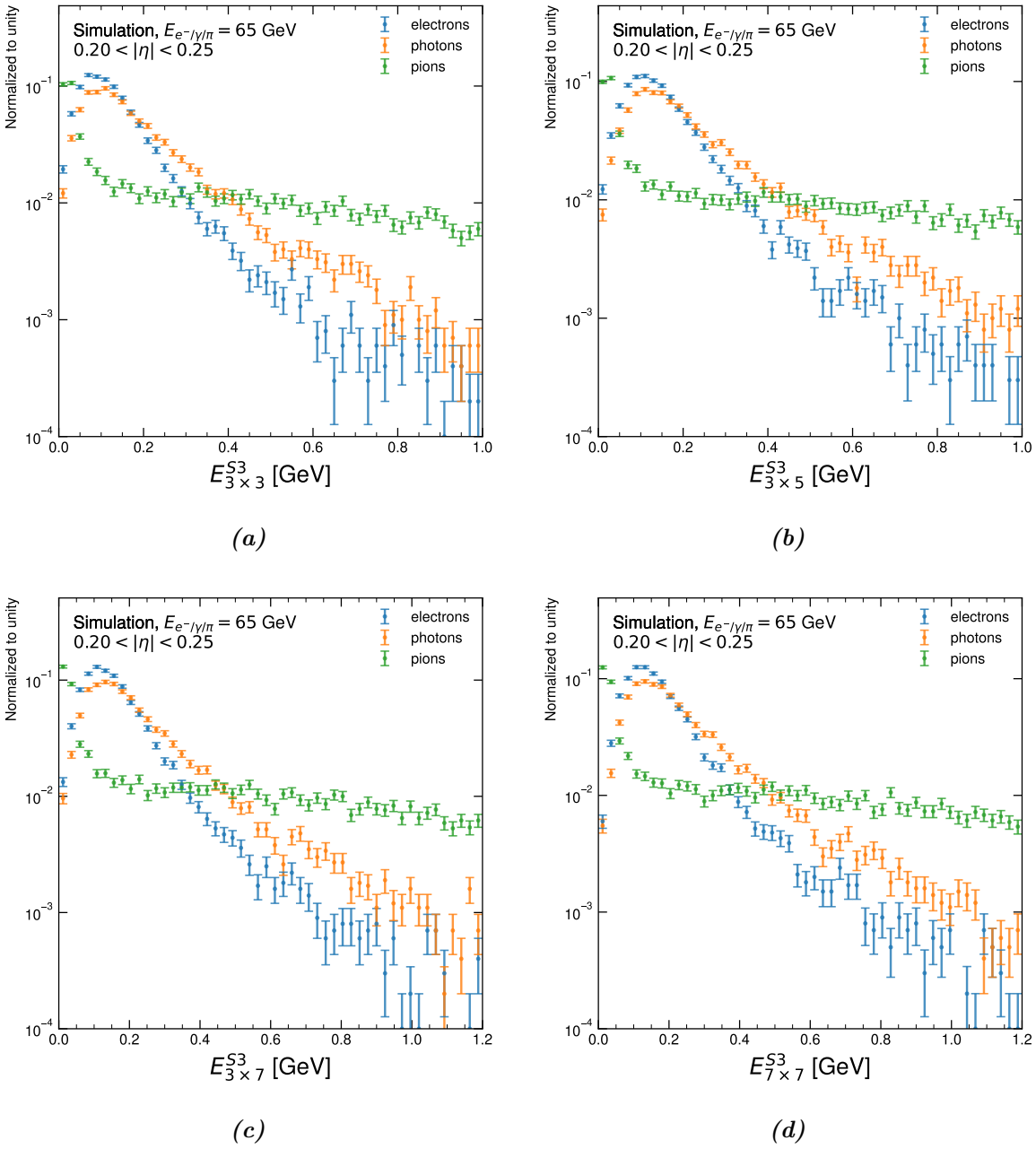

(a) *(b)*

(c) *(d)*

Figure A.36.: Distributions for energy windows $\eta \times \phi$ around the cell with the most deposited energy in the third layer of the electromagnetic barrel (S3) for 65 GeV electromagnetic and hadronic showers in the region $0.20 < |\eta| < 0.25$ in comparison for FastCaloSim.

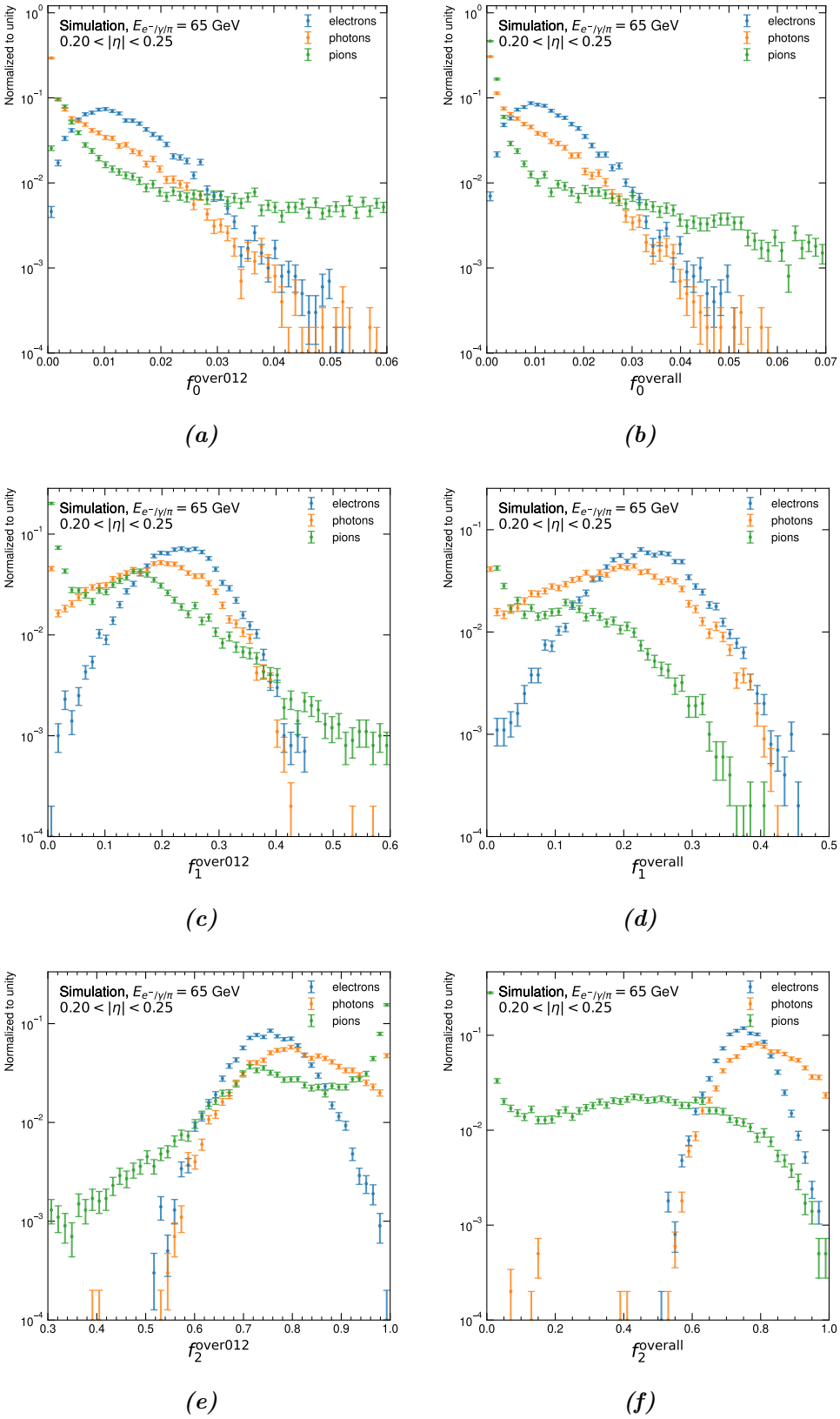

Figure A.37.: Distributions of fractions of energy in the first three layers over the sum of these (a), (c) and (e) and over the whole calorimeter (b), (d) and (f) for 65 GeV electromagnetic and hadronic showers in the region $0.20 < |\eta| < 0.25$ in comparison for FastCaloSim.

B. Means of the shower shape variables

Table B.1.: Mean of the shower shape variables for 65 GeV electrons in the region $0.20 < |\eta| < 0.25$ for FastCaloSim (FCS) and GEANT4 (G4) in comparison.

variable	FastCaloSim	GEANT4	relative difference in %
E_{tot} [GeV]	64.58 ± 0.009247	64.69 ± 0.007276	0.1796 ± 0.9247
$E^{S0}_{1\times1}$ [MeV]	672.1 ± 3.991	674.9 ± 3.981	0.4082 ± 396.5
$E^{S0}_{3\times3}$ [MeV]	787.6 ± 4.493	782.1 ± 4.411	0.7105 ± 444.2
$w_{\eta1}$	0.6043 ± 0.0004992	0.6066 ± 0.0005071	0.3848 ± 0.09657
w_{stot}	1.682 ± 0.0009716	1.685 ± 0.001336	0.1609 ± 0.1453
E_{ratio}	0.8731 ± 0.002306	0.8755 ± 0.002355	0.2746 ± 0.3529
f_1	0.2301 ± 0.0006677	0.2308 ± 0.0006455	0.3012 ± 0.2964
$E^{S1}_{3\times2}$ [GeV]	11.39 ± 0.03451	11.39 ± 0.03337	0.007902 ± 3.451
$E^{S1}_{15\times2}$ [GeV]	13.92 ± 0.04314	13.98 ± 0.04197	0.3927 ± 4.314
f_{side}	0.1606 ± 0.0001792	0.1655 ± 0.0002604	2.98 ± 0.1112
E_{maxs1} [GeV]	6.97 ± 0.02237	6.928 ± 0.02134	0.6056 ± 2.237
E_{had1} [MeV]	99.19 ± 3.178	85.49 ± 2.095	16.03 ± 243.1
$f_{1,\text{core}}$	0.1766 ± 0.000533	0.1763 ± 0.0005142	0.2173 ± 0.3067
$r_{33\text{over}37\text{allcalo}}$	0.922 ± 0.0003004	0.9219 ± 0.0003099	0.01356 ± 0.04498
E_{core} [GeV]	62.72 ± 0.01529	62.78 ± 0.01511	0.09748 ± 1.529
E_{mins1} [MeV]	242.8 ± 4.964	73.56 ± 2.953	230.1 ± 974.7
asy_1	0.004064 ± 0.003951	-0.00184 ± 0.00386	-320.9 ± 214.7
bary_{S1}	0.003511 ± 0.002252	0.003518 ± 0.002252	0.1996 ± 64.01
$E_{2\text{tsts1}}$ [MeV]	463.4 ± 8.906	455.3 ± 9.048	1.764 ± 920.8
$E_{2\text{ts1}}$ [GeV]	10.53 ± 0.03318	10.51 ± 0.03189	0.1303 ± 3.318
ΔE [MeV]	220.5 ± 8.733	330.5 ± 7.998	33.27 ± 533.8
R_η	$0.9672 \pm 4.595{\cdot}10^{-5}$	$0.9675 \pm 5.223{\cdot}10^{-5}$	0.03308 ± 0.007058
R_ϕ	$0.9714 \pm 4.923{\cdot}10^{-5}$	$0.972 \pm 5.322{\cdot}10^{-5}$	0.05504 ± 0.007344

variable	FastCaloSim	GEANT4	relative difference in %
$w_{\eta 2}$	$0.0107 \pm 1.435{\cdot}10^{-5}$	$0.01072 \pm 1.463{\cdot}10^{-5}$	0.1921 ± 0.1339
$E^{S2}_{3\times3}$ [GeV]	45.14 ± 0.04499	45.2 ± 0.04458	0.1323 ± 4.499
$E^{S2}_{3\times5}$ [GeV]	46.21 ± 0.04529	46.25 ± 0.04464	0.0839 ± 4.529
$E^{S2}_{5\times5}$ [GeV]	47.34 ± 0.0456	47.37 ± 0.0447	0.06438 ± 4.56
$E^{S2}_{3\times7}$ [GeV]	46.46 ± 0.04536	46.5 ± 0.04464	0.07119 ± 4.536
$E^{S2}_{7\times7}$ [GeV]	48.03 ± 0.04578	48.04 ± 0.0447	0.03205 ± 4.578
$E^{S3}_{3\times3}$ [MeV]	150.5 ± 1.619	148.7 ± 1.551	1.213 ± 157
$E^{S3}_{3\times5}$ [MeV]	176.3 ± 1.829	169.8 ± 1.62	3.792 ± 168.2
$E^{S3}_{3\times7}$ [MeV]	186.4 ± 1.897	178 ± 1.636	4.711 ± 171.4
$E^{S3}_{7\times7}$ [MeV]	197.7 ± 1.968	187 ± 1.65	5.736 ± 174.4
f_3	$0.003203 \pm 3.242{\cdot}10^{-5}$	$0.003158 \pm 2.729{\cdot}10^{-5}$	1.427 ± 1.027
$f_{3,\mathrm{core}}$	$0.002346 \pm 2.581{\cdot}10^{-5}$	$0.002316 \pm 2.534{\cdot}10^{-5}$	1.302 ± 1.114
f_0^{overall}	$0.01349 \pm 7.554{\cdot}10^{-5}$	$0.01332 \pm 7.123{\cdot}10^{-5}$	1.216 ± 0.567
f_1^{overall}	0.2297 ± 0.0006678	0.2304 ± 0.0006456	0.3233 ± 0.2969
f_2^{overall}	0.7517 ± 0.0006924	0.7514 ± 0.0006718	0.03593 ± 0.1141
f_0^{over012}	$0.01355 \pm 7.579{\cdot}10^{-5}$	$0.01338 \pm 7.147{\cdot}10^{-5}$	1.249 ± 0.5664
f_1^{over012}	0.2307 ± 0.0006674	0.2314 ± 0.0006452	0.2999 ± 0.2955
f_2^{over012}	0.7557 ± 0.0007095	0.7552 ± 0.0006877	0.06978 ± 0.1165
R_{had}	$0.001539 \pm 4.936{\cdot}10^{-5}$	$0.001425 \pm 6.182{\cdot}10^{-5}$	7.983 ± 3.463
E_T [GeV]	62.99 ± 0.009207	62.98 ± 0.007338	0.02509 ± 0.9207
E_T^{Had} [MeV]	96.71 ± 3.097	88.91 ± 3.723	8.781 ± 405

Table B.2.: RMS of the shower shape variables for 65 GeV electrons in the region $0.20 < |\eta| < 0.25$ for FastCaloSim (FCS) and GEANT4 (G4) in comparison.

variable	FastCaloSim	GEANT4	relative difference in %
E_{tot} [GeV]	64.58 ± 0.009247	64.69 ± 0.007276	0.1796 ± 0.9247
$E^{S0}_{1\times1}$ [MeV]	672.1 ± 3.991	674.9 ± 3.981	0.4082 ± 396.5
$E^{S0}_{3\times3}$ [MeV]	787.6 ± 4.493	782.1 ± 4.411	0.7105 ± 444.2
$w_{\eta1}$	0.6043 ± 0.0004992	0.6066 ± 0.0005071	0.3848 ± 0.09657
w_{stot}	1.682 ± 0.0009716	1.685 ± 0.001336	0.1609 ± 0.1453
E_{ratio}	0.8731 ± 0.002306	0.8755 ± 0.002355	0.2746 ± 0.3529
f_1	0.2301 ± 0.0006677	0.2308 ± 0.0006455	0.3012 ± 0.2964
$E^{S1}_{3\times2}$ [GeV]	11.39 ± 0.03451	11.39 ± 0.03337	0.007902 ± 3.451
$E^{S1}_{15\times2}$ [GeV]	13.92 ± 0.04314	13.98 ± 0.04197	0.3927 ± 4.314
f_{side}	0.1606 ± 0.0001792	0.1655 ± 0.0002604	2.98 ± 0.1112
E_{maxs1} [GeV]	6.97 ± 0.02237	6.928 ± 0.02134	0.6056 ± 2.237
E_{had1} [MeV]	99.19 ± 3.178	85.49 ± 2.095	16.03 ± 243.1
$f_{1,\text{core}}$	0.1766 ± 0.000533	0.1763 ± 0.0005142	0.2173 ± 0.3067
$r_{\text{33over37allcalo}}$	0.922 ± 0.0003004	0.9219 ± 0.0003099	0.01356 ± 0.04498
E_{core} [GeV]	62.72 ± 0.01529	62.78 ± 0.01511	0.09748 ± 1.529
E_{mins1} [MeV]	242.8 ± 4.964	73.56 ± 2.953	230.1 ± 974.7
asy_1	0.004064 ± 0.003951	-0.00184 ± 0.00386	-320.9 ± 214.7
bary_{S1}	0.003511 ± 0.002252	0.003518 ± 0.002252	0.1996 ± 64.01
E_{2tsts1} [MeV]	463.4 ± 8.906	455.3 ± 9.048	1.764 ± 920.8
E_{2ts1} [GeV]	10.53 ± 0.03318	10.51 ± 0.03189	0.1303 ± 3.318
ΔE [MeV]	220.5 ± 8.733	330.5 ± 7.998	33.27 ± 533.8
R_η	$0.9672 \pm 4.595{\cdot}10^{-5}$	$0.9675 \pm 5.223{\cdot}10^{-5}$	0.03308 ± 0.007058
R_ϕ	$0.9714 \pm 4.923{\cdot}10^{-5}$	$0.972 \pm 5.322{\cdot}10^{-5}$	0.05504 ± 0.007344
$w_{\eta2}$	$0.0107 \pm 1.435{\cdot}10^{-5}$	$0.01072 \pm 1.463{\cdot}10^{-5}$	0.1921 ± 0.1339
$E^{S2}_{3\times3}$ [GeV]	45.14 ± 0.04499	45.2 ± 0.04458	0.1323 ± 4.499
$E^{S2}_{3\times5}$ [GeV]	46.21 ± 0.04529	46.25 ± 0.04464	0.0839 ± 4.529
$E^{S2}_{5\times5}$ [GeV]	47.34 ± 0.0456	47.37 ± 0.0447	0.06438 ± 4.56
$E^{S2}_{3\times7}$ [GeV]	46.46 ± 0.04536	46.5 ± 0.04464	0.07119 ± 4.536
$E^{S2}_{7\times7}$ [GeV]	48.03 ± 0.04578	48.04 ± 0.0447	0.03205 ± 4.578
$E^{S3}_{3\times3}$ [MeV]	150.5 ± 1.619	148.7 ± 1.551	1.213 ± 157
$E^{S3}_{3\times5}$ [MeV]	176.3 ± 1.829	169.8 ± 1.62	3.792 ± 168.2
$E^{S3}_{3\times7}$ [MeV]	186.4 ± 1.897	178 ± 1.636	4.711 ± 171.4
$E^{S3}_{7\times7}$ [MeV]	197.7 ± 1.968	187 ± 1.65	5.736 ± 174.4
f_3	$0.003203 \pm 3.242{\cdot}10^{-5}$	$0.003158 \pm 2.729{\cdot}10^{-5}$	1.427 ± 1.027
$f_{3,\text{core}}$	$0.002346 \pm 2.581{\cdot}10^{-5}$	$0.002316 \pm 2.534{\cdot}10^{-5}$	1.302 ± 1.114

variable	FastCaloSim	GEANT4	relative difference in %
f_0^{overall}	$0.01349 \pm 7.554{\cdot}10^{-5}$	$0.01332 \pm 7.123{\cdot}10^{-5}$	1.216 ± 0.567
f_1^{overall}	0.2297 ± 0.0006678	0.2304 ± 0.0006456	0.3233 ± 0.2969
f_2^{overall}	0.7517 ± 0.0006924	0.7514 ± 0.0006718	0.03593 ± 0.1141
f_0^{over012}	$0.01355 \pm 7.579{\cdot}10^{-5}$	$0.01338 \pm 7.147{\cdot}10^{-5}$	1.249 ± 0.5664
f_1^{over012}	0.2307 ± 0.0006674	0.2314 ± 0.0006452	0.2999 ± 0.2955
f_2^{over012}	0.7557 ± 0.0007095	0.7552 ± 0.0006877	0.06978 ± 0.1165
R_{had}	$0.001539 \pm 4.936{\cdot}10^{-5}$	$0.001425 \pm 6.182{\cdot}10^{-5}$	7.983 ± 3.463
E_T [GeV]	62.99 ± 0.009207	62.98 ± 0.007338	0.02509 ± 0.9207
E_T^{Had} [MeV]	96.71 ± 3.097	88.91 ± 3.723	8.781 ± 405

Table B.3.: Mean of the shower shape variables for 65 GeV photons in the region $0.20 < |\eta| < 0.25$ for FastCaloSim (FCS) and GEANT4 (G4) in comparison.

variable	FastCaloSim	GEANT4	relative difference in %
E_{tot} [GeV]	64.55 ± 0.01197	64.65 ± 0.009793	0.1623 ± 1.197
$E^{S0}_{1\times1}$ [MeV]	326.6 ± 4.061	351.2 ± 3.987	7.01 ± 370.7
$E^{S0}_{3\times3}$ [MeV]	386.9 ± 4.64	403.1 ± 4.514	4.023 ± 433.2
$w_{\eta1}$	0.5656 ± 0.0009833	0 ± 0	0 ± 0
w_{stot}	1.619 ± 0.002793	0 ± 0	0 ± 0
E_{ratio}	0.8669 ± 0.002303	0.8711 ± 0.002391	0.4734 ± 0.3557
f_1	0.1751 ± 0.0009101	0.1749 ± 0.0008805	0.1561 ± 0.5279
$E^{S1}_{3\times2}$ [GeV]	8.767 ± 0.04602	8.781 ± 0.04412	0.1553 ± 4.602
$E^{S1}_{15\times2}$ [GeV]	10.55 ± 0.05686	10.6 ± 0.05501	0.4623 ± 5.686
f_{side}	0.1364 ± 0.0004769	0 ± 0	0 ± 0
E_{maxs1} [GeV]	5.522 ± 0.02858	5.513 ± 0.02705	0.1703 ± 2.858
E_{had1} [MeV]	157.4 ± 5.963	130.4 ± 4.488	20.71 ± 541.8
$f_{1,\text{core}}$	0.136 ± 0.0007137	0.1359 ± 0.0006806	0.08389 ± 0.5296
$r_{\text{33over37allcalo}}$	0.938 ± 0.000312	0.9387 ± 0.0003182	0.06999 ± 0.046
E_{core} [GeV]	62.68 ± 0.01835	62.8 ± 0.02218	0.1879 ± 1.835
E_{mins1} [MeV]	197 ± 4.266	54.84 ± 2.386	259.2 ± 856.9
asy_1	0.00341 ± 0.004266	0 ± 0	0 ± 0
bary_{S1}	0.003484 ± 0.002252	0.003528 ± 0.002254	1.241 ± 63.82
E_{2tsts1} [MeV]	371.1 ± 7.78	347.6 ± 7.643	6.763 ± 815.9
E_{2ts1} [GeV]	8.129 ± 0.04309	8.138 ± 0.04121	0.1057 ± 4.309
ΔE [MeV]	178.7 ± 7.774	271.3 ± 6.962	34.14 ± 458.5
R_η	$0.9693 \pm 4.995{\cdot}10^{-5}$	$0.9696 \pm 7.35{\cdot}10^{-5}$	0.02104 ± 0.008974
R_ϕ	$0.9734 \pm 5.161{\cdot}10^{-5}$	$0.9739 \pm 6.375{\cdot}10^{-5}$	0.04898 ± 0.008288
$w_{\eta2}$	$0.01048 \pm 1.511{\cdot}10^{-5}$	$0.0105 \pm 1.548{\cdot}10^{-5}$	0.202 ± 0.144
$E^{S2}_{3\times3}$ [GeV]	48.91 ± 0.06034	49.04 ± 0.06055	0.2616 ± 6.034
$E^{S2}_{3\times5}$ [GeV]	49.98 ± 0.06055	50.08 ± 0.06054	0.2087 ± 6.055
$E^{S2}_{5\times5}$ [GeV]	51.12 ± 0.06074	51.21 ± 0.06046	0.1865 ± 6.074
$E^{S2}_{3\times7}$ [GeV]	50.23 ± 0.06057	50.33 ± 0.0605	0.2009 ± 6.057
$E^{S2}_{7\times7}$ [GeV]	51.8 ± 0.06081	51.88 ± 0.06033	0.1621 ± 6.081
$E^{S3}_{3\times3}$ [MeV]	222.6 ± 2.697	219.2 ± 2.716	1.558 ± 275.8
$E^{S3}_{3\times5}$ [MeV]	255.5 ± 2.977	246.1 ± 2.829	3.796 ± 293.6
$E^{S3}_{3\times7}$ [MeV]	267.5 ± 3.066	255.8 ± 2.857	4.609 ± 298.9
$E^{S3}_{7\times7}$ [MeV]	280.5 ± 3.168	266.1 ± 2.881	5.447 ± 303.7
f_3	$0.004541 \pm 5.371{\cdot}10^{-5}$	$0.004483 \pm 5.256{\cdot}10^{-5}$	1.284 ± 1.198
$f_{3,\text{core}}$	$0.0035 \pm 4.453{\cdot}10^{-5}$	$0.003455 \pm 4.683{\cdot}10^{-5}$	1.308 ± 1.289

variable	FastCaloSim	GEANT4	relative difference in %
f_0^{overall}	$0.007243 \pm 8.018{\cdot}10^{-5}$	$0.007034 \pm 7.551{\cdot}10^{-5}$	2.965 ± 1.14
f_1^{overall}	0.1747 ± 0.0009076	0.1745 ± 0.0008794	0.1416 ± 0.5276
f_2^{overall}	0.8105 ± 0.0009335	0.8113 ± 0.0009119	0.1023 ± 0.1468
f_0^{over012}	$0.007284 \pm 8.075{\cdot}10^{-5}$	$0.007088 \pm 7.748{\cdot}10^{-5}$	2.767 ± 1.139
f_1^{over012}	0.1757 ± 0.0009114	0.1754 ± 0.0008818	0.1476 ± 0.527
f_2^{over012}	0.817 ± 0.00097	0.8175 ± 0.0009387	0.05566 ± 0.1513
R_{had}	$0.00245 \pm 9.309{\cdot}10^{-5}$	0.002363 ± 0.000151	3.675 ± 3.94
E_T [GeV]	62.96 ± 0.01179	62.94 ± 0.009864	0.03257 ± 1.179
E_T^{Had} [MeV]	153.5 ± 5.809	141.2 ± 7.765	8.733 ± 844.3

Table B.4.: RMS of the shower shape variables for 65 GeV photons in the region $0.20 < |\eta| < 0.25$ for FastCaloSim (FCS) and GEANT4 (G4) in comparison.

variable	FastCaloSim	GEANT4	relative difference in %
E_{tot} [GeV]	64.55 ± 0.01197	64.65 ± 0.009793	0.1623 ± 1.197
$E^{S0}_{1\times1}$ [MeV]	326.6 ± 4.061	351.2 ± 3.987	7.01 ± 370.7
$E^{S0}_{3\times3}$ [MeV]	386.9 ± 4.64	403.1 ± 4.514	4.023 ± 433.2
$w_{\eta1}$	0.5656 ± 0.0009833	0 ± 0	0 ± 0
w_{stot}	1.619 ± 0.002793	0 ± 0	0 ± 0
E_{ratio}	0.8669 ± 0.002303	0.8711 ± 0.002391	0.4734 ± 0.3557
f_1	0.1751 ± 0.0009101	0.1749 ± 0.0008805	0.1561 ± 0.5279
$E^{S1}_{3\times2}$ [GeV]	8.767 ± 0.04602	8.781 ± 0.04412	0.1553 ± 4.602
$E^{S1}_{15\times2}$ [GeV]	10.55 ± 0.05686	10.6 ± 0.05501	0.4623 ± 5.686
f_{side}	0.1364 ± 0.0004769	0 ± 0	0 ± 0
E_{maxs1} [GeV]	5.522 ± 0.02858	5.513 ± 0.02705	0.1703 ± 2.858
E_{had1} [MeV]	157.4 ± 5.963	130.4 ± 4.488	20.71 ± 541.8
$f_{1,\text{core}}$	0.136 ± 0.0007137	0.1359 ± 0.0006806	0.08389 ± 0.5296
$r_{\text{33over37allcalo}}$	0.938 ± 0.000312	0.9387 ± 0.0003182	0.06999 ± 0.046
E_{core} [GeV]	62.68 ± 0.01835	62.8 ± 0.02218	0.1879 ± 1.835
E_{mins1} [MeV]	197 ± 4.266	54.84 ± 2.386	259.2 ± 856.9
asy_1	0.00341 ± 0.004266	0 ± 0	0 ± 0
bary_{S1}	0.003484 ± 0.002252	0.003528 ± 0.002254	1.241 ± 63.82
E_{2tsts1} [MeV]	371.1 ± 7.78	347.6 ± 7.643	6.763 ± 815.9
E_{2ts1} [GeV]	8.129 ± 0.04309	8.138 ± 0.04121	0.1057 ± 4.309
ΔE [MeV]	178.7 ± 7.774	271.3 ± 6.962	34.14 ± 458.5
R_η	$0.9693 \pm 4.995{\cdot}10^{-5}$	$0.9696 \pm 7.35{\cdot}10^{-5}$	0.02104 ± 0.008974
R_ϕ	$0.9734 \pm 5.161{\cdot}10^{-5}$	$0.9739 \pm 6.375{\cdot}10^{-5}$	0.04898 ± 0.008288
$w_{\eta2}$	$0.01048 \pm 1.511{\cdot}10^{-5}$	$0.0105 \pm 1.548{\cdot}10^{-5}$	0.202 ± 0.144
$E^{S2}_{3\times3}$ [GeV]	48.91 ± 0.06034	49.04 ± 0.06055	0.2616 ± 6.034
$E^{S2}_{3\times5}$ [GeV]	49.98 ± 0.06055	50.08 ± 0.06054	0.2087 ± 6.055
$E^{S2}_{5\times5}$ [GeV]	51.12 ± 0.06074	51.21 ± 0.06046	0.1865 ± 6.074
$E^{S2}_{3\times7}$ [GeV]	50.23 ± 0.06057	50.33 ± 0.0605	0.2009 ± 6.057
$E^{S2}_{7\times7}$ [GeV]	51.8 ± 0.06081	51.88 ± 0.06033	0.1621 ± 6.081
$E^{S3}_{3\times3}$ [MeV]	222.6 ± 2.697	219.2 ± 2.716	1.558 ± 275.8
$E^{S3}_{3\times5}$ [MeV]	255.5 ± 2.977	246.1 ± 2.829	3.796 ± 293.6
$E^{S3}_{3\times7}$ [MeV]	267.5 ± 3.066	255.8 ± 2.857	4.609 ± 298.9
$E^{S3}_{7\times7}$ [MeV]	280.5 ± 3.168	266.1 ± 2.881	5.447 ± 303.7
f_3	$0.004541 \pm 5.371{\cdot}10^{-5}$	$0.004483 \pm 5.256{\cdot}10^{-5}$	1.284 ± 1.198
$f_{3,\text{core}}$	$0.0035 \pm 4.453{\cdot}10^{-5}$	$0.003455 \pm 4.683{\cdot}10^{-5}$	1.308 ± 1.289

variable	FastCaloSim	GEANT4	relative difference in %
f_0^{overall}	$0.007243 \pm 8.018 \cdot 10^{-5}$	$0.007034 \pm 7.551 \cdot 10^{-5}$	2.965 ± 1.14
f_1^{overall}	0.1747 ± 0.0009076	0.1745 ± 0.0008794	0.1416 ± 0.5276
f_2^{overall}	0.8105 ± 0.0009335	0.8113 ± 0.0009119	0.1023 ± 0.1468
f_0^{over012}	$0.007284 \pm 8.075 \cdot 10^{-5}$	$0.007088 \pm 7.748 \cdot 10^{-5}$	2.767 ± 1.139
f_1^{over012}	0.1757 ± 0.0009114	0.1754 ± 0.0008818	0.1476 ± 0.527
f_2^{over012}	0.817 ± 0.00097	0.8175 ± 0.0009387	0.05566 ± 0.1513
R_{had}	$0.00245 \pm 9.309 \cdot 10^{-5}$	0.002363 ± 0.000151	3.675 ± 3.94
E_T [GeV]	62.96 ± 0.01179	62.94 ± 0.009864	0.03257 ± 1.179
E_T^{Had} [MeV]	153.5 ± 5.809	141.2 ± 7.765	8.733 ± 844.3

Table B.5.: Mean of the shower shape variables for 65 GeV pions in the region $0.20 < |\eta| < 0.25$ for FastCaloSim (FCS) and GEANT4 (G4) in comparison.

variable	FastCaloSim	GEANT4	relative difference in %
E_{tot} [GeV]	53.81 ± 0.07867	54.25 ± 0.06641	0.811 ± 7.867
$E^{S0}_{1\times1}$ [MeV]	223.8 ± 3.972	210.4 ± 3.929	6.324 ± 417.7
$E^{S0}_{3\times3}$ [MeV]	308.2 ± 5.718	311.1 ± 6.06	0.9574 ± 600.2
$w_{\eta1}$	0.38 ± 0.002643	0 ± 0	0 ± 0
w_{stot}	1.891 ± 0.0137	0 ± 0	0 ± 0
E_{ratio}	0.6854 ± 0.002205	0.5813 ± 0.00302	17.92 ± 0.5203
f_1	0.1245 ± 0.001216	0.1208 ± 0.001025	3.113 ± 1.012
$E^{S1}_{3\times2}$ [GeV]	1.144 ± 0.01769	1.144 ± 0.01985	0.02011 ± 1.769
$E^{S1}_{15\times2}$ [GeV]	1.743 ± 0.02824	1.881 ± 0.03133	7.356 ± 2.824
f_{side}	0.1634 ± 0.001862	0.1796 ± 0.002465	9.023 ± 1.061
E_{maxs1} [MeV]	714.7 ± 10.66	607.6 ± 10.52	17.62 ± 1237
E_{had1} [GeV]	13.61 ± 0.1258	13.81 ± 0.1251	1.455 ± 12.58
$f_{1,\text{core}}$	0.07728 ± 0.0007927	0.07091 ± 0.0006305	8.991 ± 1.12
$r_{\text{33over37allcalo}}$	0.9106 ± 0.0005741	0.9059 ± 0.0009443	0.5236 ± 0.1141
E_{core} [GeV]	17.2 ± 0.1569	17.72 ± 0.1639	2.934 ± 15.69
E_{mins1} [MeV]	24.18 ± 0.5783	2.338 ± 0.3868	934.1 ± 400.7
asy_1	-0.004028 ± 0.00352	0 ± 0	0 ± 0
bary_{S1}	0.00183 ± 0.002248	0.002158 ± 0.002314	15.2 ± 104.2
E_{2tsts1} [MeV]	82.92 ± 1.779	146.8 ± 2.884	43.49 ± 163
E_{2ts1} [GeV]	1.05 ± 0.01653	1.073 ± 0.01843	2.113 ± 1.653
ΔE [MeV]	73.3 ± 1.86	100.3 ± 2.251	26.94 ± 164.5
R_η	0.9281 ± 0.0003694	0.9276 ± 0.0007193	0.05056 ± 0.08225
R_ϕ	0.9448 ± 0.0003146	0.9427 ± 0.0006118	0.2168 ± 0.06981
$w_{\eta2}$	0 ± 0	0 ± 0	0 ± 0
$E^{S2}_{3\times3}$ [GeV]	12.58 ± 0.1199	12.98 ± 0.1317	3.106 ± 11.99
$E^{S2}_{3\times5}$ [GeV]	13.32 ± 0.1274	13.66 ± 0.1363	2.528 ± 12.74
$E^{S2}_{5\times5}$ [GeV]	14.19 ± 0.1362	14.47 ± 0.1417	1.88 ± 13.62
$E^{S2}_{3\times7}$ [GeV]	13.56 ± 0.1298	13.88 ± 0.1377	2.32 ± 12.98
$E^{S2}_{7\times7}$ [GeV]	14.93 ± 0.1435	15.11 ± 0.1459	1.231 ± 14.35
$E^{S3}_{3\times3}$ [MeV]	756.8 ± 9.402	886.7 ± 12.82	14.65 ± 1094
$E^{S3}_{3\times5}$ [MeV]	853.7 ± 10.68	951.9 ± 13.18	10.32 ± 1182
$E^{S3}_{3\times7}$ [MeV]	896.8 ± 11.26	977.8 ± 13.29	8.283 ± 1219
$E^{S3}_{7\times7}$ [MeV]	966.1 ± 12.16	1019 ± 13.41	5.227 ± 1271
f_3	0.09421 ± 0.001258	0.0934 ± 0.001128	0.8653 ± 1.352
$f_{3,\text{core}}$	0.07003 ± 0.0009363	0.07651 ± 0.00105	8.468 ± 1.228

variable	FastCaloSim	GEANT4	relative difference in %
f_0^{overall}	0.009632 ± 0.0001862	0.008972 ± 0.0001684	7.356 ± 2.076
f_1^{overall}	0.04786 ± 0.0007533	0.04756 ± 0.0007386	0.6154 ± 1.586
f_2^{overall}	0.3026 ± 0.002741	0.3027 ± 0.002704	0.05451 ± 0.9449
f_0^{over012}	0.05348 ± 0.0007165	0.04958 ± 0.0005905	7.876 ± 1.447
f_1^{over012}	0.1335 ± 0.001259	0.1286 ± 0.00105	3.854 ± 0.9848
f_2^{over012}	0.813 ± 0.001627	0.8218 ± 0.001404	1.078 ± 0.2419
R_{had}	0.5367 ± 0.003437	0.5512 ± 0.003456	2.635 ± 0.7085
E_T [GeV]	52.75 ± 0.07676	52.32 ± 0.06481	0.8263 ± 7.676
E_T^{Had} [GeV]	28.73 ± 0.2022	29.2 ± 0.1984	1.594 ± 20.22

Table B.6.: RMS of the shower shape variables for 65 GeV pions in the region $0.20 < |\eta| < 0.25$ for FastCaloSim (FCS) and GEANT4 (G4) in comparison.

variable	FastCaloSim	GEANT4	relative difference in %
E_{tot} [GeV]	53.81 ± 0.07867	54.25 ± 0.06641	0.811 ± 7.867
$E^{S0}_{1\times1}$ [MeV]	223.8 ± 3.972	210.4 ± 3.929	6.324 ± 417.7
$E^{S0}_{3\times3}$ [MeV]	308.2 ± 5.718	311.1 ± 6.06	0.9574 ± 600.2
$w_{\eta1}$	0.38 ± 0.002643	0 ± 0	0 ± 0
w_{stot}	1.891 ± 0.0137	0 ± 0	0 ± 0
E_{ratio}	0.6854 ± 0.002205	0.5813 ± 0.00302	17.92 ± 0.5203
f_1	0.1245 ± 0.001216	0.1208 ± 0.001025	3.113 ± 1.012
$E^{S1}_{3\times2}$ [GeV]	1.144 ± 0.01769	1.144 ± 0.01985	0.02011 ± 1.769
$E^{S1}_{15\times2}$ [GeV]	1.743 ± 0.02824	1.881 ± 0.03133	7.356 ± 2.824
f_{side}	0.1634 ± 0.001862	0.1796 ± 0.002465	9.023 ± 1.061
E_{maxs1} [MeV]	714.7 ± 10.66	607.6 ± 10.52	17.62 ± 1237
E_{had1} [GeV]	13.61 ± 0.1258	13.81 ± 0.1251	1.455 ± 12.58
$f_{1,\text{core}}$	0.07728 ± 0.0007927	0.07091 ± 0.0006305	8.991 ± 1.12
$r_{33\text{over}37\text{allcalo}}$	0.9106 ± 0.0005741	0.9059 ± 0.0009443	0.5236 ± 0.1141
E_{core} [GeV]	17.2 ± 0.1569	17.72 ± 0.1639	2.934 ± 15.69
E_{mins1} [MeV]	24.18 ± 0.5783	2.338 ± 0.3868	934.1 ± 400.7
asy_1	-0.004028 ± 0.00352	0 ± 0	0 ± 0
bary_{S1}	0.00183 ± 0.002248	0.002158 ± 0.002314	15.2 ± 104.2
E_{2tsts1} [MeV]	82.92 ± 1.779	146.8 ± 2.884	43.49 ± 163
E_{2ts1} [GeV]	1.05 ± 0.01653	1.073 ± 0.01843	2.113 ± 1.653
ΔE [MeV]	73.3 ± 1.86	100.3 ± 2.251	26.94 ± 164.5
R_η	0.9281 ± 0.0003694	0.9276 ± 0.0007193	0.05056 ± 0.08225
R_ϕ	0.9448 ± 0.0003146	0.9427 ± 0.0006118	0.2168 ± 0.06981
$w_{\eta2}$	0 ± 0	0 ± 0	0 ± 0
$E^{S2}_{3\times3}$ [GeV]	12.58 ± 0.1199	12.98 ± 0.1317	3.106 ± 11.99
$E^{S2}_{3\times5}$ [GeV]	13.32 ± 0.1274	13.66 ± 0.1363	2.528 ± 12.74
$E^{S2}_{5\times5}$ [GeV]	14.19 ± 0.1362	14.47 ± 0.1417	1.88 ± 13.62
$E^{S2}_{3\times7}$ [GeV]	13.56 ± 0.1298	13.88 ± 0.1377	2.32 ± 12.98
$E^{S2}_{7\times7}$ [GeV]	14.93 ± 0.1435	15.11 ± 0.1459	1.231 ± 14.35
$E^{S3}_{3\times3}$ [MeV]	756.8 ± 9.402	886.7 ± 12.82	14.65 ± 1094
$E^{S3}_{3\times5}$ [MeV]	853.7 ± 10.68	951.9 ± 13.18	10.32 ± 1182
$E^{S3}_{3\times7}$ [MeV]	896.8 ± 11.26	977.8 ± 13.29	8.283 ± 1219
$E^{S3}_{7\times7}$ [MeV]	966.1 ± 12.16	1019 ± 13.41	5.227 ± 1271
f_3	0.09421 ± 0.001258	0.0934 ± 0.001128	0.8653 ± 1.352
$f_{3,\text{core}}$	0.07003 ± 0.0009363	0.07651 ± 0.00105	8.468 ± 1.228

variable	FastCaloSim	GEANT4	relative difference in %
f_0^{overall}	0.009632 ± 0.0001862	0.008972 ± 0.0001684	7.356 ± 2.076
f_1^{overall}	0.04786 ± 0.0007533	0.04756 ± 0.0007386	0.6154 ± 1.586
f_2^{overall}	0.3026 ± 0.002741	0.3027 ± 0.002704	0.05451 ± 0.9449
f_0^{over012}	0.05348 ± 0.0007165	0.04958 ± 0.0005905	7.876 ± 1.447
f_1^{over012}	0.1335 ± 0.001259	0.1286 ± 0.00105	3.854 ± 0.9848
f_2^{over012}	0.813 ± 0.001627	0.8218 ± 0.001404	1.078 ± 0.2419
R_{had}	0.5367 ± 0.003437	0.5512 ± 0.003456	2.635 ± 0.7085
E_T [GeV]	52.75 ± 0.07676	52.32 ± 0.06481	0.8263 ± 7.676
E_T^{Had} [GeV]	28.73 ± 0.2022	29.2 ± 0.1984	1.594 ± 20.22

Bibliography

[1] M. K. Gaillard, P.D. Grannis, F. J. Sciulli, *The Standard Model of particle physics*, Rev. Mod. Phys. **71** (1999)

[2] F. Englert, R. Brout, *Broken symmetry and the mass of gauge vector mesons*, Phy. Rev. Lett. **13** (1964)

[3] P. W. Higgs, *Broken symmetries and the masses of gauge bosons*, Phy. Rev. Lett. **13** (1964)

[4] G. S. Guralnik, C. R. Hagen, T. W. B. Kibble, *Global Conservation Laws and Massless Particles*, Phys. Rev. Lett. **13** (1964)

[5] ATLAS Collaboration, *The ATLAS experiment at the CERN Large Hadron Collider*, JINST **3** (2008)

[6] CMS Collaboration, *The CMS experiment at the CERN LHC*, JINST **3** (2008)

[7] P. Mermod, *Prospects of the SHiP and NA62 experiments at CERN for hidden sector searches. Hidden sector searches with SHiP and NA62*, PoS **NuFact2017** (2017)

[8] P. A. Zyla, et al. (Particle Data Group), *Review of particle physics*, Prog. Theor. Exp. Phys. **2020** (2020)

[9] A. Salam, *Gauge unification of fundamental forces*, Rev. Mod. Phys. **52** (1980)

[10] S. Weinberg, *A model of leptons*, Phys. Rev. Lett. **19** (1967)

[11] S. L. Glashow, *Partial-symmetries of weak interactions*, Nuclear Physics **22** (1961)

[12] ATLAS Collaboration, *Measurement of the W-boson mass in pp collisions at* $\sqrt{s} = 7$ *TeV with the ATLAS detector*, Eur. Phys. J. C **78** (2018)

[13] Working group on LEP energy and LEP Collaborations ALEPH, DELPHI, L3 and OPAL, *Measurement of the mass of the Z boson and the energy calibration of LEP*, Physics Letters B **307** (1993)

[14] P. W. Higgs, *Broken Symmetries, Massless Particles and Gauge Fields*, Phys. Lett. **12**, 132 (1964)

[15] F. Englert, R. Brout, *Broken Symmetry and the Mass of Gauge Vector Mesons*, Phys. Rev. Lett. **13**, 321 (1964)

[16] J. Ellis, *Higgs Physics*, European School of High Energy Physics (2013)

[17] P. Kroupa et al., *Local-Group tests of dark-matter concordance cosmology*, Astron. Astrophys. **523** (2010)

[18] R. H. Cyburt, B. D. Fields, K. A. Olive, *Primordial nucleosynthesis in light of WMAP*, Phys. Lett. B **567** (2003)

[19] C. H. Llewellyn Smith, G. G. Ross, *The real gauge hierarchy problem*, Phys. Lett. B **105** (1981)

[20] C. W. Fabjan, F. Gianotti, *Calometry for particle physics*, Rev. Mod. Phys. **75** (2003)

[21] H. Kolanoski, N. Wermes, *Teilchendetectoren. Grundlagen und Anwendungen*, Springer-Verlag (2016)

[22] L. R. Evans, P. Bryant, *LHC Machine*, JINST **3** (2008)

[23] C. Lefèvre, et al., *The CERN accelerator complex. Complexe des accélérateurs du CERN*, Technical report (2008)

[24] ATLAS Collaboration, *Technical design report for the ATLAS Inner Tracker Strip Detector*, `https://cds.cern.ch/record/2257755` (2017)

[25] ATLAS Collaboration, *Electron and photon performance measurements with the ATLAS detector using the 2015-2017 LHC proton-proton collision data*, JINST **14** (2019)

[26] ATLAS Collaboration, *Electron reconstruction and identification in the ATLAS experiment using the 2015 and 2016 LHC protonâproton collision data at* $\sqrt{s} = 13$ *TeV*, Eur. Phys. J. C **79** (2019)

[27] A. Hoecker et al., *TMVA: Toolkit for multivariate data analysis*, PoS ACAT **040** (2007)

[28] J. C. Saxon, *Discovery of the Higgs boson, measurements of its production, and a search for Higgs boson pair production*, Ph.D. thesis, University of Pennsylvania (2014)

[29] S. Agostinelli, et al., *GEANT4: A simulation toolkit*, Nucl. Instrum. Methods A **506**, 250 (2003)

[30] ATLAS Collaboration, *ATLAS HL-LHC computing conceptual design report*, `https://cds.cern.ch/record/2729668/` (2020)

[31] ATLAS Collaboration, *AtlFast3: The next generation of fast simulation in ATLAS*, ATL-COM-PHYS-2021-373 (2021), `https://cds.cern.ch/record/2771484` (ATLAS internal note)

[32] ATLAS Collaboration, *The ATLAS simulation infrastructure*, Eur. Phys. J. C (2010)

[33] ATLAS Collaboration, *Fast simulation of the ATLAS calorimeter system with Generative Adversarial Networks* (2020), `https://cds.cern.ch/record/2746032`

[34] J. Beirer, *AtlFast3: The next generation of fast simulation in ATLAS*, `https://cds.cern.ch/record/2774959` (2021)

[35] I. T. Jolliffe, *Principal Component Analysis*, Springer-Verlag New York (2002)

[36] ATLAS Collaboration, *Public plots*, `https://atlas.web.cern.ch/Atlas/GROUPS/PHYSICS/PLOTS/SIM-2021-003/` (Accessed on 26-07-21)

[37] ATLAS Collaboration, *Optimisation of large-radius jet reconstruction for the ATLAS detector in 13 TeV proton-proton collisions*, `http://cds.cern.ch/record/2723736` (2020)

[38] R. Wigmans, M. T. Zeyrek, *On the differences between calorimetric detection of electrons and photons*, Nucl. Instrum. Methods A **485** (2002)

[39] ATLAS Collaboration, *Topological cell clustering in the ATLAS calorimeters and its performance in LHC Run 1*, Eur. Phys. J. C **77** (2017)

[40] W. Lampl et al., *Calorimeter Clustering Algorithms: Description and Performance* (2008), `https://cds.cern.ch/record/1099735`

Acknowledgements

First of all, I naturally would like to thank Stan for giving me this opportunity and for being such a supportive and involved supervisor. I know, it does not go without saying that professors care so much about Bachelor students. Also, your way of being so friendly and cheerful combined with your high expectations is a really good and effective way to motivate people! I would hate to disappoint you. And thanks again for the pizza. I had a really great time! At this point, many thanks to Jason, too, also for spending a week explaining ROOT and Athena etc.

Then, needless to say that I owe you, Joshua, for spending so much time and putting so much work in for me, for responding to my helpless, desperate and probably sometimes stupid messages and questions always within minutes, even late at night and on weekends. I must have been very annoying, sorry for that. But I hope you had a little fun, too. I really had a great and interesting time and learned so much thanks to your amazing supervision. Moreover, thank you endlessly for thoroughly reading and commenting my thesis on your holiday. It is incredible.

Many thanks also to Michael Duehrssen-Debling and Julien Maurer for their help with the implementation of the shower shape variables and to Guillaume Quétant and Mariia Drozdova for sharing their implementation of a simple topological clustering algorithm in Python, on which ground I constructed my clustering algorithm. Also, thanks a lot for always being so helpful and taking the time to answer all my questions in personal meetings or via mail.

Finally, I would like to thank my roommates for listening to me going on and on about how cool my Bachelor's thesis is and how annoying compiling errors are, and for pretending to understand and to care about what I was babbling. Also, thanks to my friends and family for encouraging and supporting me, especially Jannis, you know why.

Erklärung nach §13(9) der Prüfungsordnung für den Bachelor-Studiengang Physik und den Master-Studiengang Physik an der Universität Göttingen:
Hiermit erkläre ich, dass ich diese Abschlussarbeit selbständig verfasst habe, keine anderen als die angegebenen Quellen und Hilfsmittel benutzt habe und alle Stellen, die wörtlich oder sinngemäß aus veröffentlichten Schriften entnommen wurden, als solche kenntlich gemacht habe.
Darüberhinaus erkläre ich, dass diese Abschlussarbeit nicht, auch nicht auszugsweise, im Rahmen einer nichtbestandenen Prüfung an dieser oder einer anderen Hochschule eingereicht wurde.

Göttingen, den 31. Oktober 2021

(Carla Neubert)